UNIVERSITY OF SOUTHAMPTON
Faculty of Engineering, Science and Mathematics
School of Ocean & Earth Sciences

A laboratory investigation of frequency-dependent seismic anisotropy in fractured rocks

by

Philip Robert Tillotson

Thesis for the degree of Doctor of Philosophy

JUNE 2011

UNIVERSITY OF SOUTHAMPTON

ABSTRACT

FACULTY OF ENGINEERING, SCIENCE & MATHEMATICS
SCHOOL OF OCEAN & EARTH SCIENCES

Doctor of Philosophy

A LABORATORY INVESTIGATION OF FREQUENCY-DEPENDENT SEISMIC ANISOTROPY IN FRACTURED ROCKS

by Philip Robert Tillotson

Equivalent medium theories can be used to interpret seismic anisotropy in field seismic data to infer the properties of subsurface fractures. These theories analyse the seismic response of the rock in the long wavelength limit and relate the degree of anisotropy measured to the fracture properties. They have particular use in the hydrocarbon industry where extraction can be determined by both naturally and induced fractures. Validation is required to use these theories with more confidence in the commercial setting. One method for validation is through controlled laboratory seismic experiments. For the idealised fracture distributions found in these equivalent medium theories the laboratory experiments require rocks that can be built with a controlled fracture geometry.

I present ultrasonic laboratory data from three different experiments of synthetic porous rocks containing controlled fracture geometries. I then analyse the data using suitable theory where possible. Despite the ultrasonic experiments violating equivalent medium criteria strong relationships between data and theory were found.

The relationship between shear-wave splitting and fracture density was found to be highly robust. The dependence of shear-wave splitting on fluid saturation at 45° to the fracture normal was quantified for variations of fluid viscosity and bulk modulus and has direct implications for oil/water discrimination in fractured reservoirs. Based on a single fitting parameter from the water saturated data it was possible to accurately predict Thomsen's anisotropy parameters, ε and δ for air and glycerin saturation. Predictions of γ are independent of fluid saturation and model fitting and show strong agreement with the laboratory data.

Table of contents

List of figures

List of tables

Declaration of authorship

I, *Philip Robert Tillotson*, declare that the thesis entitled:

A laboratory investigation of frequency-dependent seismic anisotropy in fractured rocks

and the work presented in the thesis are both my own, and have been generated by me as the result of my own original research. I confirm that:

- this work was done wholly or mainly while in candidature for a research degree at this University;
- where any part of this thesis has previously been submitted for a degree or any other qualification at this University or any other institution, this has been clearly stated;
- where I have consulted the published work of others, this is always clearly attributed;
- where I have quoted from the work of others, the source is always given. With the exception of such quotations, this thesis is entirely my own work;
- I have acknowledged all main sources of help;
- where the thesis is based on work done by myself jointly with others, I have made clear exactly what was done by others and what I have contributed myself;
- parts of this work have been published as:

Conference abstracts:

Tillotson P., Sothcott J., Best A.I., Chapman M., Li X.Y. 2011. D029: Ultrasonic measurements of seismic anisotropy in synthetic silica cemented sandstones with controlled fracture geometry. 73st EAGE Conference and Exhibition, Vienna, Expanded Abstracts.

Tillotson P., Best A.I., Chapman M., Sothcott J., Li X.Y., Shangxu W. 2009. Z020: Laboratory ultrasonic validation of frequency-dependent seismic anisotropy in synthetic fractured, porous rocks. 71st EAGE Conference and Exhibition, Amsterdam, Expanded Abstracts.

Tillotson P., Best A.I., Chapman M., Sothcott J., Li X.Y., Shangxu W. 2008. Laboratory measurements of elastic wave anisotropy in synthetic cracked rocks. SEG Summer Research Workshop: Emergent and Challenging Issues in Rock Physics, Galway, Ireland, Expanded Abstracts, pg. 83.

Published and submitted papers:

Chapter 4:

Tillotson P., Chapman M., Best A. I., Sothcott J., McCann C., Shangxu W. and Li X. Y. 2011. Observations of fluid-dependent shear-wave splitting in synthetic porous rocks with aligned penny-shaped fractures. *Geophysical Prospecting* **59**, 111-119, doi: 10.1111/j.1365-2478.2010.00903.x.

Chapter 5:

Tillotson P., Sothcott J., Best A. I., Chapman M. and Li X. Y. Experimental verification of the fracture density and shear-wave splitting relationship using synthetic silica cemented sandstones with a controlled fracture geometry. *Submitted to Geophysical Prospecting April 2011.*

Chapter 6:

Tillotson P., Chapman M., Sothcott J., Best A. I., and Li X. Y. Analysis of P- and S-wave anisotropy in silica cemented sandstone with a controlled fracture geometry. *Submitted to Geophysical Prospecting June 2011.*

Signed: ……..

Date:……

Acknowledgments

I wish to express my gratitude to my supervisors Dr. Angus Best and Dr. Mark Chapman for their continual guidance, encouragement and support throughout my PhD. Special thanks go to Jeremy Sothcott for never-ending supply of both technical advice and humour for which my bill to him may take some time to repay. It was also his inspirational thought during the SEG Galway Rock Physics conference and enthusiasm that led us to the successful development of the synthetic fractured rocks.

I would like to thank the financial support of the Natural Environmental Research Council and the sponsors of the Edinburgh Anisotropy Project, particularly Sinopec, for funding the PhD project.

I extend my thanks to my friends in Southampton, both in the University and in the local area. Particular thanks go to my office mates for many enjoyable days at NOCS.

Finally, I wish to express my gratitude for the support (both moral and financial) from my family and to Melissa Pritchard for being eternally understanding.

Notation and conventions

The Einstein summation convention (i.e. summation over repeated indices) applies throughout this thesis.

I adopt the convention:

$$\dot{f} = \frac{\delta f}{\delta t}$$

for time variables, t.

Furthermore I also use the convention:

$$u_{i,j} = \frac{\delta u_i}{\delta x_j}$$

for a spatial variable, x.

List of symbols

Symbol	Meaning	Page introduced
δ	Thomsen's delta anisotropy parameter	168
ε	Thomsen's P-wave anisotropy parameter	167
V_P	P-wave velocity	18
V_S	S-wave velocity	18
N	Fractures per unit volume	14
Q	Quality factor	66
S1	S-wave polarised parallel with fractures	13
S2	S-wave polarised perpendicular to fractures	13
SWS	Shear-wave splitting	45
γ	Thomsen's S-wave anisotropy parameter	23
Φ_p	Porosity	32
ς	Grain size	40
C_{ijkl}	Stiffness tensor	9
$R(f)$	Reflection coefficient	65
S	Nomalised distance	63
a	Fracture radius	14
f	Frequency	42
k	Fluid bulk modulus	32
r	Aspect ratio	42
v	Poisson's ratio	42
$\alpha(f)$	Attenuation coefficient	65
ε_c	Mircocrack density	41
ε_f	Fracture density	14
η	Fluid viscosity	40
κ	Permeability	40
λ	Lamé parameter	11
μ	Shear modulus	11

ρ	Density	9
σ	Stress	9
τ_f	Fracture related relaxation time	41
τ_m	Grain scale relaxation time	41
ω	Angular frequency	42
ϵ	Strain	9

Chapter 1

Introduction.

It is known that seismic velocity and attenuation have a close relationship to the anisotropic properties of fractured rocks. Characterisation of these fracture systems play important roles for applications such as hydrocarbon reservoirs, geothermal reservoirs and nuclear waste repositories (Horne 2003).

In the hydrocarbon context, fractures can significantly affect the flow of reservoir fluids during extraction and are therefore important features to quantify for optimal production (Sayers 2009). Natural fractures within these hydrocarbon reservoirs are determined by the stress history of the rock and at depth will tend to be orientated normal to the direction of minimum in-situ stress (Schoenberg and Sayers 1995). If areas of high fracture density can be located and quantified they may represent potential sweet spots of high permeability, and for this reason could be a good target for infill drilling (Sayers 2009). It has been suggested that micro-scale cracks and macro-scale fractures can be a dominant cause of seismic anisotropy in hydrocarbon reservoirs (Liu et al. 1993). Therefore the use of seismic anisotropy to determine the orientation of the fractures is of considerable interest and if the observed seismic anisotropy could be attributed to micro- or macro-scale fractures then fluid flow modelling of hydrocarbon reservoirs could be improved (Maultzsch *et al.* 2003). Clearly, the ultimate goal for the geoscientist is to be able to remotely and reliably determine the fracture density, fracture size, fracture orientation, infill (water/oil/gas) and connectivity (Hudson *et al.* 2001).

Sets of orientated fractures can lead to directional dependent seismic velocities (Sayers 2009). For example fracture orientations have been inferred through P-wave amplitude variations seen with offset and azimuth (AVOA) analysed from a 3D ocean-bottom cable by Hall and Kendall (2003) and through the polarization directions and time delay differences between fast and slow shear waves observed in a Vertical Seismic Profile (VSP) survey by Maultzsch et al. (2003).

The application of equivalent medium theory to seismic data is one method used to extract geological information. These theories relate seismic properties to the fracture properties within a rock in the long wavelength limit (wavelength of the seismic wave is the order of ten times that of the individual fracture size). The fractures we wish to model may be considerably smaller than this and also below the resolution of typical seismic reflection surveys.

Two classical equivalent medium mathematical models often used for the characterisation of fractures are those of Hudson (1981) and Thomsen (1995) that are limited to the high and low frequency range, respectively. However, a more recent theory by Chapman (2003) models frequency-dependent seismic anisotropy in fractured reservoir rocks through knowledge of rock porosity, permeability, fracture density and orientation, and pore fluid properties viscosity, bulk modulus and density. The model is based on a squirt flow mechanism in an anisotropic porous rock with two crack populations: randomly aligned, grain contact, ellipsoidal microcracks defined by the grain size; and aligned, mesoscale, ellipsoidal fractures which are longer than the grain size. For this reason the theory can account for the two different length scales, a problem that previous frequency-independent fracture models have struggled to quantify. The results of the model agree with Brown and Korringa (1975) in the low frequency range and Hudson (1981) in the high frequency range. In the absence of aligned mesoscale fractures the model returns to the isotropic, microcrack squirt-flow model of Chapman *et al.* (2002) which was tested against laboratory data by Chapman (2001).

A more recent application of equivalent medium theories is the prediction of fluid saturation from shear-wave data (Qian *et al.* 2007). In the case of fractured reservoirs, frequency-dependent seismic anisotropy predicts anisotropic velocity and attenuation relationships between fracture properties (e.g. fracture size and orientation) as well as fluid properties such as viscosity. A common problem in oil exploration is the discrimination between oil and water in a reservoir using seismic reflection data. However, theoretical predictions of frequency-dependent seismic anisotropy indicate that S-waves are more sensitive to the fluid viscosity in a fractured reservoir than the commonly used P-waves in some directions (Qian *et al.* 2007). The sensitivity of shear-wave splitting to saturating fluid has already been observed on a field scale by van der Kolk *et al.* (2001) and for this reason, mode converted S-wave analysis has the potential to improve fluid type predictions within fractured reservoirs.

To date there have only been a handful of laboratory experiments that seek to validate theoretical models of seismic wave propagation in fractured, porous rocks. Most famously the work of Rathore *et al.* (1995) produced synthetic porous sandstones containing aligned penny-shaped voids with a diameter of 5.5 mm. They measured ultrasonic P- & S-wave velocity at 100 kHz on dry and water saturated samples as a function of wave propagation direction. The data were compared to the model predictions of Hudson (1981) and Thomsen (1995). Some limitations of the work included: evidence for scattering (Hudson *et al.* 2001); only two saturation states were measured (dry and water); little emphasis on attenuation; and an unrealistic rock cement (sand grains or glass beads cemented with epoxy resin). Despite these limitations, their model predictions showed that low frequency theory could explain some of the experimental observations.

The aim of this work is to take laboratory based theory validation to the next level of sophistication. Two sets of novel synthetic fractured rock were measured using the well established and accurate ultrasonic pulse-echo system and another using a bench-top technique. Here P- & S-wave velocity and attenuation coefficient were measured in synthetic

porous rocks with aligned, penny-shaped fractures while fully saturated with various fluids. The theory of Chapman (2003) was applied to the laboratory data with an aim to validate particular aspects of the theory.

I begin this thesis with a review of observations of seismic anisotropy in crustal rocks. Initially, I describe the theoretical predictions between fracture density and S-wave anisotropy, the effect of fracture direction and pore fluid saturation. I shall then go on to show how these principles have been observed in both the laboratory and on a field seismic scale.

Chapter three describes the theoretical predictions of the Chapman (2003) model. I include carefully selected model outputs that predict azimuthal anisotropy for velocity and attenuation and other variables such as pore fluid viscosity variations and sensitivity to fracture size.

In Chapter four I introduce the ultrasonic pulse-echo system and describe the system advantages and disadvantages for this study, measurement techniques, accuracy and data processing. This chapter will concentrate on experiments carried out on a block of synthetic fractured rock produced by the China National Petroleum Corporation (CNPC) with comparisons between the laboratory data and theory being made. Particular emphasis is placed on measurements and theoretical predictions of shear-wave splitting and their relationship to fluid viscosity and fracture density.

Chapter five describes novel samples produced at the National Oceanography Centre, Southampton. The samples were designed to provide a more realistic base rock and smaller fracture size than that of the CNPC samples. The manufacturing method is documented and the series of laboratory experiments conducted on the samples is described. The results show that traditional equivalent medium theory cannot be applied to the dataset given major differences in physical properties between the core samples at different orientations to the fracture normal. Despite this, measurements of shear-wave splitting confirmed some theoretical expectations.

In chapter six I describe an experiment designed to overcome the inter-sample variability seen in the data collected in chapter 5. Two

octagonal samples were studied, one containing penny shaped voids in a much better constrained controlled geometry than the cores in chapter 5. The other sample was left blank to study the background layering anisotropy. Both samples were made from the same material at the same time. The faces of both octagonal samples were 1 inch in width so that a bench-top laboratory arrangement could be used to study the velocity and attenuation anisotropy (using a duralumin reference sample) at atmospheric pressure for a variety of fluid saturations. Both samples were measured air, water and glycerin saturated. By taking into account the layering anisotropy found in the unfractured sample, the model results show good agreement with the laboratory data. A further finding was a corroboration of the result from chapter 4 where shear-wave splitting observations at 45° to the fracture normal were found to be sensitive to fluid saturation.

Chapter seven comprises a discussion of the significance of the laboratory results and their implications for seismic exploration. Finally, the conclusions of the thesis are summarised.

Chapter 2

Review of seismic anisotropy in crustal rocks.

Summary: This chapter introduces the concept of seismic anisotropy, discusses its origins and introduces some basic theoretical ideas. Experiments in both the laboratory and field setting are reviewed. This leads to the conclusion that ultrasonic measurements on synthetic fractured rocks can be used to validate some aspects of low frequency equivalent medium theories. Once validated, these low frequency theories can then be used to interpret seismic anisotropy observations from multi-component seismic data, such as from 3D Vertical Seismic Profile (VSP) and 3D, three-component (3C), surface seismic surveys.

2.1 Wave propagation in anisotropic media.

Seismic anisotropy is the dependence of the seismic properties of an elastic medium on direction and may be caused by a number of mechanisms including crystal alignment, stress-induced effects, regular sedimentary layers and cracks (Crampin 1981).

The stiffness tensor C_{ijkl} which relates stress σ_{ij} to strain ϵ_{kl} is related through Hooke's law:

$$\sigma_{ij} = C_{ijkl}\,\epsilon_{kl}\,, \tag{2.1}$$

where C_{ijkl} is a forth-rank tensor and has a total of 81 components. However, not all components are independent and symmetries in the stress and strain tensors and the existence of a unique strain energy potential reduces the number of independent constants to 21 (Mavko *et al.* 1998). This stiffness tensor can then be written as a condensed 6 by 6 matrix using Voigt notation.

Combining Hooke's law with Newton's second law leads to the elastodynamic wave equation that relates stiffness to displacement, u:

$$C_{ijkl}\mathrm{u}_{k,lj} = \rho\ddot{u}_i\,, \tag{2.2}$$

where ρ is the density of the material. The general expression for the harmonic displacement of a plane wave is given by,

$$\mathrm{u}_k = A_k \exp\left[i\omega\left(t - p_j x_j\right)\right], \tag{2.3}$$

where A_k is the amplitude vector specifying the polarization of the particle motion, $p = \mathbf{n}/c$ is the slowness vector and ω is the angular frequency. Substituting equation 2.3 into equation 2.2 reveals the eigenvalue problem:

$$(\Gamma_{ik} - \rho c^2)A_k = 0\,, \tag{2.4}$$

with,

$$\Gamma_{ik} = C_{ijkl}\mathbf{n}_j\mathbf{n}_l\,, \tag{2.5}$$

where $\mathbf{n}$ is the unit vector normal to the wavefront and v is the phase velocity. Equation 2.4 is referred to as the Kelvin-Christoffel equation and equation 2.5 is known as the Christoffel matrix.

Solving the eigenvalue problem reveals three eigenvalues and corresponding eigenvectors. The eigenvalues are equal to ρc^2 and give three mutually orthogonal phase body velocities and corresponding polarization vectors, A. Therefore in a general anisotropic medium, given a propagation direction, $\mathbf{n}$, three body waves exist: P-, S1- and S2-waves. The two shear waves have different velocities and polarizations and give rise to shear-wave splitting (see chapter 2.2).

When the phase velocity depends on angle, group velocity will not be identical. In the anisotropic case the group velocity determines the propagation of energy along a ray and is normal to the slowness surface whereas phase velocity is always perpendicular to the wavefront (Figure 2.1 adapted from Sheriff and Geldart 1999).

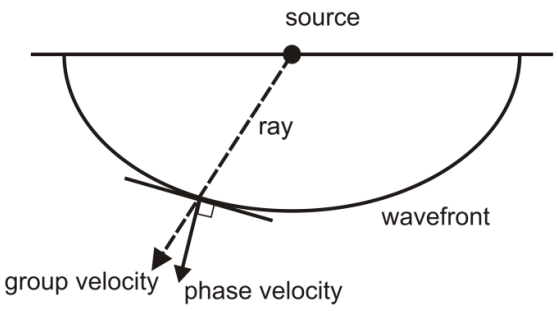

Figure 2.1: Wavefront in anisotropic medium showing difference between phase and group velocity according to Huygen's principle.

Symmetry systems have an impact on the elastic constants in the 6 by 6 matrix. Isotropy has the highest possible symmetry where there are only two independent elastic constants known as Lamé constants, λ and μ:

$$\begin{bmatrix} c_{11} & c_{12} & c_{12} & 0 & 0 & 0 \\ c_{12} & c_{11} & c_{12} & 0 & 0 & 0 \\ c_{12} & c_{12} & c_{11} & 0 & 0 & 0 \\ 0 & 0 & 0 & c_{44} & 0 & 0 \\ 0 & 0 & 0 & 0 & c_{44} & 0 \\ 0 & 0 & 0 & 0 & 0 & c_{44} \end{bmatrix},$$

where $c_{11} = \lambda + 2\mu$, $c_{12} = \mu$ and $c_{44} = \mu$.

Hexagonal symmetry, also called transversely isotropic, is described by 5 independent stiffness constants where the wave slowness surface is rotationally symmetric about the axis of symmetry and has the following form:

$$\begin{bmatrix} c_{11} & c_{12} & c_{13} & 0 & 0 & 0 \\ c_{12} & c_{11} & c_{13} & 0 & 0 & 0 \\ c_{13} & c_{13} & c_{13} & 0 & 0 & 0 \\ 0 & 0 & 0 & c_{44} & 0 & 0 \\ 0 & 0 & 0 & 0 & c_{44} & 0 \\ 0 & 0 & 0 & 0 & 0 & c_{66} \end{bmatrix},$$

The five components of the stiffness tensor need to be measured from 5 velocity measurements (Wang 2002); $\mathrm{V_P}(90°)$, $\mathrm{V_P}(0°)$, $\mathrm{V_P}(45°)$, $\mathrm{S1}(90°)$ and $\mathrm{S1}(0°)$ where,

$$c_{11} = \rho V_P(90°),$$
$$c_{12} = c_{11} - 2\rho S1^2(90°),$$
$$c_{33} = \rho {V_P}^2(0°),$$
$$c_{44} = \rho S1^2(0°),$$
$$c_{13} = -c_{44}$$
$$+\sqrt{4\rho V_P(45°)^4 - 2\rho V_P(45°)^2(c_{11}+c_{33}+2c_{44}) + (c_{11}+c_{44})(c_{33}+c_{44})},$$
$$c_{66} = \frac{1}{2}(c_{11} - c_{12}),$$

An example of a system with a vertical symmetry axis (VTI) include shales (Wang 2002) and fine sedimentary horizontal stratifications in the long wavelength limit (Backus 1962, Berryman 1979). Transverse isotropy with a horizontal axis of symmetry (HTI or azimuthal) can be used to describe a system of aligned vertical fractures (Crampin 1986).

The other symmetry system that is commonly used for seismic applications is orthorhombic symmetry which contains 9 independent elastic constants. This symmetry can be described by thin layered sedimentary beds combined with vertically aligned fractures (Ass'ad 2005).

2.2 Background and theory of seismic anisotropy.

Seismic anisotropy was first successfully observed by Hess (1964) in oceanic fracture zones. He attributed the observed azimuthal variations of P-wave velocity to the effects of wave propagation through olivine crystals showing preferred orientations caused by mantle flow away from spreading ridges. Over the past twenty years in particular, several theoretical and technical breakthroughs have taken the subject of seismic anisotropy from one of pure academic interest to a topic of key importance to the industrial seismic exploration and exploitation of hydrocarbons (Thomsen 2001). In fact advances in the parameterisation of anisotropy (e.g. Thomsen 1986) combined with the move from poststack imaging to prestack depth migration, wider offset 3D surveys

and increased quality multi-component data has led anisotropy to become a widespread application in seismic exploration (Tsvankin *et al.* 2010).

Major theoretical breakthroughs in the study of anisotropy (e.g. Crampin 1981, Hudson 1981) showed that shear-wave splitting was the most diagnostic feature of anisotropy related to cracks and fractures in rocks. Shear-wave splitting occurs when shear waves (S-waves) enter a system of fractures and split into two orthogonally polarised waves that travel at different velocities (Figure 2.1); S1 (or V_{SH}) polarised parallel with the fractures and S2 (or V_{SV}) polarised perpendicular to the fractures (Crampin and Peacock 2005).

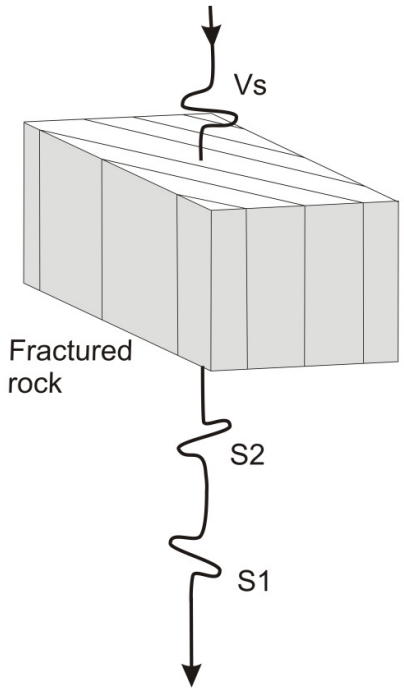

Figure 2.2: Schematic illustration of shear-wave splitting.

Work including Crampin (1981), Crampin (1985), Willis *et al*. (1986), Lynn and Thomsen (1986) demonstrated that shear-wave splitting due to azimuthal anisotropy was a first order influence using converted PS-waves. To analyse the shear-wave splitting, shear-wave processing is still

based on Alford (1986) rotation and its various modifications (Tsvankin *et al.* 2010).

Natural fractures are determined by the stress history of the rock. At depth, they will tend to be orientated normal to the direction of minimum *in-situ* stress (Schoenberg and Sayers 1995) and, below a critical depth of around 500 to 1000 m, it has been suggested that these fractures are nearly vertical (Crampin and Peacock 2005) and thus can cause azimuthal anisotropy. Since fracture systems dominate the fluid drainage pattern in many hydrocarbon reservoirs they have the potential to change low matrix permeability rocks into commercial assets (Willis *et al.* 2006). It is also becoming increasingly common for induced fracturing to take place using high pressure fluids as an aid to increase the natural permeability of a reservoir (e.g. Meadows and Winterstein 1994, Block *et al.* 1994). It is therefore clear to see that the development of mathematical models relating anisotropic seismic properties to the fractures is of upmost importance (Chapman 2003).

For shear wave propagation through these fracture sets the polarisation direction of the fast shear wave is often interpreted as the principal direction of the predominant fracture set (Liu *et al.* 2006). Further information can be obtained using the time-delays between the split shear-waves, providing information about the average fracture density of the rock (Crampin 1985).

Appropriate equivalent medium theories are needed to interpret suitable seismic datasets in terms of fracture properties. These theories relate the fracture density (ε_f) to the amount of anisotropy measured by the simple expression (Crampin 1981),

$$\varepsilon_f = \frac{\mathrm{N}a^3}{\mathrm{V}}, \tag{2.6}$$

where N is the number of fractures in a unit volume V, and a is the fracture radius. This relationship is believed to be valid up to ε_f = 0.1 (Crampin 1984). However, fracture density can be an ambiguous measurement of the fracture distribution. For example, if a rock has

only a few large fractures and many smaller fractures then the same fracture density may be observed for different proportions of large to small fractures (Figure 2.2). A major cause of seismic anisotropy within hydrocarbon reservoirs is thought to be due to both micro-scale (grain-scale) and macro-scale (metre-scale) fractures (Liu *et al.* 1993). If the observed anisotropy could be attributed to either micro- or macro-scale fractures using equivalent medium theories then fluid flow modelling of hydrocarbon reservoirs could be improved (Maultzsch *et al.* 2003).

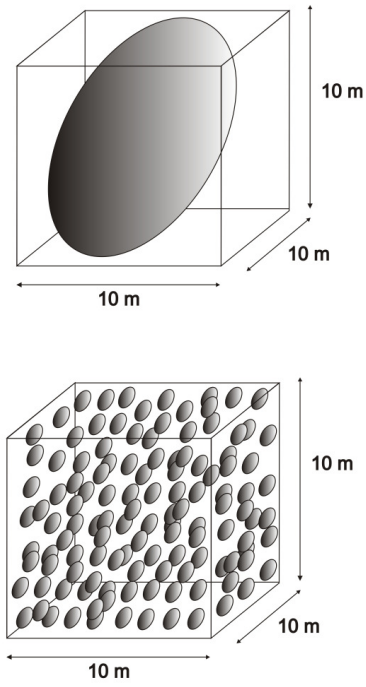

Figure 2.3: The fracture density problem. Both the top and bottom images have the same fracture density but different fracture sizes and distributions

Fracture modelling is typically implemented using the equivalent medium theories of Hudson (1981) and Thomsen (1995). Hudson's (1981) model takes into account the propagation of seismic waves through a material with thin (compared to the wavelength of the seismic wave) embedded fractures with a low fracture density. The model assumes that fluid is trapped within the fractures and does not connect

between other fractures and the surrounding pores. Therefore, this theory is limited to the high frequency range. This assumption means that fluid pressure can be altered due to the stress of the propagating elastic wave and will be different depending on fracture orientation. The matrix surrounding the fractures is assumed to be isotropic, with the overall elastic properties becoming anisotropic if the fractures have a non-random orientation.

The model of Thomsen (1995) differs from that of Hudson by incorporating localised hydraulic connections between the pores of the matrix and the fractures, with the fluid pressure being equal in both pores and fractures. This assumption limits the theory to low frequencies, since the period of the wave must be much longer than the time taken for the pressure to equalise. The model also takes into account anisotropic crack interactions described by Hoenig (1979). Thomsen's theory was compared to the laboratory experimental data of Rathore *et al*. (1995), obtained on synthetic cracked sandstones (see Chapter 2.2). It was concluded that the flow of fluid between the fractures and the pores is a significant process, something not accounted for in the Hudson (1981) model. For this reason his theoretical model predictions matched the ultrasonic data of Rathore *et al*. (1995) for water saturated samples more favourably than those of the Hudson (1981) model.

The theory of Chapman (2003) seeks to model frequency-dependent seismic anisotropy in fractured reservoir rocks through knowledge of rock porosity, permeability, fracture density and orientation, and the pore fluid viscosity, bulk modulus and density. The model is based on a squirt flow mechanism in an anisotropic porous rock with two crack populations: randomly aligned, grain contact, ellipsoidal microcracks defined by the grain size; and aligned, mesoscale, ellipsoidal fractures which are longer than the grain size. For this reason the theory can account for the two different length scales, a problem that previous fracture models have struggled to quantify. The results of the model agree with Brown and Korringa (1975) in the low frequency range and Hudson (1981) in the high frequency range. In the

absence of aligned mesoscale fractures the model returns to the isotropic, microcrack squirt-flow model of Chapman *et al.* (2002) which was tested against laboratory data by Chapman (2001). An explicit description of the Chapman (2003) model will follow in Chapter 3.

A more recent application of equivalent medium theories is the prediction of fluid saturation from shear-wave data (Qian *et al.* 2007). In the case of fractured reservoirs, frequency-dependent seismic anisotropy predicts anisotropic velocity and attenuation relationships between fracture properties (e.g. fracture size and orientation) as well as fluid properties such as viscosity. A common problem in oil exploration is the discrimination between oil and water in a reservoir using P-wave seismic reflection data since the two fluids have a similar bulk moduli. However, theoretical predictions of frequency-dependent seismic anisotropy indicate that S-waves are more sensitive to the fluid viscosity in a fractured reservoir at typical incidence angles for seismic data than the commonly used P-waves (Qian *et al.* 2007). This is due to the relationship between the fluid properties, known as the fluid mobility parameter, given by the ratio of permeability to fluid viscosity. The sensitivity of shear-wave splitting to saturating fluid has already been observed on a field scale by van der Kolk *et al.* (2001). For this reason, mode converted S-wave analysis has the potential to improve fluid type predictions within fractured reservoirs.

2.3 Laboratory observations of anisotropy in fractured rock.

One way to evaluate the reliability of equivalent medium theories for porous fractured rocks is through controlled elastic wave experiments on synthetic rock samples with fractures or penny-shaped voids. This method requires that velocities and attenuations can be measured with sufficient accuracy in at least three directions (e.g., 0˚, 45˚, 90˚ relative to the fracture normal) for transversely isotropic materials (an isotropic matrix containing a set of parallel fractures) and that the fracture size,

shape and density are known as well as the properties of the saturating fluid.

In a previous study, Rathore *et al.* (1995) produced blocks of synthetic porous sandstones containing aligned penny-shaped voids with a diameter of 5.5 mm. The construction of the samples initially involved mixing Danish beach sand (with a narrow grain size spectrum, mean value around 200 μm) and epoxy at a ratio of 25 parts sand to 1 part (2-component) epoxy. Fracture geometry was predefined, with shape (circular) size (5.5 mm diameter), thickness (0.02 mm), density (ε_f = 0.1, as defined by equation 2.1) and position specifically designed to test specific aspects of theoretical models. Fractures were formed by placing thin metallic discs in a total of 48 layers while the blocks were manufactured. Once the epoxy had set and dried, percolating fluids were used to leach out the aluminium leaving disc-shaped voids representing fractures. Since the leaching process liberated gas, this could be used as an indicator that all the aluminium had chemically reacted and was no longer present in the sample. Their final sample was a single block of length 25 cm, width 10 cm and height 10 cm. Fractures were concentrated in one end leaving the other end homogenous and fracture free. This had the advantage that any anisotropy caused by the manufacturing process on the background matrix could be measured. Once the leaching process had removed all the aluminium, water was then percolated through the sample for 24 hours to remove any trace of the acid. Finally, the sample was dried at 110 ˚C for over 24 hours. This single long sample was then cleaved into two rocks, both 10 cm long, one taken from each end of the original block. They were subsequently milled into 16 sided prisms to allow good ultrasonic transducer coupling at varying azimuths to the fracture direction at 22.5˚ increments.

They measured three ultrasonic velocities (P-wave [V_P], vertically polarized S-wave velocity [V_{SV}; measured tangentially] and horizontally polarized S-wave velocity [V_{SH}; measured axially]) at 100 kHz in transmission mode using a pair of 1 inch diameter Panametrics transducers with a central frequency of 100 kHz coupling either side of

the sample in a bench-top configuration. Both the fractured and unfractured samples were measured dry and water saturated (here the bench-top equipment was submersed under water with full evacuation of air to ensure total saturation) as a function of wave propagation direction. Velocities were calculated using,

$$\text{Velocity (V)} = \frac{L}{t_{received} - t_{transmitted}}, \tag{2.7}$$

where L is the sample length and t the time difference between the first zero-crossover of the received wave ($t_{received}$), and the first zero-crossover of the transmitted pulse ($t_{transmitted}$).

Anisotropy in the samples was calculated from,

$$\text{Percentage of anisotropy} = \frac{\text{V}_{max} - \text{V}_{min}}{\text{V}_{max}} \times 100\,, \tag{2.8}$$

The unfractured sample showed azimuthal anisotropy of 4% or lower, and was considered small enough for reasonable data quality. The fractured sample showed much larger variations in arrival times, and therefore velocity anisotropy, than when compared to the unfractured sample with respect to fracture azimuth (see Table 2.1 from Rathore *et al.* 1995). This proved that the presence of fractures was responsible for causing the large anisotropic velocity variations.

Sample		V_P	V_{SH}	V_{SV}
Fractured (Dry)	Max-Vel. (m/s)	2474	1512	1288
	Min-Vel. (m/s)	1783	1273	1260
	Anisotropy (%)	28	16	2
Fractured (Saturated)	Max-Vel. (m/s)	2706	1406	1292
	Min-Vel. (m/s)	2385	1186	1194
	Anisotropy (%)	12	16	8

Table 2.1: Velocity results from Rathore *et al.* (1995) on synthetic sandstone with disc-shaped voids (fractures) taken at 100 kHz both dry and water saturated.

The data were compared to the model predictions of Hudson (1981) and Thomsen (1995) since the design of the experiment allowed all the required properties of the samples (e.g. porosity, fracture density, matrix bulk density and fluid bulk modulus) to be measured. In the dry case it was seen that the model of Hudson (1981) fitted the experimental data the best. However, when water saturated the P-wave data clearly fitted the cosine 2θ azimuthal variation of Thomsen (1995) over the cosine 4θ azimuthal variation in the Hudson (1981) model. This showed that fluid flow between the fractures and the equant porosity of the rock, as introduced by Thomsen (1995), was indeed an important consideration.

Despite the success of the work, some limitations of the experiments are evident. Firstly there is evidence of scattering in the wave traces (Hudson *et al.* 2001). Rathore *et al.* (1995) quote that

wavelengths for P- & S-waves are around 22 mm and 14 mm respectively. With a fracture size of 5.5 mm, it can be noted that the wavelength to fracture size is at best 4.4 : 1, some way off the 10 : 1 required for equivalent medium modelling.

Another limitation of the study is that only two saturation states were measured (dry and water). This was sufficient to show the importance of fluid flow between fractures and equant porosity, but it does not allow for variations of viscosity to be modelled (e.g. to predict the presence of oil or water). Also, the study had very little emphasis on attenuation due to the laboratory set up, the samples had unrealistic rock cement (epoxy) and there was no error analysis for the velocity measurements. Despite these limitations, the theoretical model predictions showed that low frequency theory could explain some of the experimental observations.

Another laboratory study on Carrara marble compared ultrasonic velocity measurements to the Hudson (1981) model (Peacock *et al.* 1994b), and defined empirical relations between ultrasonic wave attenuation and fracture density (Peacock *et al.* 1994a). Measurements were carried out initially on unstressed samples, and then again after stress induced fractures had been formed. Carrara marble is 100% pure calcium carbonate with a very low porosity of 0.7% and little intrinsic anisotropy. The measurements were carried out using the pulse-echo system (see Chapter 4). P- and S-wave velocity and attenuation were measured in three samples of dry and then water saturated, unfractured, Carrara marble up to a confining pressure of 60 MPa. Eight samples were then subject to elevated stress creating fractures, then the same measurement procedure was followed to relate the changes in seismic properties to the induced fractures.

Fractures were induced in the eight Carrara marble samples by subjecting them to an axial stress of up to 376 MPa (exceeding the elastic limit of the rock) under a confining pressure of 65 MPa inside a Hoek cell using a servo-hydraulic loading actuator. Small fractures were observed on black and white photographs (247 x 156 mm) of 30-micron thin sections under reflected light magnified 100 times and counted

visually. The calcite crystals of the marble showed up as large highly reflected areas separated by black lines of low reflectance. The black lines were seen to follow grain boundaries, some penetrating grains and others straight lines, all assumed to be small fractures. These lines were counted by laying a grid of orthogonal lines over each photograph and measuring the orientation and length of each fracture that intersected a line and assuming a circular fracture radius. The mean number of fractures intersecting a unit length of the grid line as related to the surface area of cracks per unit volume was calculated from the relation (assuming circular cracks),

$$S_v = 2N_L\,, \tag{2.9}$$

where, S_v is the surface area of fractures per unit volume of fractures, and N_L is the mean number of fractures intersecting a unit length of a grid line.

The fracture density was then calculated from,

$$\varepsilon_f = \frac{Na^3}{V} = \frac{aS_v}{\pi}, \tag{2.10}$$

Peacock *et al.* (1994b) found that Hudson's theory systematically over predicted the observed fracture density in dry and water saturated Carrara marble samples with induced fractures. They concluded that the method for fracture density determination was probably at fault and that it was difficult to obtain accurate fracture densities from thin section analysis. Saturated samples gave particularity poor comparisons with Hudson's theory, in agreement with Rathore *et al.* (1995) observations.

Peacock *et al.* (1994a) presented experimental evidence for a correlation between ultrasonic wave attenuation and fracture density using the same Carrara Marble samples. They also found that attenuation was frequency dependent for P- and S-waves between 400 and 1000 kHz, that Q increased with increasing effective pressure

(attributed to the closure of micro-cracks), and that Hudson's theory for viscous dissipation attenuation mechanisms did not predict the low Q values seen in the experimental data.

The physical model study of Ass'ad, *et al.* (1992) recorded seismic waves propagating through a solid matrix containing penny-shaped inclusions. The matrix was comprised of epoxy resin and the inclusions were made from rubber with a lower density than the epoxy. They produced seven models: a homogenous isotropic rock, a layered solid block and five inclusion models. The first two models were used as control models to test the construction method for anisotropy and the five inclusion models had fracture densities (using equation 2.1) of 0.01, 0.03, 0.05, 0.07 and 0.1. Each inclusion model was constructed from 18 layers of equal thickness with rubber discs embedded within each layer, creating vertically aligned layers of inclusions. The disc radius and aspect ratio were kept similar for each block, and the number density per layer changed to alter the fracture density.

Experiments were carried out using a sonic (30 – 60 kHz) pulse transmission method and specifically measured S-waves to determine relationships between fracture density and anisotropy. The transducers (located on the top and bottom of the block) were rotated at 9° intervals and measured the V_{S1} (fast shear-wave) and V_{S2} (slow shear-wave) arrivals.

The measurements were again compared to the theory of Hudson (1981) and used the anisotropy parameter, γ (Thomsen 1986) defined as:

$$\gamma = \frac{1}{2}\left(\frac{{V_{S1}}^2}{{V_{S2}}^2} - 1\right) = \left(\frac{c_{66} - c_{44}}{2c_{44}}\right). \qquad (2.11)$$

They found that theory agrees well with the seismic observations on blocks with lower fracture densities ($\varepsilon_f \leq 0.07$) finding a strong correlation between fracture density and anisotropy. The S1 velocity is well matched throughout the range of fracture density models. The S2 velocity was more affected by the presence of the inclusions and, at 0.1

fracture density there was an increase of S2 velocity, attributed to scattering.

There were some drawbacks with the experiment: samples were only measured dry; only a single fracture orientation was measured; scattering is likely to have influenced the results given the fracture size (3.18 mm) relative to the sonic wavelengths that were used (20 – 40 mm) and no attenuation results were reported. Finally the physical model of sample matrix made from epoxy resin with low density rubber inclusions does not adequately represent a true fractured rock as a porous medium with crack-like voids.

A laboratory study by Best, Sothcott and McCann (2007) using the pulse-echo system looked at the variations of seismic velocity and attenuation anisotropy in near-surface sedimentary rocks using effective pressures between 5 and 50 MPa on a set of varied lithological cores (sandstone, limestone and siltstone). The rock samples were from boreholes, and the cores taken were cut parallel and perpendicular to the borehole axis. The samples showed differing amounts of laminations, some showing almost none, and others appearing to be strongly laminated. P- and S-wave velocity and attenuation anisotropy were observed and seen to depend on frequency, pressure and lithology. Anisotropy was seen to be greatest for rocks with visible laminations (velocity > 20%, attenuation >70%) and the sensitivity to pressure was attributed to the closure of micro-cracks. The results found that regardless of lithology, attenuation anisotropy was much higher than velocity anisotropy, and as a result could prove useful for monitoring pressure changes in reservoir rocks.

2.4 Field observations of seismic anisotropy.

The last two decades have seen a large number of theoretical and practical developments in seismic anisotropy methods for hydrocarbon exploration and exploitation (Thomsen 2001). Isotropic seismic P-wave analysis can be considered to be a mature method having been utilized

for several decades. However, modern processing techniques look to account for both P-wave and S-wave (usually from mode converted waves) anisotropy through the use of three component (3C) geophones and, even more recently, nine component surveys (three component geophones and three source line directions). The development of this technology has been relatively slow until recently but its full potential is beginning to be realised with the measurement of full-waveform attributes (e.g. amplitude, frequency, phase, attenuation and frequency dispersion) for both P- and S-waves (Xiyuan *et al.* 2009).

One major application of quantitative seismic anisotropy is the characterisation of fracture systems (both natural and induced) associated with hydrocarbon exploration and production. This is particularly relevant to fractured tight gas reservoirs, where production is usually only commercially viable because of the conduits to fluid flow along open fractures (Maultzsch *et al.* 2009).

Anisotropy measurements to determine fracture properties are carried out using the following methods: P-wave velocity anisotropy using azimuthal moveout and prestack amplitude analysis from vertical seismic profile (VSP) data, shear-wave analysis from multicomponent data and scattering.

VSP data is collected by fixing a string of geophones down a borehole or well and shooting a seismic source either around the hole (walkaround), away from the hole (walkaway) or a combination of both (Horne 2003). The relative fixed position of the geophones means that variations of azimuthal P-wave velocity and reflection amplitude away from the geophones can indicate anisotropy. These measurements have advantages over well-log instruments which measure velocity in the 5 kHz range which are much higher than field seismic sources.

In a simple survey design the geophones are one component and only record P-waves. In this case P-wave walkaway data allows estimation of the Thomsen anisotropy parameter δ, and with larger offsets ε in the presence of lateral VTI media (e.g. shales) (Tsvankin *et al.* 2010). Multicomponent geophones can also be used and they allow PP and PS converted waves to be measured.

Azimuthal variations of traveltimes are one method to investigate anisotropy associated with natural fracture systems. Wide-azimuth shots create an azimuthal moveout ellipse. This shape is used to interpret dominant fracture direction. It has shown to be an effective tool for interpreting natural fracture sets (Lynn *et al.* 1999, Tod *et al.* 2007, Maultzsch *et al.* 2009).

Prestack amplitude analysis analyses changes of reflection amplitude with offset (known as AVO) and/or azimuth. Reflection coefficients are given by the Zoeppritz (1919) for the isotropic case and for transverse isotropy are given by Rüger (2002). If the azimuthal anisotropy is assumed to be caused by a single set of vertical fractures (HTI symmetry) the maximum AVO gradient may be parallel or perpendicular to the fractures (Tsvankin *et al.* 2010). Despite this, studies have successfully used AVO to predict the dominant fracture direction (e.g. Gray *et al.* 2002, Hall and Kendall 2003). One way to remove the uncertainty involved in this method is to combine azimuthal AVO and attenuation analysis (e.g. Clarke *et al.* 2009). In this case the direction of minimum attenuation will be measured at 90° to the fracture normal direction (Hudson 1981, Chapman 2003, Maultzsch *et al.* 2007, Maultzsch *et al.* 2009).

Multicomponent geophones can be used to analyse shear-waves in addition to P-waves. Most measured shear-waves are from converted P to S reflections; however some land field seismic studies use a shear-wave source. Analysis of 9C3D (three-component geophones and three source orientations) data by van der Kolk *et al.* (2001) from the Naith field, Oman indicated a large region of shear-wave splitting. The magnitude of the shear-wave splitting and associated attenuation showed a large increase at the gas/oil contact within a carbonate reservoir; this suggested that shear-wave spitting was sensitive to the fluid filling a fractured hydrocarbon reservoir. The sensitivity of shear-waves to frequency has also been shown in multicomponent data (Liu *et al.* 2003, Maultzsch *et al.* 2003).

A method was devised by Willis *et al.* (2006) that determined the reflection and scattering characteristics of seismic energy from fractured

rocks from 3D3C seismic surveys. The method used the coda signature (ringing tail) of scattered seismic energy as seismic waves propagate through a fractured rock. It was found that the coherence of the coda signature was a function of the fracture spacing, the angle between the orientation of the fractures and acquisition direction, the wavelength of the seismic energy and the compliance of the fractures. The energy was found to be most coherent in the acquisition direction parallel to the strike of the fractures and had the largest amplitude when the seismic wavelengths were the same size as the fracture spacing. This method therefore could have the potential to estimate the dominant direction, size and openness of natural fracture sets.

Three-dimensional seismic attribute technology is another tool used to characterise the subsurface geology (Gao 2011). This approach uses seismic attribute analysis algorithms that detect changes and patterns in seismic amplitudes for large scale fractures and faults. They are used to enhance seismic images for interpretation and are particularly useful to map fractures and faults within three dimensional seismic volumes. Seismic coherence (Bahorich and Farmer 1995) is one attribute known to be effective at highlighting high-angle faults and has been used by Hall and Kendal (2003) to correlate with P-wave AVO and AVA to characterise fractures. These attributes can now be used with "Ant-tracking" to automatically detect and illuminate fractures and faults within seismic data.

2.5 Conclusions.

Seismic anisotropy is a well established robust method for detecting fractures within crustal rocks. The presence of fractures is seen to cause azimuthal variations of velocity and attenuation on both a laboratory and field scale. Another diagnostic feature of fractures is shear-wave splitting. The magnitude of shear-wave splitting is theoretically believed to be directly proportional to the fracture density up $\varepsilon = 0.1$. This relationship is widely used in industry in the analysis of field seismic

data, however the few laboratory validation experiments carried out to date are unsatisfactory for application to natural rocks in the Earth's crust. If this theoretical relationship turns out to be correct, then it is surely a very powerful seismic interpretation tool. However, we must first establish its range of validity for natural reservoir rocks with fractures.

The best method available to test the theoretical fracture models is through elastic wave measurements on rock samples with controlled fracture geometries under laboratory conditions. Only a handful of experiments exist in the literature, which all suffer from some systematic failures limiting their applicability to low frequency theory.

Chapter 3

Theory of frequency-dependent seismic anisotropy.

Summary: This chapter gives an overview of the theoretical model of Chapman (2003) that was used to analyse the laboratory data in Chapters 4 and 6. Historically, the classical theory of Biot-Gassmann has strong experimental support for predicting body wave velocity in saturated porous rocks. The main failing of the Biot-Gassmann model is that it under predicts attenuation observed in low permeability rocks and sediments, such as shaley sandstones, and hence also under predicts the true velocity dispersion in the seismic to ultrasonic bandwidth of interest to exploration seismology. The introduction of another loss mechanism such as local (so-called squirt) fluid flow is necessary to explain the observations. A range of squirt flow models exist including the model of Chapman *et al*. (2002). This model was extended to include aligned (anisotropic) meso-scale fractures (larger than the grain scale) by Chapman (2003). The model considers that fluid flow can occur on two scales, at seismic frequencies within the large fractures, and at ultrasonic frequencies in the small micro-cracks on the grain scale. This prediction means that anisotropic velocity dispersion and attenuation could occur at seismic frequencies. A further prediction of the model is that shear-wave splitting is sensitive to frequency, fluid type and fracture size.

3.1 Introduction to poroelasticity.

Poroelastic theories seek to establish the links between a porous, permeable elastic solid saturated with a viscous fluid and elastic wave propagation. The Biot-Gassmann theory of poroelasticity (Biot 1956, Gassman 1951) is a classic model still commonly used.

The theory of Gassmann (1951) is the most basic in poroelasticity and is still commonly used to predict velocity as a result of changes in fluid saturation of a rock. It considers three components of a rock: the mineral (or minerals) that makes up the solid grains, the dry framework of mineral grains (also known simply as the frame), and the saturating fluid that fills the pore space within the frame. However, there are underlying assumptions that limit the applicability of the model. The theory assumes that the mineral and frame are elastically isotropic, that there is perfect pressure communication between pores (i.e., the porosity is completely connected and that fluid has enough time to flow between pores for pressure equalisation to occur during the passing of a seismic wave; each point of the rock has the same pressure gradient); and that the rock is a closed system (i.e., there is no fluid flow into or out of the rock volume under consideration). A final assumption is that no chemical interaction takes place between the fluid and the solid mineral grains. These limits imply that the theory is best applied to low frequency seismic measurements at high static pressures.

Using these assumptions Gassmann calculated the saturated bulk and shear moduli in terms of the mineral bulk modulus, the dry frame moduli, the fluid bulk modulus and the porosity as follows:

$$k_{sat} = k_{dry} + \frac{\left(1 - \frac{k_{dry}}{k_m}\right)^2}{\frac{\Phi_p}{k_f} + \frac{1 - \Phi_p}{k_m} - \frac{k_{dry}}{k_m^2}}, \tag{3.1}$$

$$\mu_{sat} = \mu_{dry}, \tag{3.2}$$

where k_{sat} is the saturated bulk modulus, k_{dry} is the dry frame moduli, k_m is the mineral bulk modulus, k_f is the fluid bulk modulus, Φ_p is the porosity, μ_{dry} is the dry shear modulus and μ_{sat} is the saturated shear modulus.

The equations of Gassmann are widely used throughout the hydrocarbon industry where they are used to estimate seismic wave velocity in hydrocarbon reservoirs (Müller *et al.* 2010, Wang 2001, Smith *et al.* 2003, Mavko *et al.* 1998).

The theory of Gassmann is a zero frequency theory, and the first attempt to extend this to the entire frequency range (dynamic) was by Biot (1956). Thus, the Biot theory provides theoretical formulae for predicting the frequency-dependent velocities of saturated rocks from the dry rock properties (Mavko *et al.* 1998). Importantly, the theory introduced the concepts of velocity dispersion, attenuation and the existence of a second 'slow' P-wave (observed experimentally by Plona 1980). Velocity dispersion refers to the variation of propagation velocity with frequency, and attenuation, the exponential decay of wave amplitude with distance travelled (Müller *et al.* 2010).

The frequency-dependent velocities come as a result of the concept of wave-induced fluid flow. This fluid flow occurs as a passing wave creates pressure gradients within the fluid phase and its movement relative to the solid matrix. This flow causes internal friction until the pore pressure equilibrates. Specifically, wave-induced fluid flow at the wavelength scale results in so called "global" flow which the Biot theory models resulting in viscous-internal attenuation and velocity dispersion.

In typical sedimentary rocks this global flow can occur on a wide range of scales and thus can cause attenuation over a wide frequency band. For this reason attenuation related to global fluid-flow mechanisms is becoming increasingly more significant for modelling attenuation in the seismic frequency band (Pride *et al.* 2004).

The low frequency limits for Biot velocities reduce to Gassmann's formulae. The low frequency limit is typically stated as being in the seismic frequency range (Murphy 1984, Murphy 1985, Mavko and

Murkerji 1995). However, more recent observations suggest that this may not always be true due to the concept of fluid mobility and its relationship to frequency-dependent seismic velocity (Batzle *et al.* 2006).

There is a transition zone between the low and high frequency regime given by a characteristic frequency. This characteristic frequency is directly proportional to fluid viscosity and generally lies between 50 kHz and 1Ghz (Mavko *et al.* 1998). In the high frequency limit the dynamic equations generally do not match the level of dispersion measured in ultrasonic laboratory experiments at around 1.0 MHz (e.g. Winkler 1985, Winkler 1986, Best and McCann 1995). A further problem relates to the predictions of the model for variations in fluid viscosity. While the Biot-Gassmann theory predicts that velocity will reduce with increasing fluid viscosity, the opposite is observed in laboratory experiments (e.g. Jones 1986, Jones and Nur 1983, Tillotson *et al.* 2011).

The concept of squirt flow introduced by Mavko and Nur (1975) addressed these two fundamental shortcomings of Biot theory. Squirt flow predicts much higher velocity dispersion at high frequencies and velocities that increase with increasing fluid viscosity. Squirt flow considers pressure gradients caused by elastic waves passing through the pores of a rock, causing fluid to flow along these pressure gradients. Therefore the fluid is squirted out of the more compliant parts of the pores into the stiffer parts during compression and flows back to its original position during dilation. This causes the velocity and attenuation of the elastic waves to depend on the frequency of the wave required to equalise the pressure in the pores. Squirt flow can be sensitive to a number of factors of the pore geometry and also to other lithological factors including the presence of clays (Klimentos and McCann 1990, Best and McCann 1995).

In the squirt flow theory, the characteristic frequency is inversely proportional to viscosity, the opposite of Biot, and thus shows better agreement with laboratory experimental data. In particular squirt flow is usually considered an important consideration at ultrasonic frequencies,

but is also thought to play a role at seismic and logging frequencies (Winkler 1985, Sams *et al.* 1997, Müller *et al.* 2010).

Gassmann's formulae were extended to the high frequency range by Mavko and Jizba (1991) by incorporating squirt flow theory. The model predicts the high frequency saturated moduli from dry rock properties. This model is therefore considered to be a macroscopic model, and does not require a description of the geometry of the pore scale that the microscopic models require. This theory was extended to the entire frequency range by Dvorkin *et al.* (1995) but does not include Biot theory as a mechanism. The model found that bulk dispersion and shear dispersion were proportional to each other. The model of Dvorkin *et al.* (1995) has been subsequently reformulated and refined by Pride *et al*. (2004). The new formulation is still consistent with Mavko and Jizba (1991), however parameterisation remains slightly ambiguous with the concept of the imaginary microporous grain (Müller *et al.* 2010).

An alternative approach was given by Murphy *et al*. (1986) who considered a pressure-relaxation approach between the compliant pores and gaps at the contact points between grains. However, this model is not consistent with Mavko and Jizba (1991) in the high frequency limit. Gurevich *et al*. (2010) recently proposed a new model based on the same pressure-relaxation approach of Murphy *et al*. (1986) combined with the tensor formulation of Sayers and Kachanov (1995). The result is a model which is consistent with the Gassmann and Mavko-Jizba equations at low and high frequencies, respectively.

An attempt to combine both the Biot and squirt flow mechanisms was made by Dvorkin and Nur (1993), known as the BISQ model. However, this model is not consistent with Gassman theory at zero frequency for saturated rocks, but is believed to be more suitable for partial gas saturation (Mavko *et al.* 1998).

The theory of Endres and Knight (1997) considers the magnitude of dispersion produced through squirt flow for a range of pore geometries. Their low-frequency findings (perfect pressure equalisation) are consistent with Gassmann theory and the high frequency (no fluid communication) with Hudson (1981). The main findings of the model

are that if only spherical pores are present there will be no bulk or shear dispersion. However, in the presence of an isotropic distribution of cracks and pores only the shear modulus is dispersive (for cracks with a constant aspect ratio). Between the two extremes bulk and shear dispersion are a function of the fraction of known porosity that is composed of cracks. Shear modulus dispersion is seen to be an increasing function of the crack fraction and that bulk dispersion reaches a maximum at a particular intermediate value of crack fraction.

The model of Chapman *et al.* (2002) combines the fundamental concepts of Endres and Knight (1997) and applies them to the entire frequency range. The model is also consistent with Gassmann at zero frequency and predicts the Biot slow wave. The model was tested by Chapman (2001) using the experimental data of Sothcott, McCann and O'Hara (2000) who measured velocity as a function of frequency, fluid saturation and effective stress using the resonant bar and ultrasonic pulse-echo techniques.

Although ultrasonic laboratory experiments provide accurate measurements of elastic wave velocity and attenuation, their applicability to low frequency field seismic data is difficult and requires a cautious approach. For this reason lower frequency systems used to measure the acoustic properties of fluid-saturated rocks can be of use. Of particular note is the work of Batzle *et al*. (2006) who reported P- and S-wave velocities between 5 Hz – 800 kHz for a series of sandstones and carbonates. The work used a low frequency forced-deformation technique for the low frequency measurements and pulse-transmission for the ultrasonic measurements. The work found that velocity dispersion and attenuation are influenced by fluid mobility (ratio of permeability to fluid viscosity) and may cause significant dispersion and attenuation even at seismic frequencies.

3.2 Equivalent medium theory for fractured media.

Homogenous material can become heterogeneous due to the presence of discontinuities, such as fractures and grain boundaries, or other steep gradients in material property changes. If the fractures show some degree of alignment then the overall properties of the medium will be anisotropic in the long-wave length limit. The assumption of aligned fractures is reasonable given that fractures at depth will tend to be orientated normal to the direction of minimum *in-situ* stress (Schoenberg and Sayers 1995).

Fractures within a medium are modelled using idealised shapes such as ellipsoids and flat discs (penny shaped) and are typically based on Eshelby's (1957) theory for the elastic response of an infinite elastic medium with an ellipsoidal inclusion within it. Several equivalent medium fracture models have been derived, however the theories of Schoenberg (1980), Hudson (1981) and Thomsen (1995) remain the most popular and most commonly used.

The simplest case for fractured reservoirs is a single set of totally aligned, isolated (with respect to fluid flow) fractures which are rotationally symmetrical (Müller *et al.* 2010). Schoenberg (1980) showed that in this case the elastic behaviour of the rock can be described by two parameters, the normal (Z_N) and tangential (Z_T) excess fracture compliances. When the fractures are dry or filled with gas Z_N and Z_T are of the same order (Schoenberg and Sayers 1995). However because the fractures are isolated, when the fractures are filled with fluid, Z_N vanishes and P-wave velocity parallel and perpendicular to the fractures becomes almost equal because the fluid has nowhere to flow to.

In the linear slip model of Schoenberg (1980) the fractures are modelled as planes of weakness with linear-slip boundary conditions. The elastic constants are therefore not derived from microstructural parameters. The overall stiffness tensor for this theory is found by adding the excess compliances of the fractures, S_F to the compliance of the background rock S_B and taking the inverse:

$$S = S_B + S_F \,, \tag{3.3}$$

$$C = S^{-1} \,, \tag{3.4}$$

where, S_F has the elements Z_N and Z_T.

The approach of Schoenberg (1980) allows additional fracture sets to be incorporated into the background rock by adding the respective excess compliance associated with each fracture set. However, the model is frequency independent and its usefulness for interpreting measured seismic anisotropy in terms of actual fracture properties is believed to be limited (Liu *et al.* 2000).

Hudson's (1981) model takes into account the propagation of seismic waves through a material with thin (compared to the wavelength of the seismic wave) embedded penny shaped fractures with a low fracture density ($\varepsilon_f \ll 1$). The model assumes that fluid (either gas, liquid or soft solid) is trapped within the fractures. The fluid does not connect between other fractures or the surrounding pores and therefore the model is limited to the high frequency range. The theory is a so called perturbation theory where the fractures are treated as a perturbation of the elastic moduli of the uncracked rock. The effective elastic tensor, C_{ijkl} of the fractured rock is given by

$$C_{ijkl} = C^0_{ijkl} + \varepsilon_f C^1_{ijkl} + \varepsilon_f^2 C^2_{ijkl} \,, \tag{3.5}$$

where, ε_f is the fracture density, given by equation 2.1, $C^0_{ijkl}$is the isotropic stiffness tensor, C^1_{ijkl} is the first order corrections due to the fractures and C^2_{ijkl} accounts for interactions between the fractures.

The first order correction, C^1_{ijkl} is a function of the elastic parameters of the unfractured medium and the response of a single isolated fracture to normal and shear tractions. This is also dependent on the aspect ratio of the fracture and the elastic moduli of the material

filling the fractures. The first order corrections are typically negative, and hence lower the elastic moduli from the unfractured modulus.

The model of Thomsen (1995) differs from that of Hudson by incorporating localised hydraulic connection between the pores of the matrix and the fractures, with the fluid pressure in both pores and fractures equal. With the assumption that localised fluid pressure equalisation occurs, it is limited to low frequencies, since the period of the wave is much longer than it takes for the time for the pressure to equalise. The model also takes into account anisotropic crack interactions described by Hoenig (1979). Comparing this model to the Rathore *et al*. (1995) data, Thomsen (1995) concluded that the flow of fluid between the fractures and the pores is a significant process, something not accounted for in the Hudson (1981) model, and for this reason matched the water saturated data of Rathore *et al*. (1995) more favourably than the Hudson (1981) model did. Gurevich (2003) showed that the static elastic moduli of a fluid-saturated rock with equant porosity can be obtained directly from the unfractured porous rock and fracture compliances using the equations of Brown and Korringa (1975). This approach therefore does not require the shape of the pores or fractures to be specified as long as their effect on the unfractured dry rock is known (Müller *et al.* 2010).

Both models of Hudson and Thomsen are frequency independent, with the Thomsen model representing the low frequency limit and the Hudson model the high frequency limit. There is a need for a model that can fill in the gap between the two frequency limits that might explain some seismic observations that cannot be explained by frequency independent behaviour (Liu *et al.* 2003, e.g. Maultzsch *et al.* 2003).

Neither the model of Thomsen or Hudson is able to distinguish the size of the fractures with their prediction of fracture density from measurements of seismic anisotropy. Knowledge of fracture size is important to hydrocarbon reservoir engineers; hence a remote and robust estimate of the fracture size, fracture-filling fluid type and fluid saturation would have a huge economic appeal.

The model of Hudson (1981) was extended to the entire frequency range by Hudson *et al.* (1996) by considering fluid flow between fractures. However, anomalies occur with the model: at zero frequency it does not reduce to Gassmann's theory, fluid flows along invisible fluid pathways between fractures and at seismic wavelengths velocity dispersion is only expected if the permeability of the rock is very high (>>1 Darcy).

The theory of Chapman (2003) models frequency-dependent seismic anisotropy in fractured reservoir rocks. The theory models velocity dispersion and velocity anisotropy which is frequency dependent with a result that is sensitive to fracture size (through shear-wave anisotropy) and to fluid type through a fluid mobility parameter, defined as the ratio of permeability to fluid viscosity. The model is particularly useful because it agrees with the Thomsen (1995) model and the Hudson (1981) model in the low and high frequency limits, respectively. In the absence of fractures, the low frequency limit of the model agrees with the formulation of Brown and Korringa (1975) and in the high frequency limit to the squirt flow model of Chapman *et al.* (2002). The model has ease of calibration and only requires one free parameter to be fitted to data (see chapter 3.4). It has also been used with some previous success, for example the sensitivity of shear-waves to frequency was shown and modelled in field seismic data by Maultzsch *et al*. (2003) and the sensitivity of attenuation anisotropy to fracture properties by Maultzsch *et al*. (2007).

It is for these reasons that I wish to test the validity of the Chapman (2003) model. I now describe the original Chapman (2003) and its applicability to the data that was collected.

3.3 Description of Chapman (2003) anisotropic fracture model.

The theory of Chapman (2003) is a poroelastic equivalent medium theory that considers a background medium consisting of spherical

pores with an isotropic, random distribution of ellipsoidal microcracks (identified with the grain scale size). It is based on the isotropic squirt flow theory of Chapman (2001) and Chapman *et al.* (2002) and incorporates a set of aligned fractures, thus rendering the fractured medium transversely isotropic (hexagonal symmetry). The fractures are allowed to be larger than the grain scale size, but their size and spacing must remain smaller than the seismic wavelength to fulfil equivalent medium theory criteria.

In the model by Chapman *et al.* (2002), fluid was exchanged between adjacent elements of pore space due to wave-induced pressure gradients according to D'Arcy's law; the mass flow between adjacent elements *a* and *b* is given by

$$\partial_t m_a = \frac{\rho_0 \kappa \varsigma}{\eta}(p_b - p_a)\,, \tag{3.6}$$

where m_a is the fluid mass in element, a, ρ_0 is the fluid density, κ is the permeability, ς is the grain size, η is the fluid viscosity and p_i is the pressure in the *i*th element.

It is assumed that each element is connected to six other elements. Since the fractures are larger than the pores they will be connected to more elements. It is also assumed that each pore or microcrack is connected to at most one fracture, and that the fractures are not connected to each other. Chapman (2003) then derived the expressions for the expected mass flow out of an individual fracture, microcrack and pore as a function of the inclusion pressure and applied stress. Chapman (2003) then solved these expressions for the time dependent pressure in the individual fractures, microcracks and pores due to an applied stress field.

The elastic constants were calculated using the Eshelby (1957) energy interaction approach for a medium with embedded inclusions. Using this approach, the stress and strain inside the inclusions were calculated using the derived time dependent pressures.

The elastic stiffness tensor given by Chapman (2003), C_{ijkl} is of the form

$$C_{ijkl} = C^0_{ijkl} - \Phi_p C^1_{ijkl} - \varepsilon_c C^2_{ijkl} - \varepsilon_f C^3_{ijkl}, \tag{3.7}$$

where Φ_p is the porosity, ε_c is the microcrack density, ε_f is the fracture density, C^0_{ijkl} is the isotropic stiffness tensor, C^1_{ijkl} is the contribution from pores, C^2_{ijkl} is the contribution from microcracks and C^3_{ijkl} is the contribution from fractures.

These corrections are functions of the Lamé parameters, the fluid and fracture properties, frequency and time-scale factors τ_m and τ_f which are the squirt flow time of the microcracks and fractures, respectively. Fluid flow in the model occurs on two scales, the grain scale (associated with the microcracks and pores) and the fracture scale. The relaxation time associated with the grain scale is related to the squirt-flow frequency (τ_m) while the flow associated with the fractures results in a lower characteristic frequency or time-scale constant (τ_f) related to the size of the fractures. The time scales τ_m and τ_f are themselves related through

$$\tau_f = \frac{a}{\varsigma}\tau_m, \tag{3.8}$$

where a_f is the fracture radius and ς is the grain size.

The parameter τ_m is given by

$$\tau_m = \frac{c_v \eta (1 + K_c)}{\sigma_c \kappa \varsigma c_1}, \tag{3.9}$$

where c_v is the volume of individual cracks, c_1 is the number of connections to other elements of pore space, $K_c = \frac{\sigma_c}{k_f}$, the inverse of

crack space compressibility, k_f is the fluid bulk modulus, $\sigma_c = \frac{\pi\mu r}{[2(1-v)]}$, the critical stress, r is the aspect ratio of the cracks and v is Poisson's ratio.

The model of Chapman (2003) is limited to a dilute concentrations of fractures, and therefore to a low porosity, because it uses the energy interaction approach of Eshelby (1957). To make Chapman's (2003) model more applicable to real data, it was adapted by Chapman *et al*. (2003) by introducing the Lamé parameters $\lambda^{o}$and μ^{o}which were derived from the density (ρ) and measured velocities, V_P^o and V_S^o, of the rock. The model also required a $C_{ijkl}^0(\Lambda, M)$ term, to be defined such that the fracture and pore corrections to velocities are applied at a specific frequency (f_0). This allows the model to be directly calibrated against the Lamé parameters taken from laboratory velocity measurements on rock samples. Subsequently, we have

$$\Lambda = \lambda^{o} + \Phi_{c,p}(\lambda^{o}, \mu^{o}, f_0)\,, \tag{3.10}$$

$$M = \mu^{o} + \Phi_{c,p}(\lambda^{o}, \mu^{o}, f_0)\,, \tag{3.11}$$

where $\Phi_{c,p}$ is an elastic tensor correction term that is proportional to ε_c and Φ_p

with,

$$\lambda^{o} = \rho(V_P^o)^2 - 2\mu^{o}\,, \tag{3.12}$$

$$\mu^{o} = \rho(V_S^o)^2\,, \tag{3.13}$$

Equation (3.5) is now written as

$$\begin{aligned} C_{ijkl}(\omega) = {} & C_{ijkl}^0(\Lambda, M, \omega) - \Phi_p C_{ijkl}^1(\lambda^{o}, \mu^{o}, \omega) \\ & - \varepsilon_c C_{ijkl}^2(\lambda^{o}, \mu^{o}, \omega) - \varepsilon_f C_{ijkl}^3(\lambda^{o}, \mu^{o}, \omega)\,, \end{aligned} \tag{3.14}$$

In this form the corrections for pores, microcracks and fractures which describe the frequency dependence and anisotropy of a material can be obtained from laboratory measurements on the rock (Maultzsch *et al.* 2003). Chapman *et al.* (2003) also showed that the model can be simplified further by setting the microcrack density (ε_c) to zero in cases of high porosity. In this case, it is assumed that the microcrack porosity is much smaller than the equant porosity of the rock, which holds true for most sedimentary reservoir rocks.

3.4 Model calibration.

With the reduction in the number of parameters required for the model, only the microcrack relaxation τ_m from equation 3.7 requires fitting to the model. τ_m is calibrated using the laboratory measured P- and S-wave velocity data and other measured quantities such as the fracture density using X-Ray CT scanning and porosity and permeability using standard techniques (see Chapter 4). The relaxation time for the fractures, τ_f is then calculated using equation 3.6.

3.5 Model predictions.

Important aspects of the model are reviewed in the following section using a series of synthetic examples with input parameters given in Table 3.1. In the absence of fractures, the model of Chapman (2003) reduces to the squirt flow model of Chapman *et al.* (2002).

P-wave velocity, V_P	4000 m/s
S-wave velocity, V_S	2750 m/s
Observation frequency, f_0	50 Hz
Bulk density of water saturated rock, ρ	2800 kgm^{-3}
Rock porosity, Φ_p	20%
Pore fluid bulk modulus (water), $\kappa_{f\ water}$	2.2 GPa
Microcrack density, ε_c	0.01
Fracture density, ε_f	0.02
Fracture radius, a	50 mm
Fracture aspect ratio, r	0.01
Microcrack time scale parameter, τ_m	8 x 10^{-9} s

Table 3.1: Rock and fluid parameters used to produce model predictions.

Figure 3.1 shows the model predictions in the absence of fractures. It can be seen that both P- & S-wave velocity dispersion and attenuation are expected in the megahertz frequency range due to microcrack fluid interactions. This dispersion and attenuation is related to the timescale parameter τ_m and is the traditional squirt flow frequency as predicted by Mavko and Jizba (1991).

If a set of fractures are introduced into the rock, is it rendered anisotropic (or transversely isotropic). In this anisotropic case, three waves can exist: a P-wave and two S-waves. One pure- and one quasi shear wave are polarized parallel (S1) and perpendicular (S2) to the fracture strike direction. Figure 3.2 shows the model result for wave propagation through a rock at 30° to the fracture normal using the fracture properties shown in Table 3.1. It can be seen that the P- and S2-waves show strong anisotropic velocity dispersion and attenuation in the kilohertz frequency range related to the fracture timescale parameter, τ_f, in addition to the microcrack dispersion at higher frequencies. The

S1-wave polarized parallel to the fracture shows no dispersion due to the fractures.

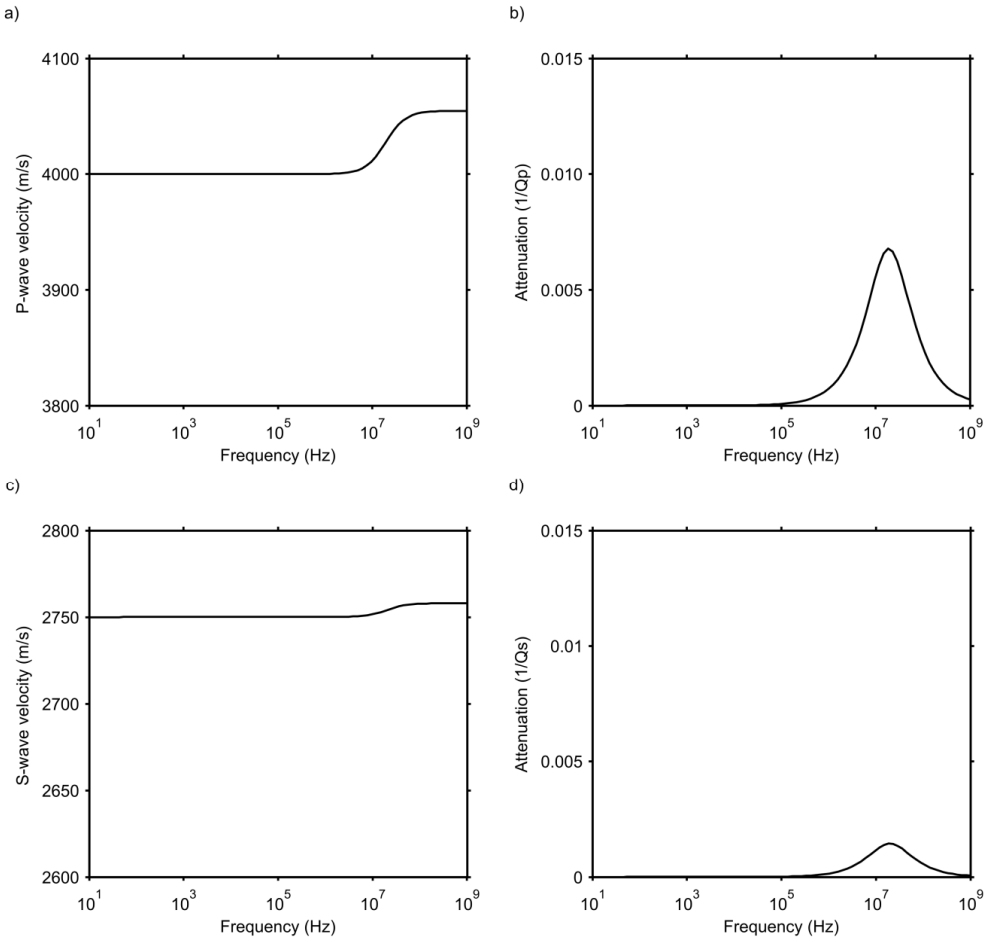

Figure 3.1: Velocity dispersion and associated attenuation for P-waves (a,b) and S-waves (c,d) due to grain scale microcracks (no fractures).

It can be seen that shear-wave splitting (SWS) is sensitive to frequency in Figure 3.2. Shear-wave splitting is defined by

$$\text{SWS}\,(\%) = \ 100 \ \times \frac{(S1 - S2)}{S1}, \tag{3.15}$$

Since τ_f depends on fracture size, and SWS depends on frequency for a single fracture size, the model predicts that SWS will be sensitive to

both fracture size and frequency (Figure 3.3). This sensitivity of SWS to fracture size and frequency has been demonstrated by Maultzsch *et al.* (2003) using VSP data.

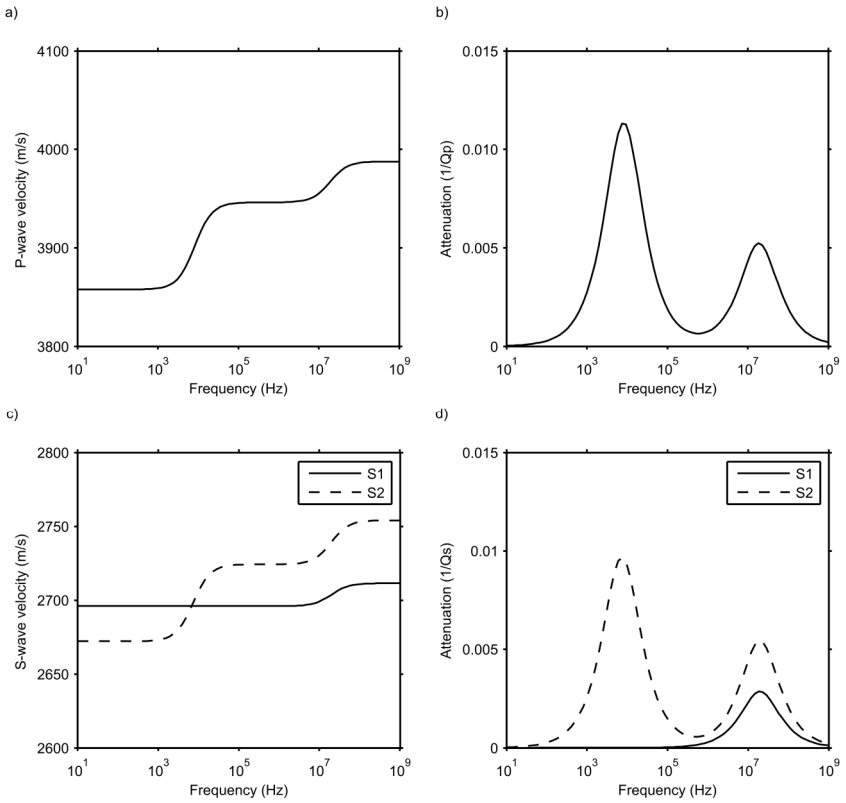

Figure 3.2: Velocity dispersion and associated attenuation for P-waves (a,b) and S-waves (c,d) due to microcracks and aligned meso-scale fractures at 30° to the fracture normal.

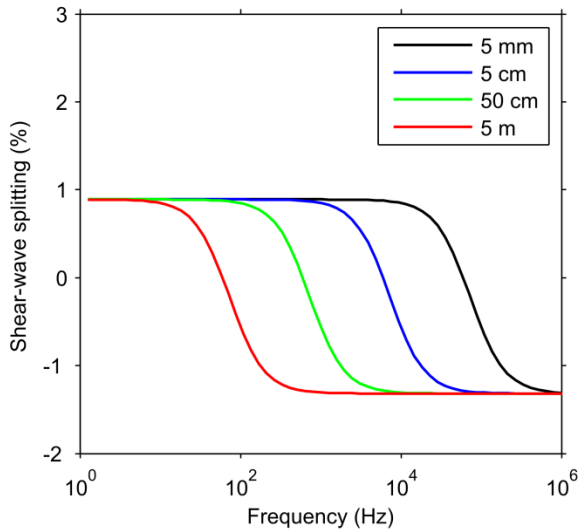

Figure 3.3: Shear-wave splitting as a function of frequency and fracture radius at 30° to the fracture normal.

Theoretical predictions of SWS and its relationship to fluid viscosity are shown in Figure 3.4. They show that SWS can be sensitive to fluid viscosity at a single frequency. This effect is caused by the fluid mobility parameter: the ratio of permeability to fluid viscosity. This sensitivity is of interest for oil/water discrimination based on fluid viscosity differences and could be detected using mode converted S-waves at typical, non-normal seismic incidence angles (30 - 45°).

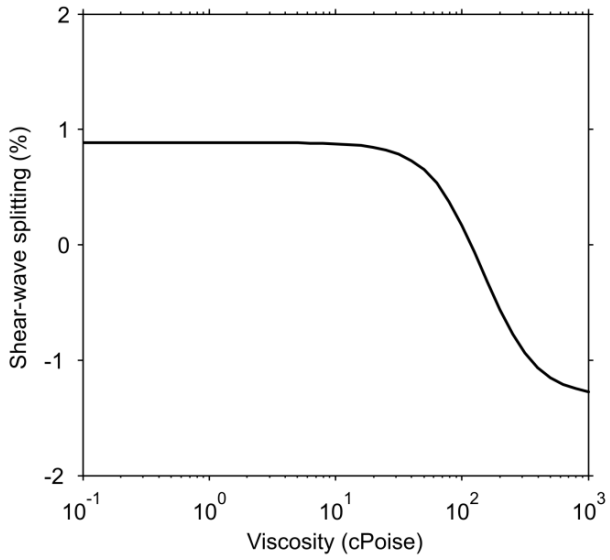

Figure 3.4: Shear-wave splitting at 50 Hz and at 30° to the fracture normal as a function of fluid viscosity.

The angular variations of P- and both S-wave velocity and attenuations are shown in Figures 3.5a and 3.5b, respectively. P-waves have a cosine 2θ azimuthal variation at 50 Hz. At higher frequencies (above 1 kHz), P-wave velocity has a cosine 4θ angular variance, shown in Figure 3.6a for a frequency of 750 kHz, the frequency at which our laboratory measurements are taken (Chapter 4). At higher frequencies it is not only the P-wave that is affected but also the S-waves. At angles between 0° and 45° to the fracture normal at 750 kHz it can be seen that the S2-wave can be faster than the S1-wave (Figure 3.6a). However, at 50 Hz the S1-wave is always greater than or equal to the S2-wave velocity (Figure 3.5a).

Attenuation due to the fractures also shows azimuthal dependence for P- and S2-waves relative to the fracture normal for both frequencies (Figures 3.5b and 3.6b). However, the S1-wave shows no attenuation at any azimuth with the presence of fractures for both frequencies. The theoretical results predict that at 750 kHz, attenuation will be larger than at 50 Hz for the P- and S2-waves.

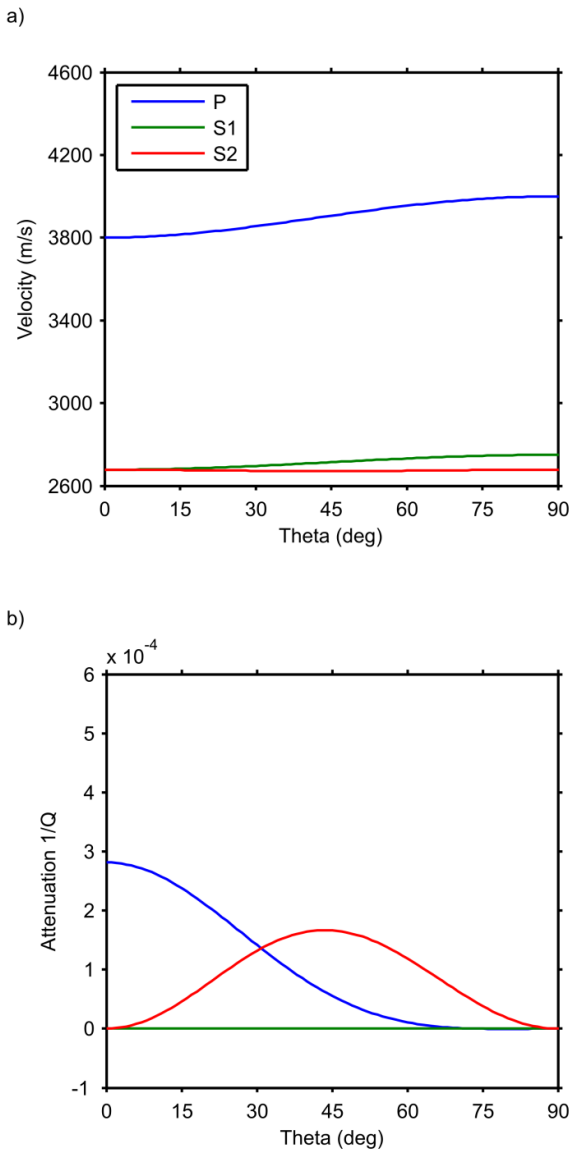

Figure 3.5: Azimuthal variations of velocity (a) and attenuation (b) relative to the fracture normal direction at 50 Hz.

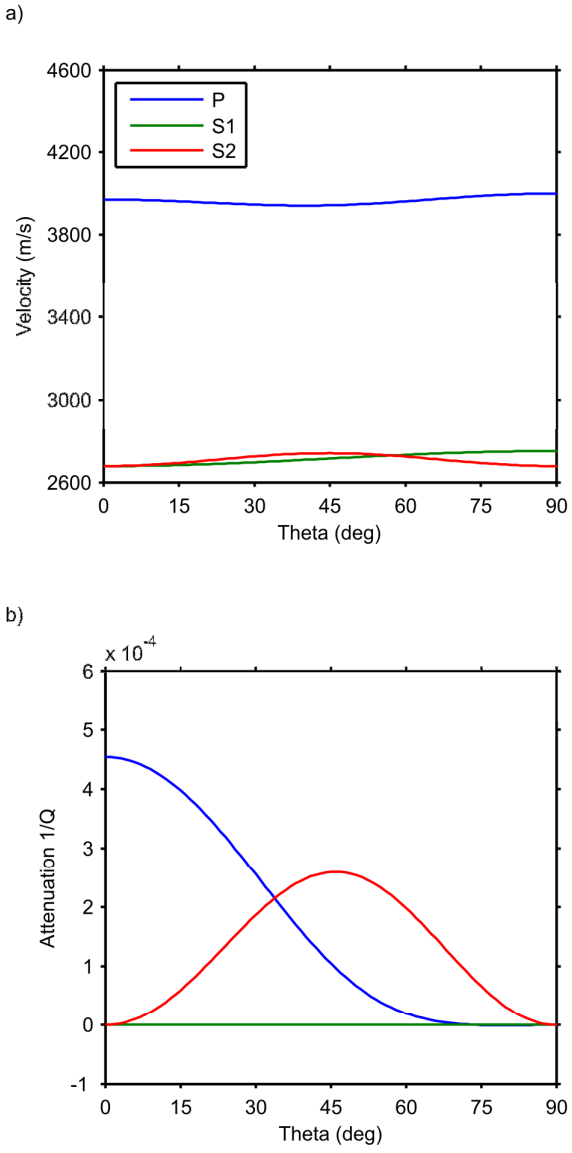

Figure 3.6: Azimuthal variations of velocity relative to the fracture normal direction at 750 kHz.

3.6 Conclusions.

Modelling of seismic anisotropy due to fractures is typically carried out with the models of Hudson (1981) and Thomsen (1995). Both these models give seismic anisotropy that is independent of frequency. The Hudson model represents the high frequency limit, where fluid is not able to flow between the fractures and the equant porosity of the rock. The model of Thomsen (1995) represents the low frequency limit, where fluid is able to flow between the fractures and the equant porosity. It was demonstrated by Rathore *et al.* (1995) that the fluid flow between the fractures and equant porosity was indeed an important aspect to consider, validating water saturated predictions of the Thomsen model in preference to the Hudson model.

Because neither of these models are frequency independent, shear-wave splitting remains the same at all frequencies for a particular rock. The theory of frequency-dependent seismic anisotropy in porous fractured rocks by Chapman (2003) predicts that anisotropic velocities and attenuation and in-particular, shear-wave splitting SWS can depend on fracture size, measurement frequency and fluid mobility. The model has the advantage that it agrees with the Biot-Gassmann theory in the absence of fractures, and with the Hudson model, and Thomsen model, in the high and low frequency limits, respectively. The model also has ease of calibration, with only one parameter, the microcrack relaxation time that requires fitting. Some evidence for the validity of the concept of frequency-dependent shear-wave splitting was provided by Maultzsch *et al.* (2003). Despite this it would be desirable to validate further aspects of the Chapman (2003) model so it's applicability to fractured reservoirs can be determined. The most sensible approach to do this requires laboratory experiments using rocks with controlled fracture geometries. To date, the only known example was the ultrasonic measurements of Rathore *et al.* (1995) on dry and water saturated, epoxy cemented rocks.

Chapter 4

Ultrasonic Experiments I (CNPC rocks).

This chapter forms an expanded version of the published paper in Appendix B:

Tillotson P., Chapman M., Best A. I., Sothcott J., McCann C., Shangxu W. and Li X. Y. 2011. Observations of fluid-dependent shear-wave splitting in synthetic porous rocks with aligned penny-shaped fractures. *Geophysical Prospecting* **59**, 111-119, doi: 10.1111/j.1365-2478.2010.00903.x.

Summary: This chapter describes the first set of laboratory experiments carried out at the National Oceanography, Southampton for my thesis. The purpose of the experiments was to obtain accurate measurements of P- and S-wave velocity and attenuation using the ultrasonic pulse-echo system on a set of synthetic, porous, fractured rocks provided by the China National Petroleum Corporation. The results were compared to aspects of the Chapman (2003). Although the wavelength to fracture size ratio infringed on the scattering regime in these experiments (values of less than 10 are considered to fall below the effective medium regime), there were nevertheless a number of important correlations with the theory. Notably, for wave propagation at 90˚ to the fracture normal, the observed values of shear-wave splitting of about 2% were one hundred times the fracture density (measured from image analysis of X-ray CT data) as predicted by theory. Moreover, the theory predicts

the observed angular variations of shear-wave splitting due to pore fluid viscosity changes.

4.1 Introduction.

A series of laboratory experiments were designed to analyse the seismic properties of a block of synthetic rock containing discrete aligned penny shaped voids manufactured by the Chinese National Petroleum Corporation's Key Laboratory. The manufacturing method was not know, so tools such as X-ray diffraction analysis, X-ray CT scanning and SEM imaging were used to characterise the physical properties of the synthetic rock.

The ultrasonic pulse-echo system was used to measure the seismic rock properties, namely P- & S-wave velocity (± 0.3%) and attenuation (± 20 dB/cm) for air dry, water and glycerin saturated samples up to an effective pressure (effective pressure = confining pressure – pore fluid pressure) of 60 MPa. The pore fluid pressure was kept at 5 MPa. Of particular use for this study was the ability to rotate the polarisation of the shear-wave transducer through 360˚ while maintaining the sample under elevated pressure. This allowed direct observations of shear-wave splitting associated with aligned fractures. Another advantage of the high pressures used and the pulse-echo geometry is that they ensure each sample has consistent coupling between the transducers, buffer rods and rock sample interfaces. This makes it a particularly reliable system for measuring attenuation as well as velocity.

Previous laboratory measurements on synthetic fractured rocks (e.g. Rathore *et al.* 1995) lacked sufficient accuracy for complete velocity and attenuation analysis and crucially lacked measurements with different pore fluid viscosities that can be used to validate theoretical models that predict the sensitivity of shear-wave anisotropy to viscosity in fractured rocks (e.g. Chapman 2003). The CNPC rocks in combination with the NOCS ultrasonic pulse-echo system offered an opportunity to address these issues.

The main drawback of the pulse-echo system for anisotropy studies is that it can only measure wave propagation in one direction through each sample. For this reason the large block was cored in three directions (0˚, 45˚ and 90˚ to the fracture normal) into small cylinders

(50 mm diameter, 20-30 mm length) to fit into the system. The success of the method therefore relied on the uniformity of the manufactured CNPC rocks. In practice, signal scattering from the relatively large fractures compared to the ultrasonic wavelength was such a problem that no useful data were recorded in the 0˚ sample. The data from the 45˚ and 90˚ samples were affected by scattering, so could not be considered to be representative of long-wavelength equivalent behaviour. This also meant that some input parameters (that would otherwise have been obtained from the 0˚ sample) for the Chapman model had to be estimated. Surprisingly, despite these drawbacks, some interesting observations were made that reinforce some theoretical predictions, even in the presence of strong scattering. Hence, the laboratory results may be expected to apply reasonably well to lower frequency, seismic datasets too.

4.2 Ultrasonic pulse-echo system overview.

Elastic wave properties; P- (compressional) and S- (shear) wave velocity and attenuation, were measured using the pulse-echo technique originally described by Winkler and Plona (1982) and implemented by McCann and Sothcott (1992). A full description of the system and its calibration can be found in Best (1992), however, a brief description is given here.

In the pulse-echo system these elastic properties are measured on pulses reflected from the top and bottom of a rock sample sandwiched between two Perspex (Lucite) buffer rods. The system offers significant improvements in accuracy and repeatability over transmission measurements, particularly for attenuation. For example, amplitude measurements are independent of any changes in the thickness of couplant between the transducer and buffer rod, or changes in coupling between the rock and buffer rods, a common problem with transmission measurements that require two separate experiments (one on the rock and another on a calibration material).

The main drawback of the pulse-echo system for seismic anisotropy studies is that it measures velocity and attenuation in a single direction only. For transverse isotropic materials such as the synthetically fractured rock samples studied here, measurements on three different cylindrical plugs (e.g. with waves propagating at 0˚, 45˚ and 90˚ to the fracture normal) are required to characterise the anisotropic tensor. Hence, for a valid characterisation of anisotropy, all three samples must have identical rock properties, including fracture size and distribution, so that the measurements can be considered to come from one material as a function of different wave propagation directions only.

A P- or S-wave transducer (see Figure 4.1) was used to transmit a broadband pulse through the buffer rod and record the reflected pulses from the top and bottom sample interfaces (ray paths A and B; Figure 4.1). A S-wave transducer was installed in the upper, rotatable transducer assembly, while a P-wave transducer was installed in the lower transducer assembly. The broadband pulses were recorded using a digital storage oscilloscope/PC at effective pressures of 10, 20, 30, 40, 50 and 60 MPa. The entire system was allowed to equilibrate for at least 30 minutes between pressure changes. The laboratory temperature and relative humidity were maintained at 20˚C and 55% respectively using an air conditioner unit.

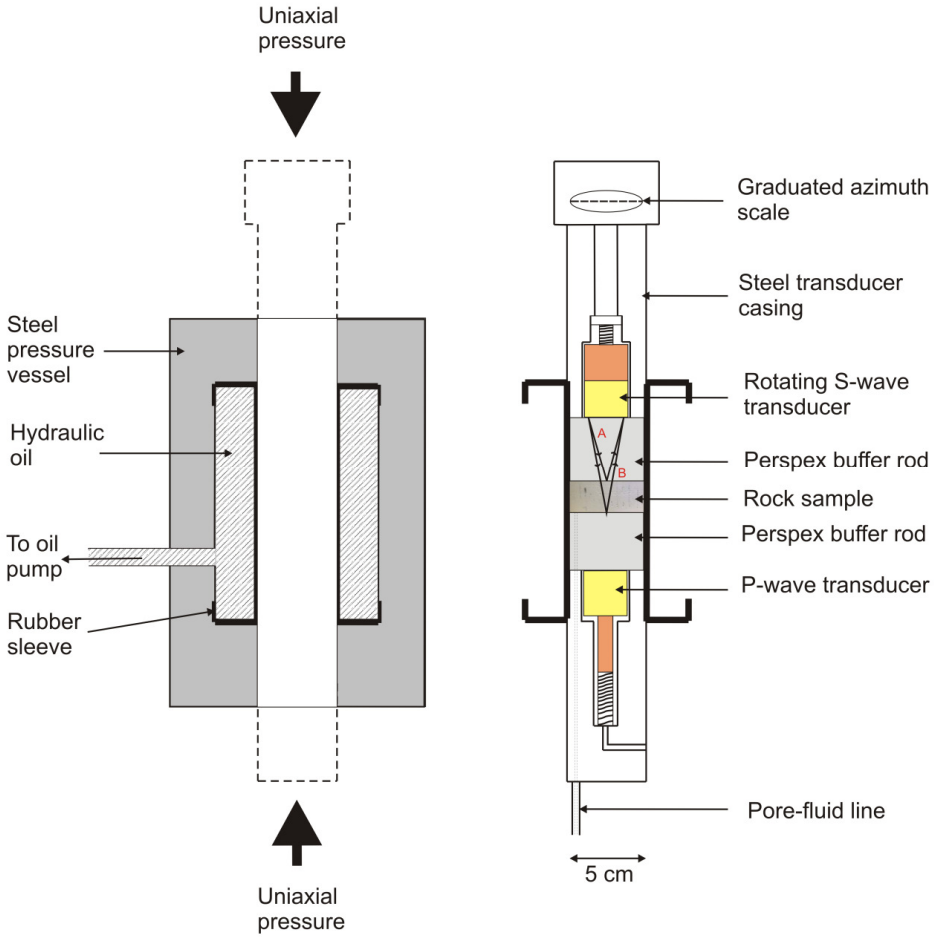

Figure 4.1: Cross-section through the ultrasonic pulse-echo system.

The whole system comprises a steel transducer housing, buffer rods and rock sample enclosed by a rubber jacket inside a hydraulic, Hoek-type, pressure cell mounted in a load frame (Figure 4.2). Pore fluid saturation is controlled through a pore fluid inlet at the base of the pressure cell, which connects to the base of the sample through the lower buffer rod, and is typically kept at 5 MPa. The hydrostatic confining pressure can be elevated up to 65 MPa. Hence, effective pressures up to 60 MPa can be achieved (effective pressure = confining pressure – pore fluid pressure).

Figure 4.2: The ultrasonic pulse-echo system when installed inside the Hoek high pressure cell and steel load frame.

4.3 Ultrasonic transducers.

A Panametrics type V102 P-wave transducer and a custom made Panametrics type V1540 S-wave transducer, both of nominal frequency 1 MHz, were used to generate ultrasonic pulses. The P-wave transducer was coupled to the lower buffer rod using Ultragel couplant, a commercially available, water based gel. The S-wave transducer was coupled using commercially available, shear-wave couplant with the consistency and appearance of black treacle; its viscosity is such that it behaves like a solid at high frequencies.

The S-wave transducer had two semi-circular crystals polarised at right angles to each other. However, in these experiments only one half was used to transmit and receive S-wave signals. The transducer

housing was designed to allow the S-wave transducer to be rotated on a thin film of shear-wave couplant while under confining pressure (Figure 4.3).

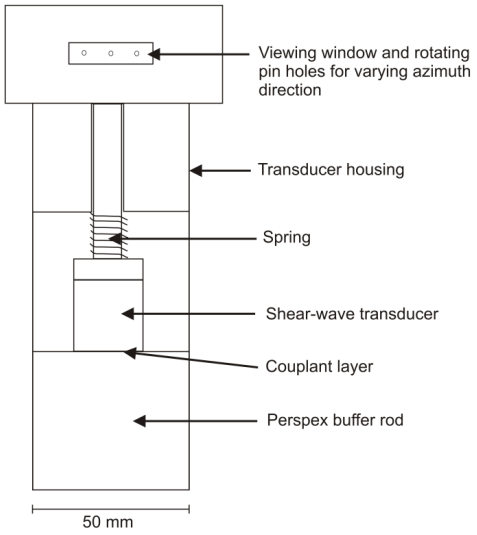

Figure 4.3: Shear-wave transducer housing. The design allows the transducer to be rotated for the measurement of azimuthal S-wave anisotropy under elevated pressures.

The transducer is held against the buffer rod using a spring inside the housing and rotated manually using a thin metal bar inserted into pin holes in a metal ring at the top of the housing. The system was designed so that it only fitted together one way for consistent azimuth angles relative to transducer orientation between experiments. Consistent re-assembly of the transducer housing was important because repeated rotation of the transducer eventually caused the coupling to degrade and then fail, thus affecting the signal to noise ratio. For this reason the transducer assembly was cleaned and S-wave couplant was reapplied after each experiment.

4.4 Pulse generator.

An Avtech AVR-1-PW-C-P pulse generator was used to provide broadband pulses with frequency content between 500 to 1500 kHz. Spectral analysis was used to calculate phase velocity and attenuation within this frequency range. A typical broadband pulse is shown in Figure 4.4a and the top and base reflections spectral content in Figures 4.4b and 4.4c, respectively. The first pulse is from the top of the rock and buffer rod interface, and the second (phase reversed) from the base of the rock sample and buffer rod interface. The spectral content of an actual rock sample in Figures 4.4b and 4.4c shows the amplitude is spread broadly between frequencies of 200 and 1200 kHz for both the top reflection and base reflection.

The pulses were viewed using a LeCroy digital storage oscilloscope and stacked between 500 and 1000 times to improve the signal to noise ratio. The signals were then saved as binary files on either a floppy 3.5" disk or via a direct data connection to a PC. Conversion of the binary files to ASCII was done using the ScopeExplorer software provided by LeCroy.

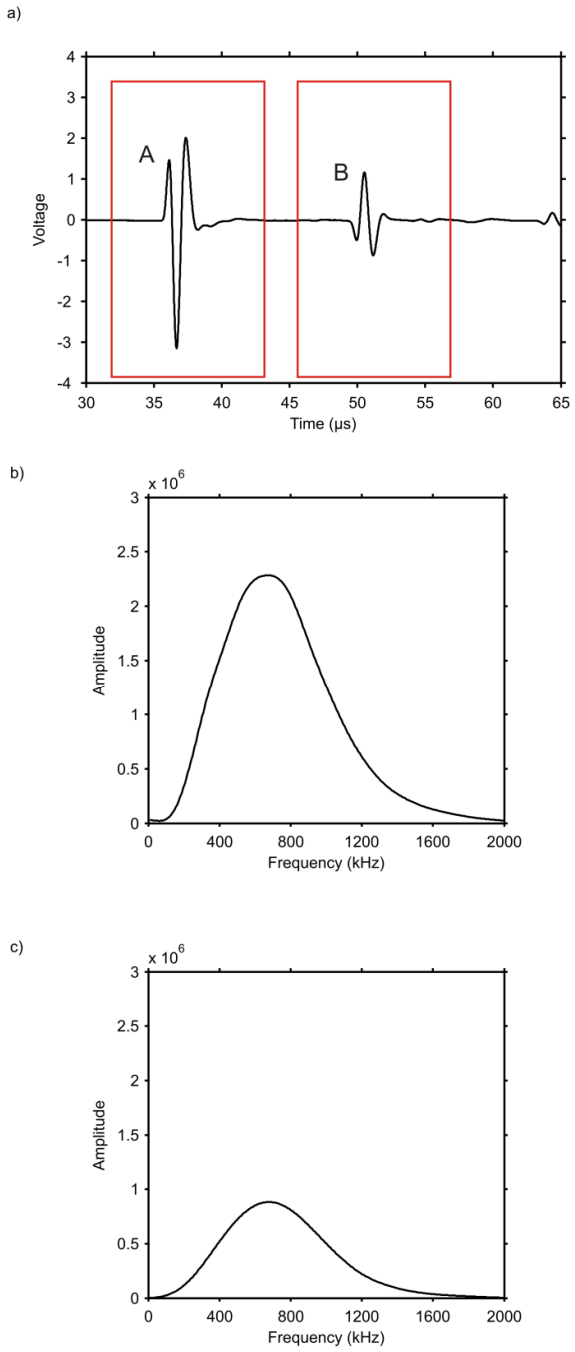

Figure 4.4: Example pulse-echo waveforms using a broadband frequency pulse (a). A and B refer to the ray travel paths shown in Figure 4.1. The red boxes in 4.4a indicate the windows for each wavelet required for Fourier analysis. The spectral content of top and base reflections are shown in (b) and (c), respectively.

4.5 Diffraction corrections.

The phase and amplitude of waveforms transmitted by the transducers require corrections for diffraction effects as a result of interference between energy transmitted from different points on the transducer face (Huygen's principle). The diffraction corrections are related to path length, the frequency and diameter of the transducer. The resulting phase changes lead to an apparent decrease in travel-time, thus giving rise to a higher than expected sample velocity. Diffraction effects also lead to higher apparent attenuations than the true values. Papadakis (1972) formulated P-wave phase and attenuation corrections for a finite circular broadband transducer. These were tabulated by Benson and Kiyohara (1974) and graphed by Papadakis *et al.* (1973).

The corrections are computed in terms of a normalised distance, S, from the transducer using,

$$S = \frac{z\lambda}{r_t{}^2} = \frac{z\mathrm{V}}{r_t{}^2 f}, \tag{4.1}$$

where, z is the distance from the source (m), λ is the wavelength (m), r_t is the transducer radius (m), V is the velocity of the wave (m/s) and f is the frequency (Hz).

Although the Benson & Kiyohara (1974) diffraction corrections strictly relate to P-waves radiating into an infinite medium, the same corrections were applied for S-waves because there are no published diffraction correction for them. However, Klimentos and McCann (1990) showed that these diffraction corrections were reliable for both P- and S-waves. Further work by McCann and Sothcott (1992) and Best (1992) using aluminium and brass materials showed P-wave diffraction corrections gave good predictions for S-wave corrections and that velocity could be measured to an accuracy of ± 0.3% and attenuation to ± 0.1 dB/cm for single head transducers and ± 0.2 dB/cm for dual head transducers.

The dual S-wave transducer is split into two semicircular halves, one polarized orthogonally to the other, with an effective radius of each half of 0.89 cm. Since this radius is smaller than for the circular P-wave transducer (1.27 cm) it results in a larger normalised distance, S and larger diffraction corrections.

4.6 Calculation of phase velocity.

The phase velocity of the rock, an initial estimate of which is needed to calculate the diffraction corrections, is calculated using,

$$\mathrm{V_{P/S}}(f) = \frac{2L_R}{\left(t_B - \frac{\Phi_B(f)}{2\pi f} - \frac{1}{2f}\right) - \left(t_A - \frac{\Phi_A(f)}{2\pi f}\right)}, \tag{4.2}$$

where, $\mathrm{V_{P/S}}(f)$ is the P- or S-wave velocity (m/s) at frequency, f, L_R is the length of the rock sample (m), t_A is the window start time for pulse A, t_B is the window start time for pulse B, $\Phi_A(f)$ is the Fourier phase angle spectrum for pulse A (radians), at frequency, f and $\Phi_B(f)$ is the Fourier phase angle spectrum for pulse B. The term $\frac{1}{2f}$ is included to correct the base reflection for the 180˚ phase change.

For each frequency, the corrected travel time, $t_{corr}(f)$ is given by

$$t_{corr}(f) = t_{meas}(f) + \Delta t(f), \tag{4.3}$$

where, $t_{meas}(f)$ is the measured difference in travel time between the top and base reflections (s) and $\Delta t(f)$ is the diffraction correction given by

$$\Delta t(f) = \frac{\Phi_{S_B}(f) - \Phi_{S_A}(f)}{2\pi f}, \tag{4.4}$$

where, $\Phi_{S_B}(f)$ is the phase lag of the base reflection at normalised distance S_B (radians) at frequency, f and $\Phi_{S_A}(f)$ is the phase lag of the top reflection at normalised distance S_A.

It is important that the length of the samples is accurately calculated for accurate velocity and attenuation results. This was achieved by grinding the top and bottom faces of the rock samples parallel to an accuracy of ± 0.005 mm, then taking a mean of seven length measurements in a regular pattern around the sample using a digital micrometer accurate to 1μm at room temperature and pressure.

4.7 Calculation of intrinsic attenuation coefficient.

The intrinsic attenuation coefficient is defined as the loss of amplitude per unit distance or the fractional loss of energy per wavelength. It is calculated according to:

$$\alpha(f) = \frac{8.686}{2L_R} \ln\left[\left(\frac{A_A(f)}{A_B(f)}\right)(1 - R^2(f))\right], \tag{4.5}$$

where $\alpha(f)$ is the attenuation coefficient (dB/cm) at frequency, *f*, $A_A(f)$ is the Fourier amplitude spectrum of the top reflection and $A_B(f)$ is the Fourier amplitude spectrum of base reflection. $R(f)$ is the reflection coefficient given by the Zoeppritz's (1919) equations for waves at normal incidence which reduce to (Mavko *et al.* 1998):

$$R(f) = \frac{\rho_R \mathrm{V}_R(f) - \rho_P \mathrm{V}_P(f)}{\rho_R \mathrm{V}_R(f) + \rho_P \mathrm{V}_P(f)}, \tag{4.6}$$

where ρ is bulk density and the subscripts R and P refer to the rock sample and Perspex buffer rods, respectively.

Quality factor, Q, is defined (valid for Q > 10) by

$$\mathrm{Q}(f) = \frac{\pi f}{\mathrm{V_{P/S}}(f)\alpha(f)}, \tag{4.7}$$

Amplitude changes caused by diffraction effects as a function of the normalised distance from the transducer face are listed in the Benson and Kiyohara (1974) tabulated data and are calculated from;

$$\Delta\alpha(f) = \frac{\alpha_{S_B}(f) - \alpha_{S_A}(f)}{2L_R}, \tag{4.8}$$

where $\Delta\alpha(f)$ is the attenuation diffraction correction (dB/cm) at frequency, f, $\alpha_{S_B}(f)$ is the diffraction loss (dB) for the base reflection at normalised distance $S_B(f)$, for base reflection and $\alpha_{S_A}(f)$ is the diffraction loss (dB) for the top reflection at normalised distance $S_A(f)$.

The corrected attenuation, $\alpha_{corr}(f)$ is therefore calculated using,

$$\alpha_{corr}(f) = \alpha_{meas}(f) + \Delta\alpha(f), \tag{4.9}$$

where $\alpha_{meas}(f)$ is the measured attenuation coefficient (dB/cm).

4.8 Phase or group velocity.

A question that arises is whether at 45° to the fracture normal, phase or group velocity is measured using the pulse-echo system. Dellinger and Vernik (1994) modelled propagation of P- and S-waves through an anisotropic medium. They considered the wavefronts to have a finite width when using an ultrasonic transducer with a radius between 6 – 10 mm. If the wavefront is travelling parallel or perpendicular to the fracture normal, a true phase velocity is measured. At 45° to the fracture normal, the wavefront can suffer a lateral translation dependent on the

degree of anisotropy and propagation distance through the sample. If this translation is larger than the radius of the receiving transducer then a group velocity, not phase velocity, is measured. The lateral translation for P and SV-waves is given by,

$$D = H\frac{(V_P(90)^2 - V_P(0)^2)}{2V_X(45)^2} \times \frac{(V_{SV}(90)^2 + V_{SV}(0)^2) - 2V_X(45)^2}{(V_P(90)^2 + V_P(0)^2) + (V_{SV}(90)^2 + V_{SV}(0)^2) - 4V_X(45)^2}, \quad (4.10)$$

and the lateral translation for SH-waves given by,

$$D = H\frac{V_{SH}(90)^2 - V_{SH}(0)^2}{2V_{SH}(45)^2}, \quad (4.11)$$

The parameter, D is the total lateral displacement (m), H is the core height/length (m), $V_P(\theta)$ is the P-wave velocity at angle θ from the fracture normal (degrees), $V_{SV}(\theta)$ is the SV or S2 -wave velocity at angle θ from the fracture normal (degrees), $V_X(\theta)$ is $V_P(\theta)$ or $V_{SV}(\theta)$ depending on wave under consideration, and $V_{SH}(\theta)$ is SH or S1-wave velocity at angle θ from the fracture normal (degrees).

The maximum lateral translation was calculated to be 0.31 mm for P-waves at 50 MPa (less than 10% of the radius of the receiving transducer in our experimental setup). Since S-waves suffer lower lateral translations than P-waves from equation 4.11, all wavefronts therefore have a lateral translation an order of magnitude less than the radius of the receiving transducer. This confirms that pulses travelling through the rock sample to the base buffer rod rock interface are reflecting from the base of the rock and not translated past the base of the rock onto the side of the rock. The conclusion from the calculation confirms phase velocity is measured at 45˚.

4.9 Technique for measuring anisotropy.

P-wave anisotropy was measured using different samples with different fracture orientations. This was successfully measured in the samples with fractures orientated at 90° and 45° to the fracture normal. The sample with 0° fractures was too highly attenuating for meaningful results.

S-wave anisotropy was measured by rotating the S-wave transducer to measure the maximum and minimum travel-times in the sample with fractures orientated at 90° to the fracture normal (see Best *et al.* 2007 for anisotropic measurement procedure) and calculated using equation 3.13. In this case the minimum travel-time represents the S1 (fast) shear-wave polarized parallel to the fractures, and the maximum travel-time the S2 (slow) shear-wave polarized perpendicular to the fractures.

In the sample with fractures orientated at 45° to the fracture normal the velocity difference between the S1 and S2 wave will not be as obvious (since the S2 wave can theoretically be faster e.g. Figure 3.6). To ensure the S1 and S2 were correctly measured in the 45° sample the polarization of the shear-wave transducer was lined up parallel with the fracture strike to measure the S1-wave, and perpendicular to the fracture strike to measure the S2-wave. This removed any ambiguity in the S-wave polarization direction.

The error associated with the shear-wave splitting measurement was calculated by combining the errors of each velocity measurement involved in the calculation of shear-wave splitting (Equation 3.13). Since the error in velocity measurement is ±0.3%, the shear-wave splitting error is 0.3% + 0.3% + 0.3% = 0.9%. The largest measured shear-wave splitting is 2.39% (Figure 4.20b), therefore the largest error is 0.9% of 2.39 giving ± 0.02%. This is the error associated with the shear-wave splitting measurements in this experiment using the pulse-echo system. Since this value represents the worst case scenario, it is used as an error for all other shear-wave splitting measurements for the experiments reported below.

4.10 China National Petroleum Corporation sample description.

A block of a novel synthetic porous rock with aligned penny-shaped voids (fractures) was provided by the Chinese National Petroleum Corporation's (CNPC) Key Laboratory for experimental investigation using the pulse-echo system. The block was cored into three plugs of diameter 50 mm and length 20-30 mm (Figure 4.5) using a diamond corer and water flush.

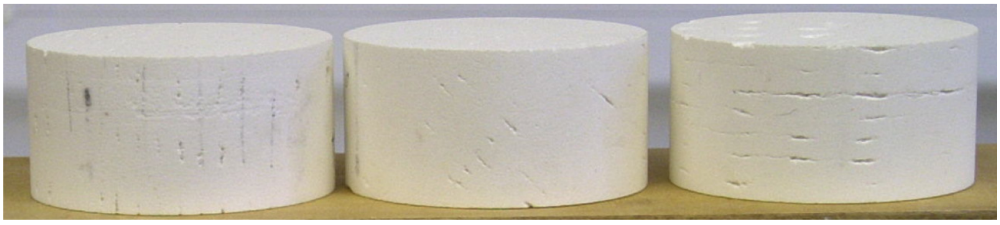

Figure 4.5: Synthetic rock samples (diameter 50 mm) cored at 90˚ (left), 45˚ (centre) and 0˚ (right) to the fracture normal from the same block.

The plugs were subjected to the standard methods: helium porosimetry (porosity and density), nitrogen permeametry (Klinkenberg corrected permeability), X-ray diffraction analysis (mineral composition; carried out by Ross Williams at the National Oceanography Centre, Southampton), X-ray CT scanning (size, density and distribution of the fractures) and SEM imaging (grain size/sorting and close up images of the fractures). These properties are listed in Table 4.1.

Parameter	Units	Value
Rock properties		
[a]Equant porosity, φ_p	%	29
[a]Grain density, ρ_g	$kg.m^{-3}$	3576
[b]Grain mineralogy	-	Sodium Aluminium Oxide
[c]Mean grain radius, ζ	μm	20
[d]Permeability	mD [1 mD = 1 x 10^{-15} m^2]	25
[e]*Fracture properties*		
Fracture density, ε_f	-	0.0201 ± 0.0068
Fracture radius	mm	1.8 ± 0.19
Fracture aspect ratio, r	-	0.01
Microcrack density, ε_c	(see Chapman et al. 2003)	0
[f]*Fluid properties*		
Water density	$kg.m^{-3}$	998.2
Water bulk modulus	GPa	2.19
Water viscosity	cP [1 cP = 1 x 10^{-3} Pa.s]	1
Glycerin density	$kg.m^{-3}$	1225
[g]Glycerin bulk modulus	GPa	4.40
[h]Glycerin viscosity	cP	100

[a]Helium porosimetry, [b]XRD, [c]SEM estimate, [d]Nitrogen permeametry, [e]X-ray CT image analysis, [f]from Kaye & Laby, [g]Measured on sample from identical block without fractures, [g]Measured in a special cell using P-wave velocity, [h]Measured using a viscometer

Table 4.1: Petrophysical and fracture properties.

4.11 X-ray CT scanning for fracture density determination.

High resolution X-ray CT scanning can be an effective tool for analysing internal properties of material and has been used by the medical industry for many years. Newer portable X-ray CT scanning devices allow scanning on small scale at a fast and reasonable cost. To get an internal

image of the CNPC rocks they were X-ray CT scanned using an X-TEK Benchtop CT 160Xi scanner (Figure 4.6) located in the School of Engineering Sciences at the University of Southampton.

Figure 4.6: X-TEK Benchtop CT 160Xi scanner with sample inside.

The small scanner has a resolution of about 50 μm and is ideal for locating and quantifying the penny shaped voids within the CNPC rock samples. Image analysis of the scan data was carried out using VGStudio MAX software by Volume Graphics.

Two types of images were obtained: single slices (Figure 4.7), and a 3D volume (Figure 4.8). The 3D volume was particularly useful for determining the fracture density since it allowed the number of fractures within a plug to be counted within an estimated error or ± 1. To calculate the radius of the samples 20 identified fractures were measured and a mean average found. Fracture density was then calculated using equation 2.10 and found to be 0.0201 ± 0.0068. The error was calculated using the law of combinations of errors (Barlow 1989).

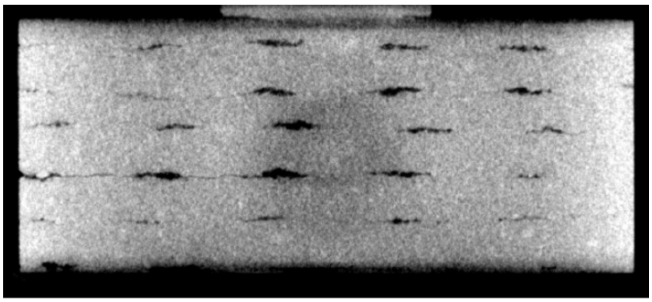

Figure 4.7: X-ray CT scan image slice through the CNPC rock. It shows the cross sectional distribution and variation in the penny shaped fractures. Hairline fractures can be seen between some of the penny shaped fractures.

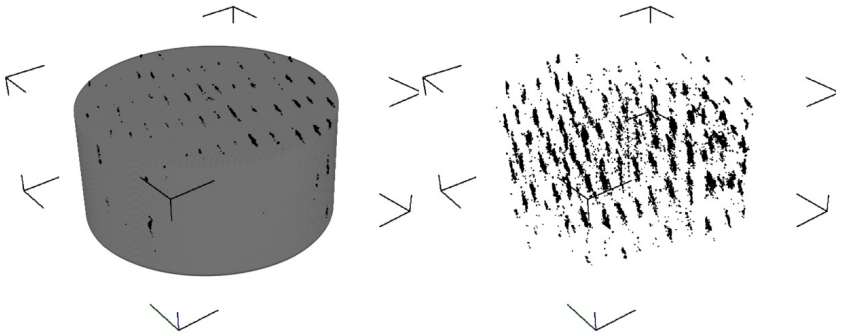

Figure 4.8: 3D volume image from CT scan. It shows the position of the fractures in the vertically fractured plug. This allowed an accurate calculation of the fracture density to be made.

4.12 Scanning Electron Microscope (SEM) imaging.

SEM imaging provides a useful tool for imaging the fine surface structure of a rock. For this work it was used to determine the average size of the grains and to view more closely the shape of the penny shaped fractures within the CNPC samples. Imaging was acquired using a Hitachi TM-1000 Tabletop Microscope and corresponding software. An example of an image used for analysis can be seen in Figure 4.9. It

shows that the synthetic rock is fine grained with an average grain diameter of around 20 μm. The image also shows that the fractures have some kind of detritus material in them. This is presumably from the manufacturing process to create the penny shaped fractures.

Figure 4.9: SEM image example showing grain size variation and material within the penny shaped void. Note scale bar is 100 μm in the bottom left hand corner.

4.13 Technique for saturating samples.

Samples were measured air, water (1 cPoise) and glycerine saturated (100 cPoise). Viscosities were measured using standard viscometer techniques. The air saturated samples were held in a vacuum desiccator suspended over a saturated salt solution providing a repeatable relative humidity of 55%.

Samples were saturated with either water or glycerin using a method devised by Jeremy Sothcott. The method ensured as complete saturation as possible throughout the sample. Firstly a sample is evacuated to 10^{-3} Pa by a diffusion pump and then immersed in de-gassed distilled de-ionised water or glycerin while still under a vacuum. The water or glycerine pressure is then raised to 7 MPa and the sample is left overnight and finally stored in a jar totally filled with water or glycerin.

4.14 Laboratory results.

Measurements are presented for P- and S-wave velocity on two samples taken at 50 MPa (to reduce any effects caused by the hairline fractures seen in Figure 4.7) saturated with water or glycerin. The two samples have fractures orientated at 90° and 45° to the fracture normal. A third sample with fractures orientated at 0° to the fracture normal was too highly attenuating to get meaningful results.

Measurements of attenuation are only presented for P- and S-waves from the 90° sample. Without the full elastic tensor (i.e. no measurements in the 0° sample) it is not possible to correct for the anisotropic reflection coefficient for measurements in the 45° sample used to calculate attenuations (see Appendix A for a discussion of the anisotropic reflection coefficient). However, calculations of velocity remain valid as they are based on travel-time differences.

In particular, the shear-wave splitting observations showed good agreement with theory and will be the main focus of the results.

4.14.1 Fractured rock P-wave velocity anisotropy.

Measurements of P-wave velocity on the samples with fractures orientated at 45° and 90° to the fracture normal and at 50 MPa show that levels of dispersion are generally low. Changing the fracture azimuth from 90° to 45° is seen to reduce velocity by 49 m/s when water saturated (Figure 4.10a), and 43 m/s when saturated with glycerin (Figure 4.10b). P-wave velocity dependence on viscosity is seen to be high from the laboratory measurements. For example at 90° to the fracture normal, an increase of 227 m/s at 750 kHz is measured, while at 45° to the fracture normal, an increase of 233 m/s at 750 kHz is measured when the samples are saturated with glycerin compared to when they are saturated with water.

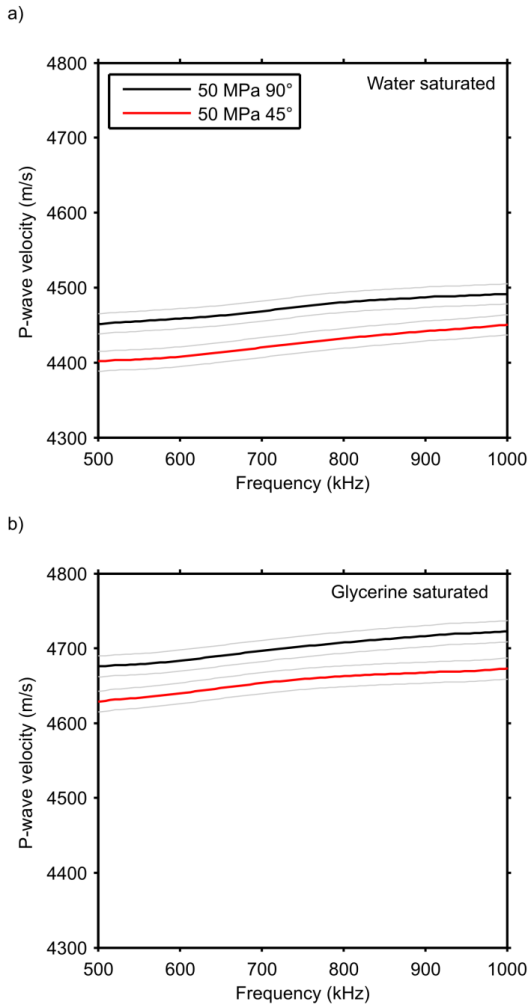

Figure 4.10: P-wave velocity versus measurement frequency in the 90˚ and 45˚ samples when saturated with (a) water and (b) glycerin.

4.14.2 Fractured rock P-wave attenuation.

Attenuation in the 90° sample for both water and glycerine saturated show almost identical trends and magnitudes (Figure 4.11). They both rise from Q^{-1} of 0.02 (Q = 50) at 500 kHz, and flatten off with Q^{-1} of 0.035 at 750 kHz up to 1000 kHz. Error bars are set at 10% of the measured attenuation value, representing the worst case scenario for the error in attenuation measurement.

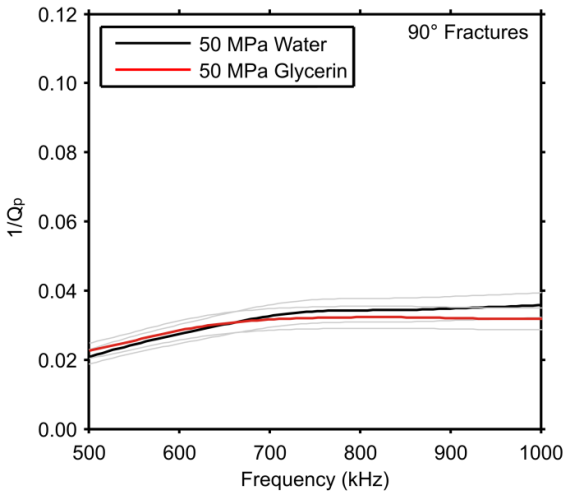

Figure 4.11: Water and glycerin saturated attenuation (1/Q) versus measurement frequency at 90˚ to the fracture normal.

4.14.3 Fractured rock S-wave velocity anisotropy.

The S-wave pulse reflections from the base of the samples are presented in Figure 4.12. For the 90˚ sample, significant time differences are seen between orthogonally polarized S-waves corresponding to inline and transverse directions relative to the aligned fractures (e.g., compare time shift between peak amplitudes of waveforms).

These time delays are approximately the same for both the water (Figure 4.12a) and glycerin (Figure 4.12b) saturated cases. However in the 45˚ sample the time delay becomes much smaller for both water and glycerin. When water saturated (Figure 4.19c), the waveform for S-wave polarization at 0˚ to the fracture direction arrives at the same time as the arrival for 90˚. However when the 45˚ sample is glycerin saturated (Figure 4.12d) the waveform for S-wave polarization at 90˚ to fracture direction arrives just before that at 0˚. The corresponding S-wave phase velocities are also presented in Figures 4.13 and 4.14 for a differential pressure of 50 MPa when any undesired fractures are closed leaving only the desired penny-shaped voids.

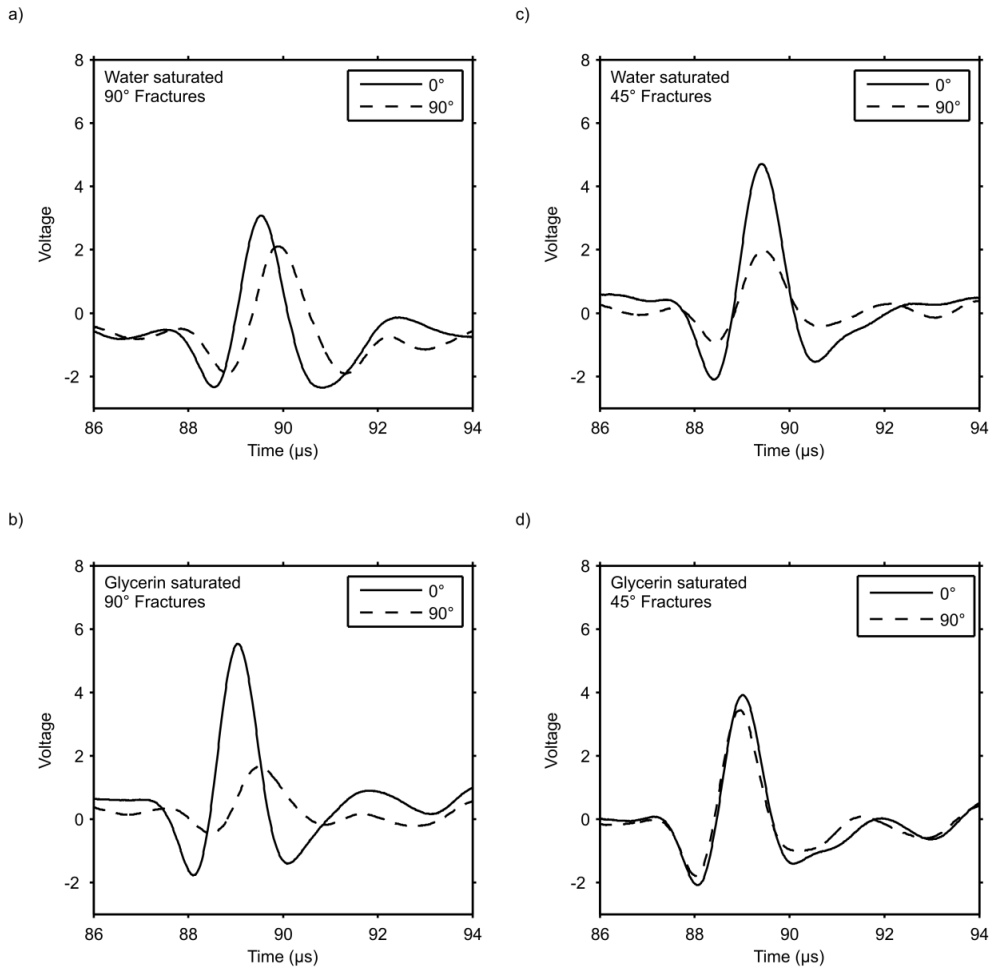

Figure 4.12: S-wave pulse reflections from the base of the 90˚ sample saturated with (a) water and (b) glycerin, and from the 45˚ sample saturated with (c) water and (d) glycerin. S-wave polarizations relative to fracture direction indicated in legend.

Shear-wave splitting (SWS) is expressed as the parameter SWS (%) = 100 x (S1 - S2)/S1 (equation 3.13), where S1 and S2 are the parallel and perpendicular shear-wave velocities relative to the fracture direction, respectively. Significant shear-wave splitting of about 2% was observed in the 90˚ sample for both the water saturated (Figure 4.13a) and glycerin saturated (Figure 4.13b) cases. However, in the 45˚ sample the magnitude of shear-wave splitting is seen to change with fluid type. Shear-wave splitting reduces to 0.00 ± 0.02% in the water saturated 45˚ sample in Figure 4.14a, and is -0.77 ± 0.02% in the glycerin saturated 45˚ sample in Figure 4.14b.

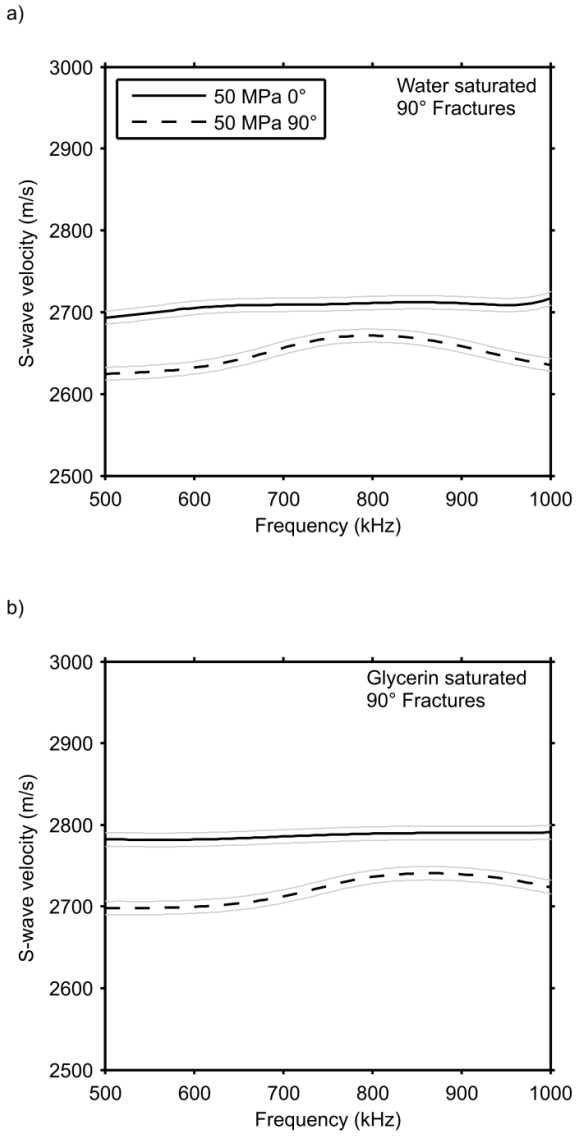

Figure 4.13: S-wave velocities versus measurement frequency in the 90˚ sample when saturated with (a) water and (b) glycerin. S-wave polarizations relative to fracture direction indicated in legend.

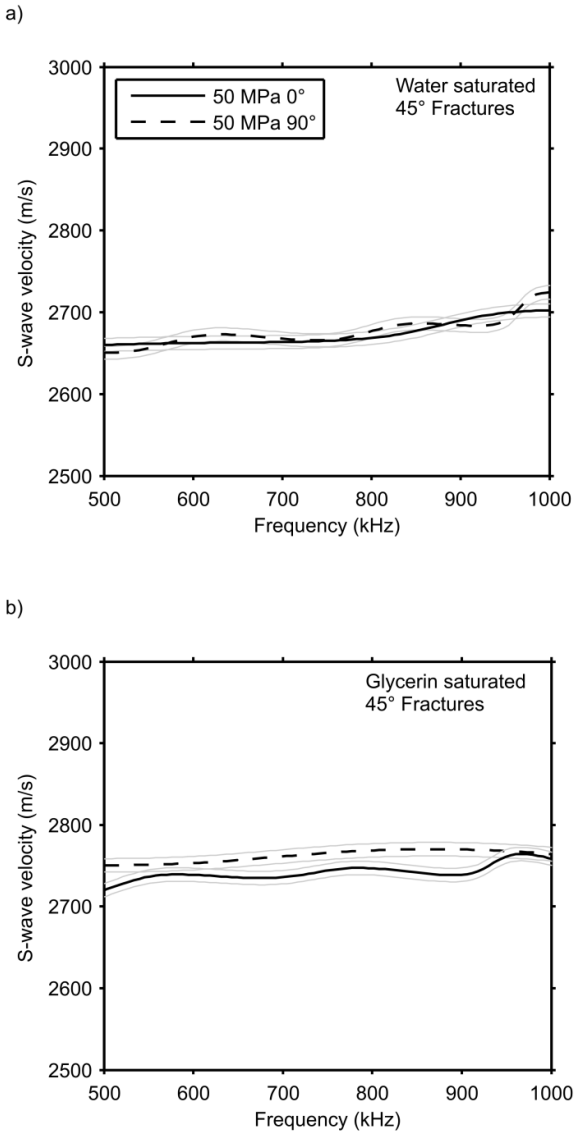

Figure 4.14: S-wave velocities versus measurement frequency in the 45˚ sample when saturated with (a) water and (b) glycerin. S-wave polarizations relative to fracture direction indicated in legend.

4.14.4 Fractured rock S-wave attenuation.

Measurements of attenuation when water saturated and at 90˚ to the fracture normal show the magnitude of S2 attenuation is generally higher than that of the S1 (Figure 4.15a) with Q^{-1} for S1 around 0.04 and S2 around 0.06 at 750 kHz. When glycerin saturated (Figure 4.15b) that magnitudes of attenuation measurements are almost identical to those in the water saturated case.

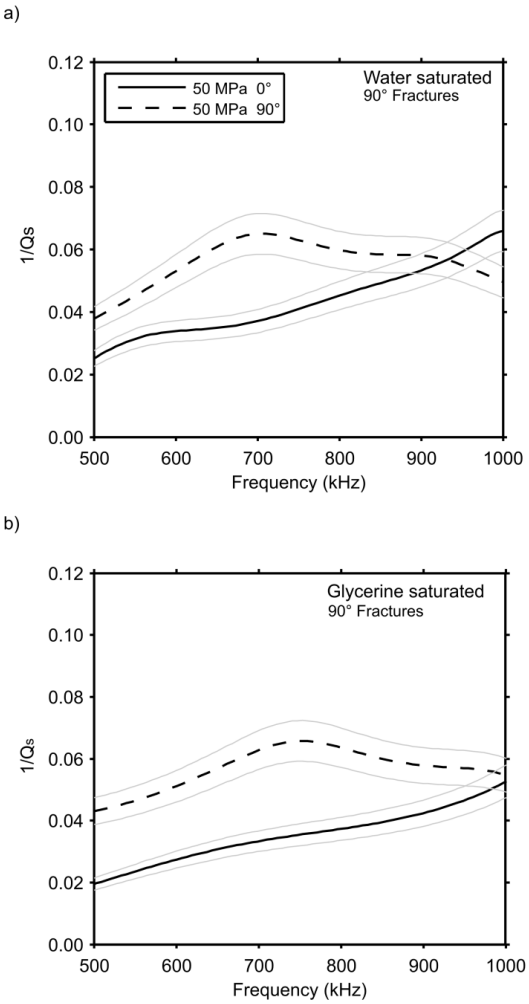

Figure 4.15: S-wave attenuations (1/Q) versus measurement frequency in the 90˚ sample when saturated with (a) water and (b) glycerin. S-wave polarisations relative to fracture direction indicated in legend.

4.14.5 Effects of scattering.

Equivalent medium fracture theories such as Chapman (2003) are based on the assumption that the fractures are much smaller than the wavelength of the sound propagating through the fractured rock (Hudson *et al.* 2001). This limit is satisfied when the wavelength of the sound is at least 4 times that of the fracture size and preferably around 10 times.

The ultrasonic pulse-echo system was used to measure P- and S-wave velocity in the 500 – 1000 kHz range. From this the wavelength, $\lambda_{P,S}$ is calculated using,

$$\lambda_{\mathrm{P,S}} = \frac{\mathrm{V_{P,S}}}{f}, \tag{4.12}$$

Wavelength to fracture size ratio is therefore calculated using:

$$ratio = \frac{\lambda_{\mathrm{P,S}}}{a}, \tag{4.13}$$

The P-wave velocity to fracture size ratio for both the 90° (Figure 4.16a) and 45° (Figure 4.16b) are about 2.5 at 500 kHz and reduce to about 1.25 at 1000 kHz. The S-wave velocity to fracture size ratio results show ratios of between 1.5 and 0.75 in the same frequency range. The ratios remain the same for the S1 & S2-waves in both the 90° (Figure 4.17a) and 45° (Figure 4.17b) samples. These ratios put the P- & S-wave velocity results into the Mie scattering regime (Mavko *et al.* 1998).

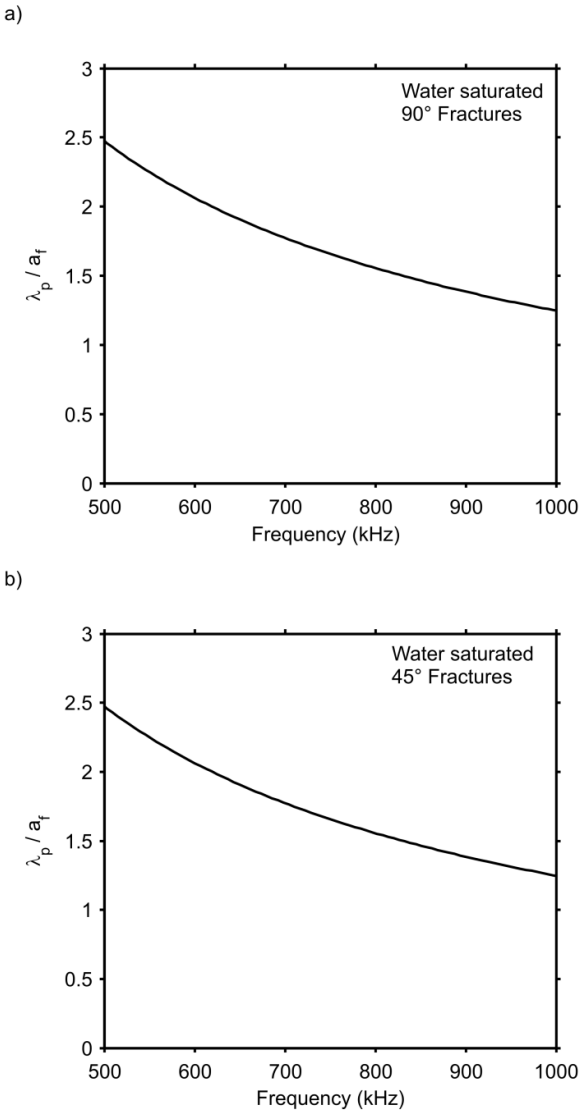

Figure 4.16: P-wave wavelength to fracture size ratio verses measurement frequency for water saturated measurements in the sample with (a) 90˚ fractures and (b) 45˚ fractures to the fracture normal, respectively.

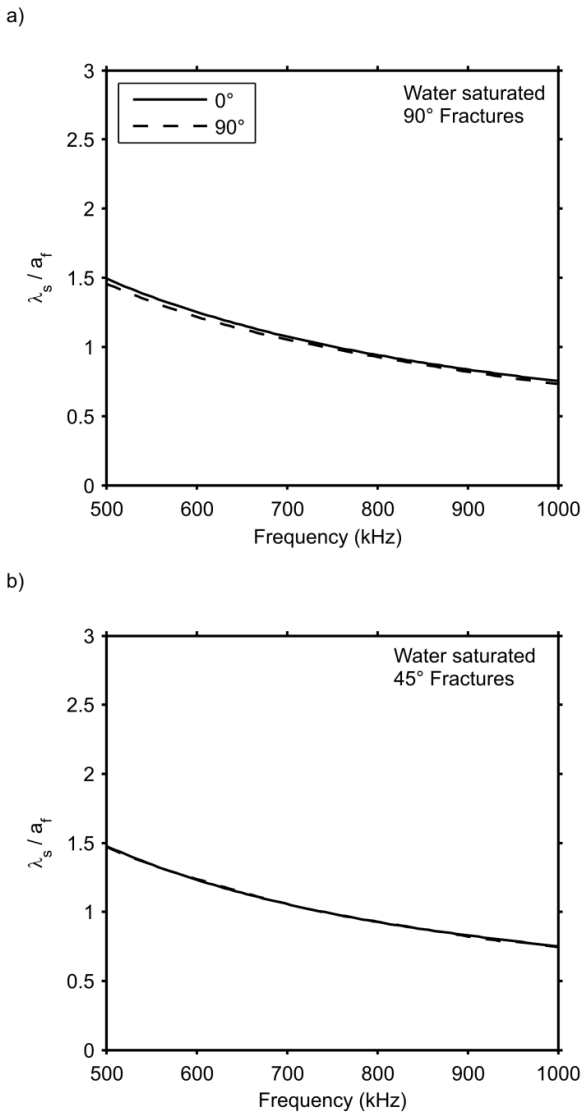

Figure 4.17: S-wave wavelength to fracture size ratio verses measurement frequency for water saturated measurements in the sample with (a) 90˚ fractures and (b) 45˚ fractures to the fracture normal, respectively. S-wave polarizations relative to fracture direction indicated in legend.

4.15 Comparison with theory.

Following the description of the Chapman (2003) theory in Chapter 3, I now apply the theory to suitable laboratory data collected from the CNPC rocks. Despite the wavelength criteria for equivalent medium theory being violated there are still a number of strong correlations.

4.15.1 Chapman (2003) model parameterisation.

Table 4.2 shows the model parameters used to implement the theory of Chapman (2003). The only free variable that requires fitting to the data is the microcrack relaxation time τ_m; the fracture relaxation time τ_f is derived from this value through model relationships incorporating the known fracture radius a_f and grain size ς (equation 3.6). Chapman *et al.* (2003) showed that setting the microcrack density ε_c to zero is a good approximation for most situations of interest, hence only the fracture density ε_f is needed in Table 4.2.

The value of τ_m was sought that minimised the misfit between the observations and model for the water saturated 45˚ and 90˚ samples. The misfit was calculated from the combined relative error between the measured and modelled velocities at 750 kHz in the 45˚ and 90˚ samples for P- (compressional), S1- (shear-wave parallel to the fractures) and S2- (shear-wave perpendicular to the fractures) waves. This approach produced the best overall fitting model without biasing it towards any single velocity mode.

The model was found to be insensitive to fracture aspect ratio (thickness/diameter), r, in the range $r < 0.01$. This insensitivity comes through the calculation of K_c (a parameter in equation 3.7). Values of small aspect ratio result in $K_c \ll 1$ meaning the resulting elastic parameters will be insensitive to r assuming it is small enough. For these experiments, an aspect ratio of 0.1 was measured using the X-ray CT scan data at room pressure. However, under pressure, the aspect

ratio will be smaller and therefore it is assumed that low aspect ratio limit remains valid.

Rock and fluid parameters used in this study	
P-wave velocity, V_P	4475 ± 13 m/s
S-wave velocity, V_S	2710 ± 8 m/s
Observation frequency, f_0	750 kHz
Bulk density of water saturated rock, ρ	2829 kgm^{-3}
Rock porosity, Φ_p	29%
Pore fluid bulk modulus (water), $\kappa_{f\ water}$	2.19 GPa
Penny-shaped fractures (at 50 MPa)	
Fracture density, ε_f	0.0201 ± 0.0068
Fracture radius, a_f	1.8 ± 0.19 mm
Fracture aspect ratio, r	0.01

Table 4.2: Model input parameters for the synthetic porous rock.

The combined misfit curve in Figure 4.18 was generated from reasonable values of τ_m based on the grain size; a minimum is clearly located at τ_m = 8 x 10^{-9} s. In fact, the error curve suggests that the data best suit a high-frequency model because the errors are smaller at larger values of τ_m (i.e., higher values of relaxation frequency = $1/\tau_m$) than at lower values of τ_m. In the high-frequency limit the fluid within the fractures become increasingly isolated from the surrounding pore space and leads to unrelaxed poro-visco-elastic behaviour.

The best fitting model velocities are compared to the actual measurements at 750 kHz in Figure 4.19. The model velocities match well for P-waves, but slightly overestimate the measured S1-wave values at 45˚ (and the duplicated results plotted at 135˚), and overestimate the S2-wave values at 45˚ and 135˚. Nevertheless, the model and experimental results are in reasonable agreement. The fit is acceptable,

particularly given the deviation of the model parameters from the assumptions of equivalent medium theory.

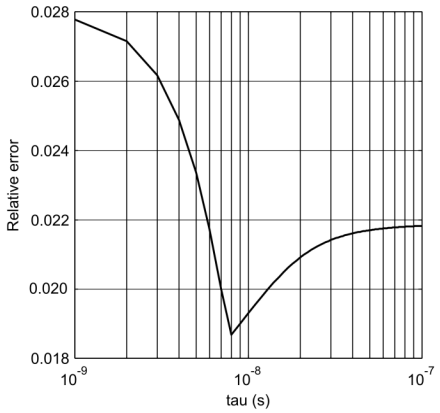

Figure 4.18: Relative error between predicted and observed ultrasonic velocities at 750 kHz in the water saturated 90˚ and 45˚ samples as a function of microcrack relaxation time τ_m; note minimum located at τ_m = 8 x 10^{-9} s.

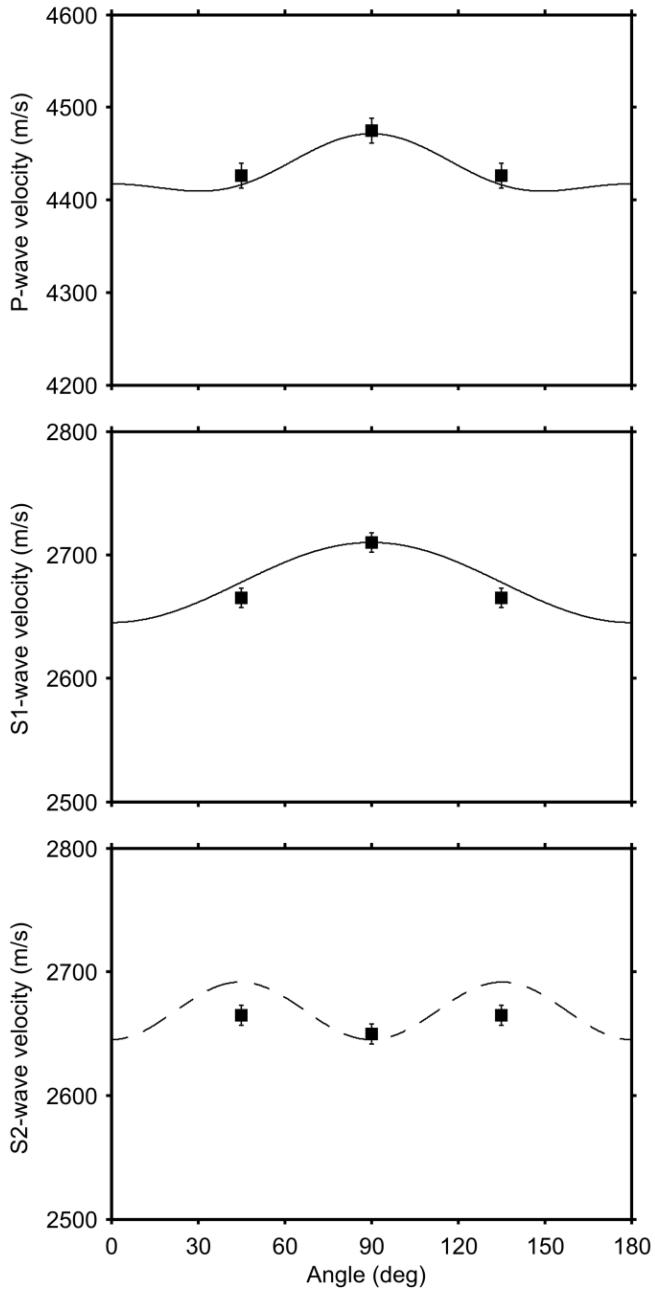

Figure 4.19: Results of best fitting model (lines) to the laboratory data for water saturated 45˚and 90˚ samples at 750 kHz (squares). Note the data at 45˚ are repeated at 135˚ on the assumption of perfect symmetry in order to complete the characteristic angular dependence curves.

4.15.2 Modelling of fluid-dependent shear-wave splitting.

An interesting feature of the theoretical model is the prediction of viscosity-dependent shear-wave splitting as a function of wave propagation incidence angle relative to the fracture normal. For this reason, the experiments were designed to discover whether any such dependencies could be observed in the synthetic rocks.

The measurements were repated under glycerin saturation. There appears to be a frame stiffening effect which results in higher P- & S-wave velocities than predicted by theory, but it is nevertheless instructive to compare shear-wave splitting results to the water saturated case.

Experimental observations of shear-wave splitting from Figures 4.13 and 4.14 are again shown in Figure 4.20, only this time plotted against pore fluid viscosity at a single frequency of 750 kHz. Again it is seen that, while shear-wave splitting is similar for water and glycerin in the 90˚ sample, shear-wave splitting is zero for water and negative for glycerin in the 45˚ sample. Note that the experimental errors are smaller than the symbols used for the data points.

Theory predicts that for wave propagation at 90˚ to the fracture normal shear-wave splitting should be unaffected by viscosity and the relationship between fracture density and shear-wave splitting holds true regardless of viscosity. At 45˚ to the fracture normal, shear-wave splitting theoretically becomes negative due to increasing viscosity since the quasi-shear (S2) velocity can be higher than that of the pure-shear (S1) at this propagation angle. It is also interesting to note that although the free parameter τ_m was fitted to the water saturated data only, it also shows good agreement with the observed shear-wave splitting as a function of fracture orientation and viscosity (i.e., in the glycerin saturated samples). This provides an independent check of the correct calibration of the model to the data.

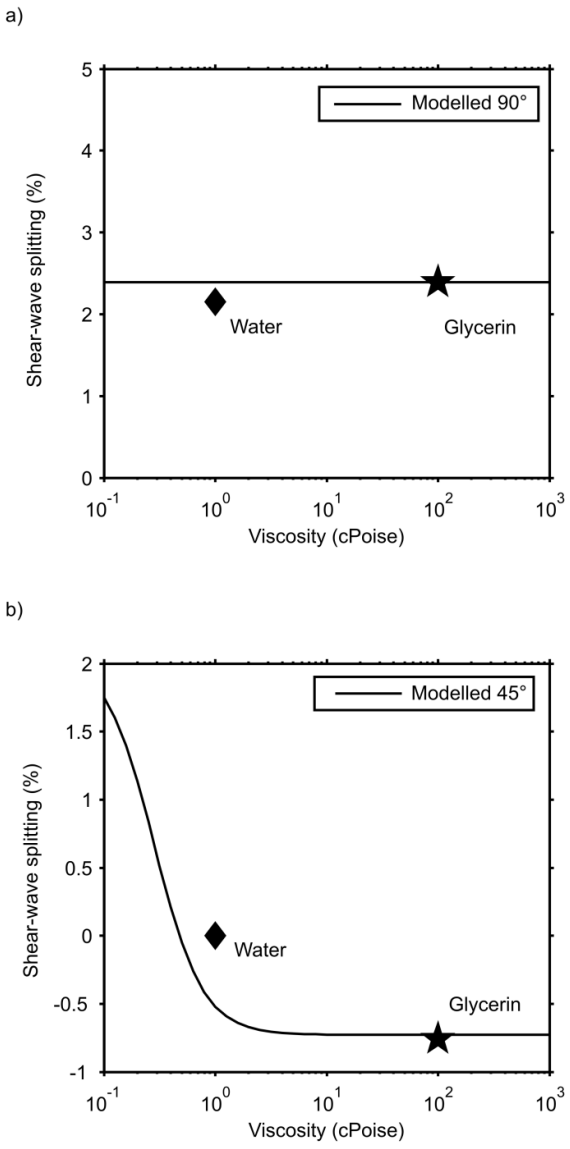

Figure 4.20: Comparison of model predictions of shear-wave splitting with observations at 750 kHz as a function of pore fluid viscosity (a) 90˚ sample and (b) 45˚ sample.

The findings here are in accordance with the theoretical predictions and field data analysis made by Qian *et al.* (2007). They successfully analyzed 3D/3-C data from the Shengli oil field, detecting attenuation and velocity anomalies of PS converted-waves. These were found to be consistent with synthetic modelling results of changes in viscosity and they observed both the oil saturated zones and the water bearing zones after water injection at the location of the oil well using the field seismic data.

4.16 Conclusions.

Laboratory observations of shear-wave splitting in synthetic rocks with penny-shaped fractures show significant changes with respect to fracture orientation and fluid viscosity relative to experimental errors. X-ray CT scanning of the rock samples allowed fracture size and density to be quantified for input to the theoretical model of Chapman (2003). Despite the experimental wavelength being close to the fracture size, the average measured magnitude of shear-wave splitting within our frequency range for waves propagating at 90° to the fracture normal is 2.15 ± 0.02% when water saturated and 2.39 ± 0.02% when glycerine saturated. This percent shear-wave splitting in the vertical core is 100 times the fracture density measured by CT scanning, as predicted by theory (Hudson 1981). The theoretical predictions of the Chapman (2003) model, relating the magnitude and polarity of shear-wave splitting to fracture orientation and pore fluid viscosity, show reasonable agreement with the laboratory observations.

The results of this study provide evidence of fluid-dependent shear-wave splitting in fractured rocks as predicted by theory. This gives added confidence in the use of the theory for the analysis of mode converted seismic wave reflection data for discrimination between, for example, oil and water in fractured reservoirs due to fluid viscosity differences.

Chapter 5

Ultrasonic Experiments II (NOCS rocks: methodology and pulse-echo).

This chapter forms an expanded version of the submitted paper:

Tillotson P., Sothcott J., Best A. I., Chapman M. and Li X. Y. Experimental verification of the fracture density and shear-wave splitting relationship using synthetic silica cemented sandstones with a controlled fracture geometry. *Submitted to Geophysical Prospecting April 2011*.

Summary: This chapter describes laboratory work carried out at the National Oceanography, Southampton using novel synthetic porous sandstones with controlled fracture geometry. The rocks closely resemble real reservoir sandstones in terms of grain cementation, porosity and permeability. The fractures are penny shaped and their size and position can be controlled. The development of the method for manufacturing the synthetic rocks is described and ultrasonic measurements are presented for a series of core plugs. These comprise three plugs fractures orientated at 0°, 45° and 90° to the fracture normal and a single unfractured (blank) plug. The latter was used to quantify the "background" anisotropy caused by the manufacturing process. The design of the rocks allowed them to withstand full saturation and pressures up to 40 MPa over three cycles with different pore fluid (air, water and glycerin) saturations. Despite the careful

manufacturing process, the three core plugs with different fracture directions showed inconsistent velocities that were attributed to small variations in grain packing and cementation between samples. Despite this, a number of useful observations could be made from measurements on individual plugs with three different pore fluids. For example in the core with 90° fractures, shear-wave splitting was equal to 100 times the fracture density for each pore fluid; in the 45° core, shear-wave splitting was seen to vary with fluid; and in the 0° core shear-wave splitting was zero.

5.1 Introduction.

Chapter 4 showed that synthetic porous rocks with controlled fracture geometries could be used to validate aspects of theories even when equivalent medium criteria are violated. The work provided the next step in theoretical validation by measuring samples with multiple fluid viscosities, something that the work of Ass'ad *et al.* (1992) and Rathore *et al.* (1995) lacked.

The next step taken to improve the model validation was to place the controlled fracture geometry within a realistic rock framework but keep the same ultrasonic measurement system. Hence, this chapter describes the development of realistic synthetic reservoir sandstones (i.e., with realistic mineralogy, grain size and shape, cementation, porosity and permeability) with a controlled distribution of penny-shaped voids (i.e., to mimic cracks or fractures in natural rocks). These novel synthetic sandstones were used to conduct controlled studies of variations in elastic wave anisotropy with fracture size and density, pore fluid type, and effective pressure along similar lines to those described in Chapter 4.

5.2 Creating synthetic rock samples with penny shaped fractures.

The simplest and most versatile way to create penny shaped fractures within a rock was to use an approach similar to Rathore *et al.* (1995). They emplaced aluminium discs while building the rock in layers of sand grains mixed with epoxy resin. Once the epoxy had set, then acid was flushed through the rock to chemically leach out the aluminium discs and thus leave behind penny-shaped voids (at least approximately penny shaped due to the geometry of the surrounding, epoxy-cemented sand grains in contact with the aluminium discs). Previous experiments (see Ellis 2008) have found that cementing sand grains with epoxy resin produced an unsatisfactory sandstone analogue because, unless cemented under an applied pressure, the sandstone is highly

attenuating and is a poor transmitter of shear waves in particular. Even if a load could be applied to the rock sample before the epoxy sets, the epoxy itself is not very representative of natural mineral cements. Instead, an improvement to the Rathore *et al*. technique by finding a suitable method of creating natural mineral cement, such as calcium carbonate or silica was sought. While a patented method of creating calcite cemented porous media exists, the Calcite In-situ Precipitation System or CIPS (see Sherlock and Siggins 2004), calcite cement would be unsuitable in this case because acid leaching of the aluminium discs would also remove the calcite cement. Instead, we chose a silica cementation method to bond the sand grains because silica is not attacked by acid.

An appropriate method for cementing sand grains is using a silica-compound (sodium silicate), widely used for over one hundred years in the metal casting industry to make sand moulds. Aqueous sodium silicate is mixed with sand to give sand moulds with a degree of strength for foundry casting (Helmut *et al.* 1969). Early trials of the methods showed the proportions of aqueous sodium silicate and sand used for moulds in the metal casting industry produced synthetic rock that was mechanically too weak for high pressure ultrasonic experiments. In the metal casting industry, the mixture was designed so that the sand could be reclaimed for the next mould.

It is possible to increase the strength of the sand bonds by adding acidic chemical setting agents, such as mineral acids and carbon dioxide gas, to the sodium silicate (Sheppard 1986). However, we found that another chemical setting agent, Kaolinitic clays, worked best for our requirements. At elevated temperatures the clays break down into acidic compounds and react with the sodium silicate to create a stronger chemical bond (Helmut *et al.* 1969). In this method the optimum proportions for the mixture of aqueous sodium silicate, kaolinite and sand were found through empirical testing. The result was,

$$Total\ mass\ of\ solids = X_{sand} + 0.25X_{sand}\ (sodium\ silicate) + 0.1X_{sand}\ (kaolinite)\ , \quad (5.1)$$

where, X_{sand} is the mass of sand grains. That is, the optimum mixture comprises X_{sand} plus sodium silicate equal to a mass of 0.25 X_{sand}, and kaolinite equal to a mass of 0.1 X_{sand}. These proportions differ greatly from those used in the metal casting industry (typically around 0.04 X_{sand} mass of sodium silicate and 0.028 X_{sand} mass of chemical setting agent) but were found to produce water proof synthetic rocks of sufficient strength to give repeatable ultrasonic velocity and attenuation measurements at high pressures (up to 60 MPa effective confining pressure).

A batch of rocks was prepared using the same material mix based on equation 5.1; a blank sample and three others containing controlled fracture geometries with fractures orientated at 0°, 45° and 90° to the fracture normal, respectively. Moulds were designed so that a cylindrical rock core could be cut that would be suitable for the ultrasonic pulse-echo measuring system (i.e., 50 mm diameter, 20-30 mm length).

To reduce ultrasonic scattering as much as possible (a constant problem with such measurements), a small fracture diameter of 2 mm was chosen. Scattering problems due to relatively large fracture size compared to the ultrasonic wavelength were noted by Hudson *et al*. (2001) for the Rathore *et al*. (1995) study, and by Tillotson *et al*. (2011). Since the fracture density is proportional to the cube of the fracture radius according to ε_f = Na^3, reducing the diameter of the fractures increases the number of fractures required to reach the desired fracture density. As the rocks were assembled manually, it was important to keep the number of fractures to a reasonable limit and the aluminium disc size to something that could be handled. For this reason a disc diameter of 2 mm and a fracture density of ε_f = 0.01 was chosen. According to elastic wave theory, fracture densities up to ε_f = 0.1 should give shear-wave splitting (expressed as a percentage) equal to 100ε_f

(Hudson 1981). Therefore, using the planned fracture density, shear-wave splitting should be around 1% and easily measureable using the ultrasonic pulse-echo system which has a velocity measurement accuracy of ± 0.3%.

To create the fractured rock, 2 mm diameter aluminium discs were stamped out of 0.2 mm thick aluminium sheet. A predefined number of discs (8 per cm^2) were arranged on top of each 4 mm layer of sand mixture in the mould (Figure 5.1). The discs were firstly scattered randomly over the surface and then flattened and spread out as best as possible. The practical difficulty of arranging such a large number of discs per layer meant that some disc overlap was unavoidable.

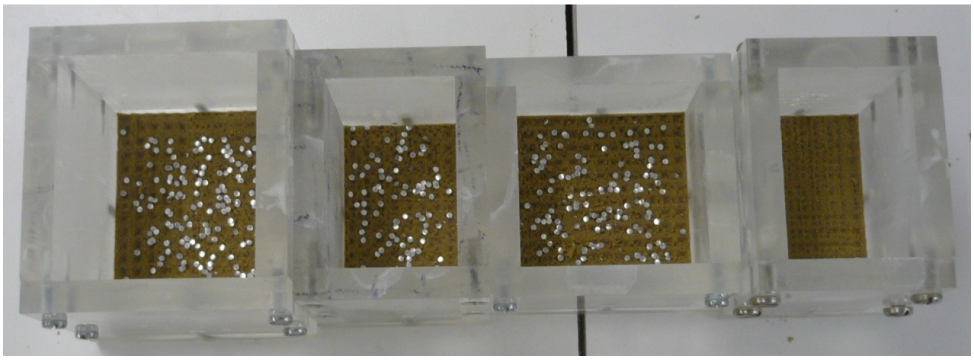

Figure 5.1: Moulds filled with a single layer of material showing the intended penny shaped fracture locations.

Once the samples had been prepared in their moulds (Figure 5.2) they were left to dry and then heated in a furnace to solidify the cement. The resultant cubic rock moulds (Figure 5.3) were then cored using a diamond drill bit to produce the 50 mm diameter core plugs (Figure 5.4).

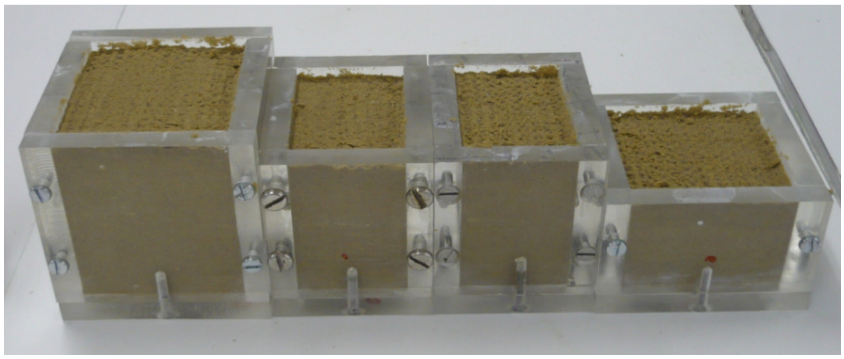

Figure 5.2: Moulds filled with 4 mm layers of mixed material with penny shaped aluminium discs.

Figure 5.3: Blocks after drying and heating in furnace.

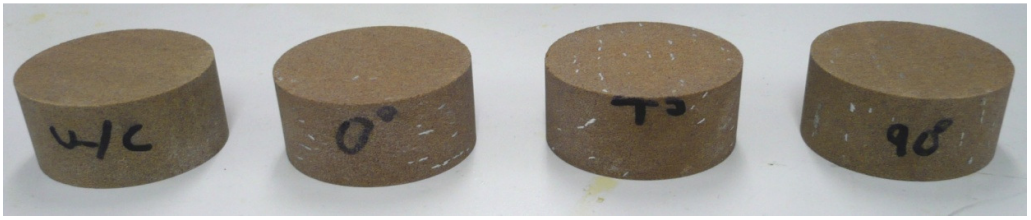

Figure 5.4: Cored samples from Figure 5.3.

The final stage of the process was to leach the aluminium discs from the "fractured" cores. This was achieved by saturating both the blank and fractured core samples with acid (so the blank sample underwent exactly the same process as the fractured sample). As in Rathore *et al*. (1995), the acid leaching process liberated gas until all the

aluminium was leached from the rock. X-ray CT scans revealed that all the aluminium had been leached out. The core samples, after leaching, are shown in Figure 5.5.

Figure 5.5: Acid leached, blank, synthetic silica-cemented sandstone sample (far left) and corresponding synthetic samples with aligned penny-shaped voids (90º, 45º and 0º respectively from left to right). The samples were cored along the grain layering which is in the same plane as the penny-shaped voids. Sample diameters are 50 mm.

5.3 Petrophysics of synthetic rock samples.

The core plugs were analysed using helium porosimetry for porosity and grain density, nitrogen permeametry for Klinkenberg corrected permeability, X-ray diffraction for mineral composition and SEM imaging for an estimate of grain size and sorting. Only the vertically fractured core was X-ray CT scanned to obtain fracture size, density and distribution due to time constraints and availability of CT scanning machine. The resulting measured properties are listed in Table 5.1.

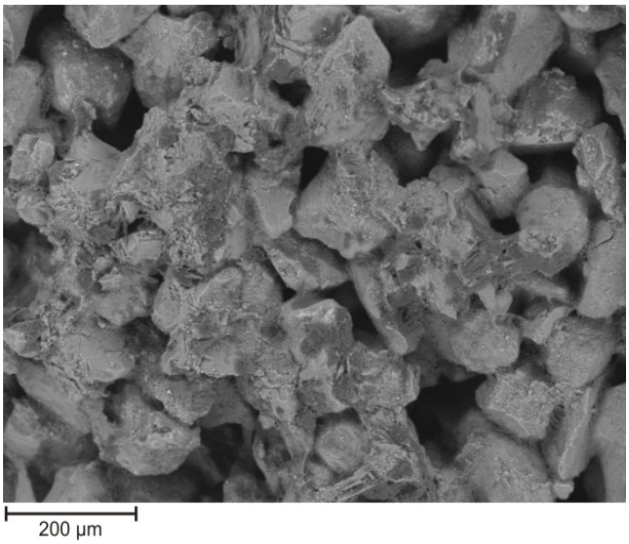

Figure 5.6: SEM image of the synthetic silica-cemented sandstone (blank sample). It shows the well sorted quartz grain size (mean 120 µm) and the distribution of the silica cement at grain contacts.

Unfractured sample	
Porosity, Φ_p	29.2 ± 0.06%
Grain density, ρ	2590 kg/m^3
Permeability, κ	40.7 mDarcy
Grain size	120 µm
Mineralogy	> 90% Silica cement
90° Fractured sample	
Porosity, Φ_p	
Grain density, ρ	30.2 ± 0.06%
Permeability, κ	2590 kg/m^3
Fracture density, ε_f	18.1 mDarcy
Average fracture radius, a	0.0298 ± 0.0077
Average fracture aspect ratio	1.19 ± 0.15 mm
	0.088 ± 0.001

Table 5.1: Physical properties of the synthetic porous rock.

The SEM image (Figure 5.6) shows well sorted sand grains (mean diameter 120 μm) and a relatively even distribution of cement between the grains. XRD analysis showed that the composition of the whole rock was >90% Silica (SiO_2). The porosity was ≈ 30% for every sample (see Table 5.1). Permeability was found to be 40.7 mDarcy in the blank sample and between 0.8 – 18.1 mDarcy for the fractured cores (see Figure 5.7). Grain density was found to be ≈ 2590 kg/m^3 for all samples. These properties are comparable with natural high porosity sandstones (King 1966, Han *et al.* 1986, Best and McCann 1995).

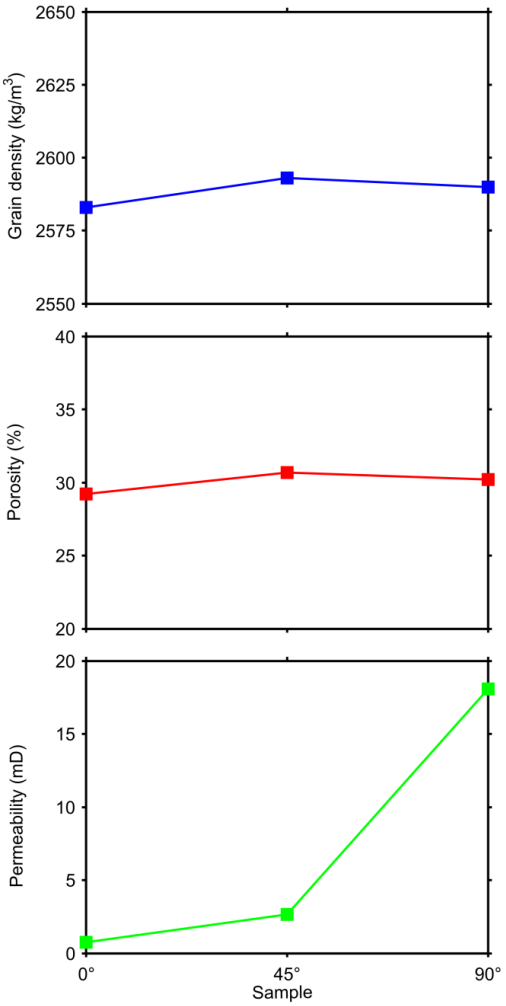

Figure 5.7: Grain density, Porosity and Permeability of the three fractured cores

X-ray CT scans of the vertically fractured sample (Figures 5.8 and 5.9) show that the aligned penny shaped voids reside in distinct layers within the rock and form a random distribution along each layer. Image analysis was used to calculate the actual fracture density, ε_f, of the sample according to the method in Chapter 4 and calculated using equation 2.10. ε_f was found to equal 0.0298 ± 0.0077. This value includes the larger voids that were created by overlapping aluminium discs as well as the smaller discrete penny shaped voids (Figure 5.9). The error in fracture density was calculated according to the method described in Chapter 4.

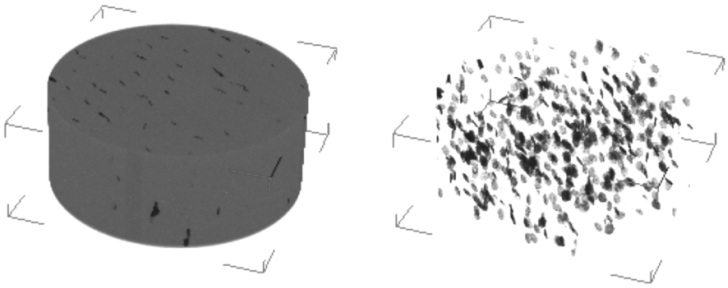

Figure 5.8: 3D X-ray CT images of the synthetic 90˚ rock sample (diameter 50 mm) showing size, density and distribution of the penny shaped fractures.

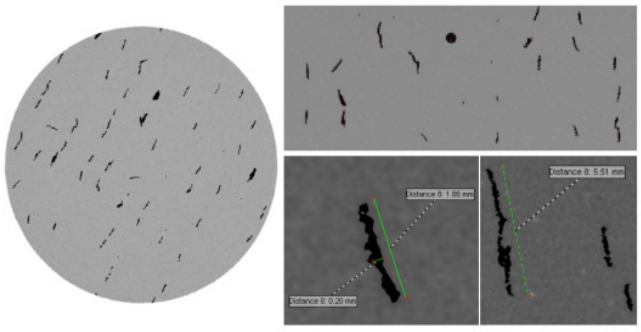

Figure 5.9: Example X-Ray CT slices used to determine penny shaped fracture sizes and density.

5.4 Unfractured rock: Hysteresis, elastic wave velocity and attenuation anisotropy.

Initial experiments were performed to determine the pressure sensitivity and layer anisotropy of the unfractured (blank) sample. The same laboratory methods and measurement techniques were used as described in Chapter 4. The blank core was water saturated and subjected to a full hysteresis cycle in 10 MPa steps from 10 – 60 MPa, and then 60 – 10 MPa differential pressure (pore pressure kept constant at 5 MPa). At each pressure P-, S1- (polarisation parallel to layering) and S2- (polarisation perpendicular to layering) wave velocity and attenuation were measured. By contrast, the three fractured samples were measured at 40 MPa only to minimise any damage that could have resulted during repeated pressure cycling.

The following results are presented at a frequency of 650 kHz (the middle of the measurement frequency range) for clarity. The results of the P-wave velocity and attenuation show some hysteresis in Figures 5.10(a) and 5.10(b), respectively, and show exponential variations with pressure typical of sandstones (e.g. Best 1992). The fact that P-wave velocity is slightly higher, and attenuation is slightly lower, on unloading indicates some degree of compaction within the sample between loading and unloading. This is unsurprising given that the samples were constructed at room pressure and could be a result of rotation and dislocation of uncemented grains leading to a stiffer framework of sand grains and a small reduction in porosity during loading. Stiffer frame moduli give higher velocity while a reduction in porosity would give lower attenuation. It is also possible that some low aspect ratio pores, such as grain contact cracks, have been permanently closed during loading, thus leading to lower attenuation on unloading (assuming a microcrack squirt flow loss mechanism; Murphy *et al.* (1986)). The measured magnitudes of P-wave velocity and attenuation are similar to those reported for high porosity sandstones in Mavko *et al.* (1998) and in Klimentos and McCann (1990).

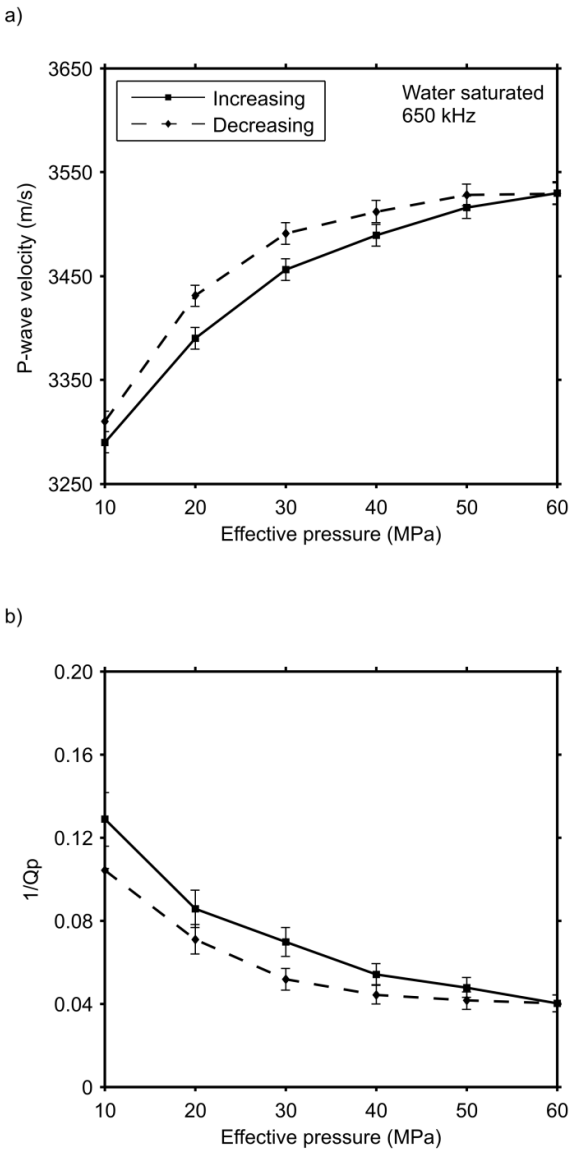

Figure 5.10: P-wave velocity (a) and attenuation (b) versus effective pressure during loading and unloading of the blank synthetic sandstone sample when water saturated. Note hysteresis.

Shear-wave splitting data were collected at a differential pressure of 40 MPa on the three fractured rock samples. This pressure was chosen to represent the high pressure regime in natural reservoir sandstones where most microcracks, such as grain contacts, are closed. However, shear-wave splitting could also be caused by the fine layering inherent in the manufacture of the synthetic sandstone samples, and this needed to be assessed first of all. Hence, shear-wave velocity (V_S) and attenuation (Q_S^{-1}) were measured parallel (S1) and perpendicular (S2) to the layering in the unfractured (blank) rock sample. Recall that the blank core was cut at 90˚ to the layer normal in a similar fashion to the vertically fractured core, which coincides with 90˚ to the fracture normal; layers and fractures are aligned in the same plane as a consequence of the synthetic sandstone manufacturing process. Shear-wave splitting (SWS) was calculated using equation 3.13. Shear-wave attenuation anisotropy (γ_Q) was calculated from (see Zhu and Tsvankin 2006),

$$\gamma_Q = \frac{Q_{S1}^{-1} - Q_{S2}^{-1}}{Q_{S1}^{-1}}, \tag{5.2}$$

Shear-wave velocities in the water saturated blank core for the S1 and S2 directions are presented in Figure 5.11(a), and associated attenuations in Figure 5.11(b), for effective pressure increasing from 10 – 60 MPa. Both S1 and S2 velocities track each other closely and increase almost linearly with increasing pressure up to 50 MPa, unlike the P-wave velocities that show an exponential increase, then reach a constant value up to 60 MPa. For attenuation, S1 is larger than S2 at 10 MPa, then becomes lower between 20 - 50 MPa, then larger again at 60 MPa; both S1 and S2 decrease with increasing pressure, consistent with the progressive closure of microcracks.

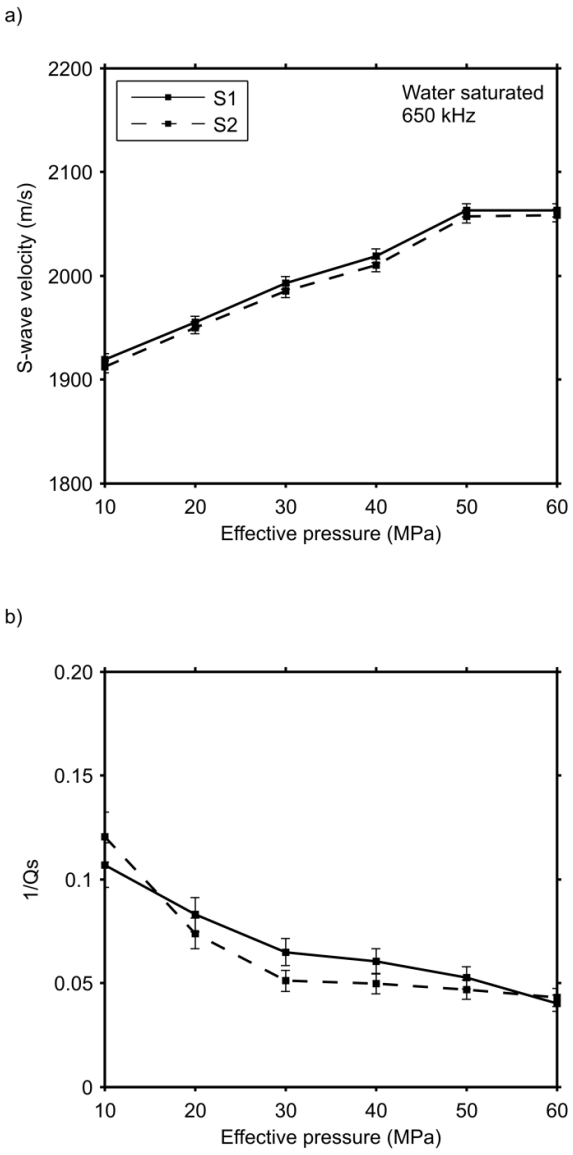

Figure 5.11: Shear-wave velocity (a) and attenuation (b), parallel (S1) and perpendicular (S2) to the layering of the water saturated blank sample, versus effective pressure for the loading half of the pressure cycle.

Figure 5.12 confirms that there is shear-wave splitting (0.25 – 0.5%) and attenuation anisotropy (< 0.3) caused by layering in the blank core. Both shear-wave splitting and attenuation anisotropy generally decreases with increasing effective pressure. Because the fractured core should have the same effect of layering as the unfractured core, then any additional anisotropy observed in it can be attributed to the penny-shaped voids (fractures).

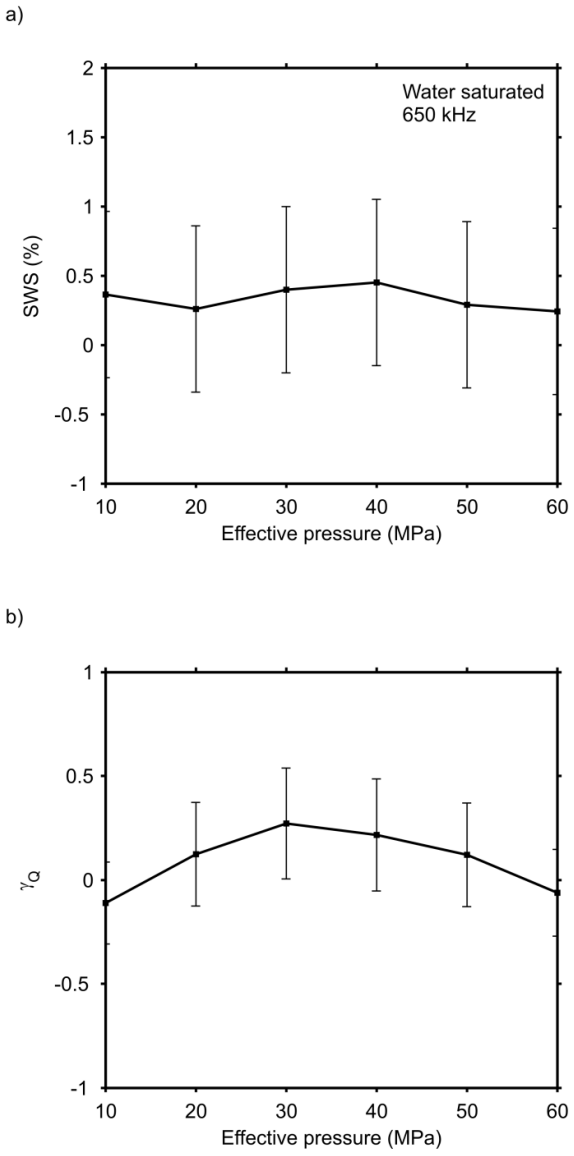

Figure 5.12: Shear-wave splitting (a) and shear-wave attenuation anisotropy (b) against effective pressure in the water saturated blank

sample showing the effect of grain layering for the loading half of the pressure cycle.

5.5 Fractured rock P-wave results.

P-wave velocity and attenuation were measured on the rock samples using the ultrasonic pulse-echo method (see Chapter 4). The broadband pulses gave useable frequencies between 400 - 1000 kHz. The actual usable frequency range is 500 – 800 kHz for this dataset. This is an optimised frequency range to minimize beam spreading and associated edge effects that appear below 500 kHz and to minimize scattering effects likely to occur above 800 kHz.

The three fractured plugs were measured while saturated with air, water and glycerin. A differential pressure of 40 MPa (confining pressure 45 MPa, pore fluid pressure 5 MPa) was used for the experiments to limit any possible damage to them (i.e., better than using 50 or 60 MPa) but still reduce the effects of grain contact microcracks as far as possible (see Figure 5.11) . P-wave velocity results are presented for the three samples with fractures orientated at 0˚, 45˚ and 90˚ to the fracture normal for air (Figure 5.13a), water (Figure 5.14a) and glycerin saturation (Figure 5.15a). Attenuation results are only presented for the cores with fractures orientated at 0˚ and 90˚ to the fracture normal for air (Figure 5.13b), water (Figure 5.14b) and glycerin saturation (Figure 5.15b) for reasons explained below. The full elastic anisotropic tensor could not be correctly calculated due to the inconsistent velocity and fracture orientation relationships that became apparent.

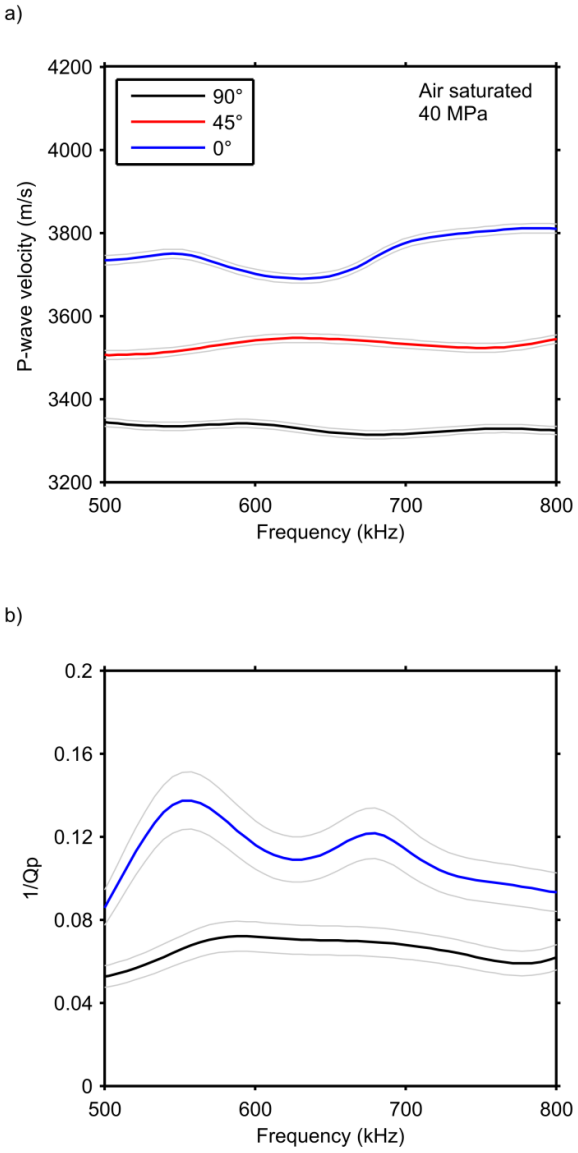

Figure 5.13: Air saturated P-wave velocity (a) and attenuation (b) relative to the fracture orientation in each core.

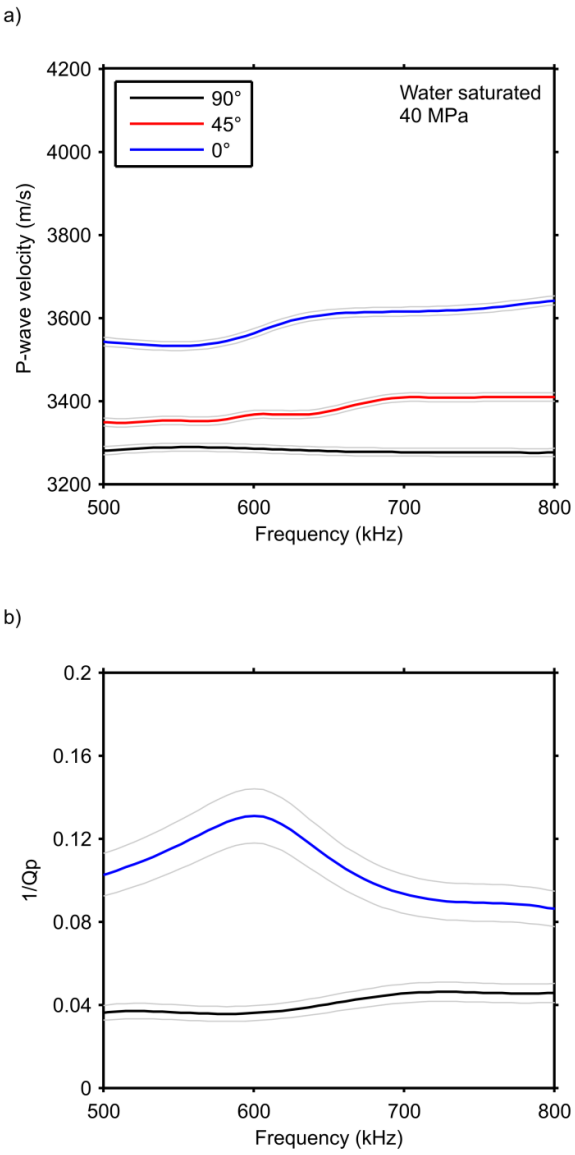

Figure 5.14: Water saturated P-wave velocity (a) and attenuation (b) relative to the fracture orientation in each core.

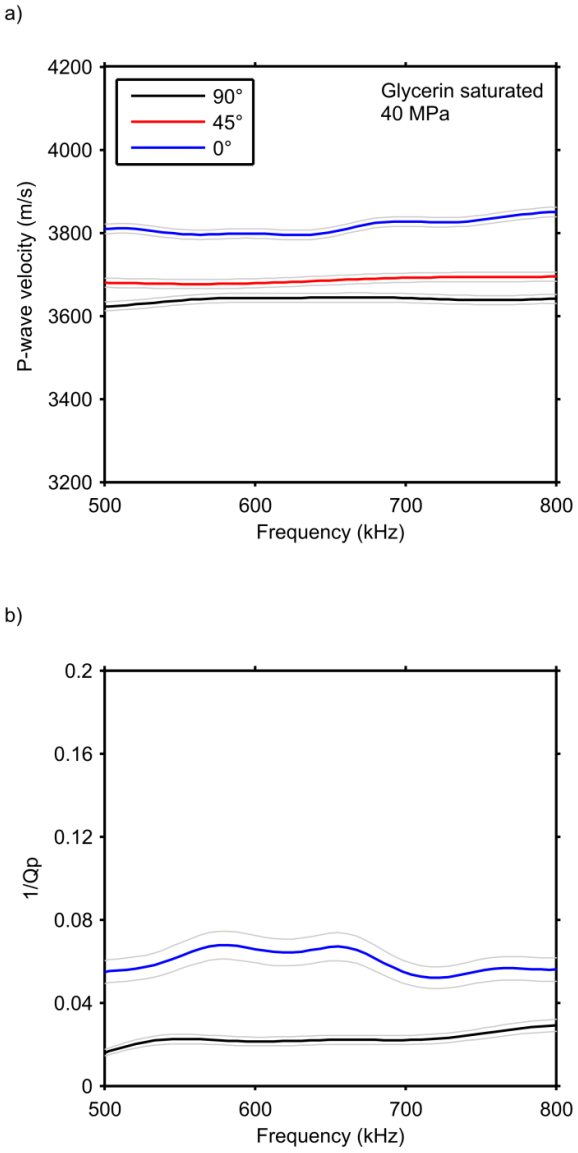

Figure 5.15: Glycerin saturated P-wave velocity (a) and attenuation (b) relative to the fracture orientation in each core.

It is seen that for all saturations P-wave velocity increases with decreasing incidence angle relative to the fracture normal direction (i.e. faster at 0˚ than at 90˚). This is at odds with theories that predict directional velocities associated with fracture orientation (e.g. Figure 3.5a). For this reason the anisotropic tensor cannot be calculated and the anisotropic reflection coefficient cannot be calculated for the 45˚ sample (see Appendix A for discussion of the anisotropic reflection coefficient). Hence, attenuation results, which require knowledge of the reflection coefficient, are incorrect for the 45º sample. Differences in fluid saturation lead to poro-visco-elastic behaviour with the 100 cPoise glycerin saturation revealing P-wave velocities that are similar to when air saturated, with both glycerin and air saturations being much faster than the water saturated case. It can be seen that the spread of velocities between the 0˚, 45˚ and 90˚ plugs is the smallest for glycerin saturation.

Attenuation results show that for each saturation the attenuation in the 0º core is higher than that in the 90º core. This finding is in line with fracture models that predict angular variations of attenuation relative to the fracture normal direction (Figure 3.5b). Attenuation also appears to reduce with increasing fluid viscosity for both fracture angles.

It is likely that scattering is a major cause of attenuation in the experiments. P-wave velocities around 3600 m/s and a central frequency of 650 kHz gives wavelengths of around 5.5 mm. The average penny shaped fracture size was 1.19 ± 0.15 mm gives a wavelength to fracture ratio of around 4.5 : 1. The situation is much worse for the slower S-waves (around 2200 m/s), with a wavelength of 3.4 mm and a wavelength to fracture ratio of 2.8 : 1 (see below).

5.6 Fractured rock S-wave results.

S-wave velocity for all three samples and attenuation for the 0° and 90° samples only (due to unknown reflection coefficients; see above) were also measured using the ultrasonic pulse-echo method. Shear-wave

splitting was measured according to the methods in Chapter 4. To ensure the S1- and S2-waves were correctly measured in the 45° sample, the polarization of the shear-wave transducer was lined up parallel with the fracture strike to measure the S1-wave, and perpendicular to the fracture strike to measure the S2-wave. This removed any ambiguity in the S-wave polarization direction. In the 0° sample, S-wave anisotropy was measured by recording S-wave signals at 90° to each other using a reference line marked on the sample to maintain the consistency of the measurements for each pore fluid.

Example raw data base reflection waveforms are presented in Figure 5.16 from the sample with 90° fractures when saturated with air (Figure 5.16a), water (Figure 5.16b) and glycerin (Figure 5.16c). The waveforms show that for each saturation distinct shear-wave splitting is observed as a result of rotating the shear-wave transducer from parallel to the strike of the fractures (S1) to perpendicular (S2).

The S-wave velocities broadly show the same velocity trends as the P-waves with regards to the velocity variations between the samples with differing fracture normal directions (i.e. faster at 0° to the fracture normal) for all saturations.

The air saturated S-wave velocities (Figure 5.17a) show that significant shear-wave splitting is measured in both the 45° and 90° samples and that no shear-wave splitting is seen in the 0° sample. This is echoed in the air saturated attenuation data (Figure 5.17b). In the 90° sample the S2-wave attenuation is markedly higher than the S1-wave attenuation. Both S-waves measured in the 0° sample show similar attenuation to the S2-wave at 90°.

The water saturated and glycerin saturated S-wave velocities show similar trends to each other (Figures 5.18a and 5.19a) with significant shear-wave splitting only being measured in the 90° sample. On the 0° and 45° samples shear-wave splitting is almost zero. Attenuation results mirror those of the air saturated measurements.

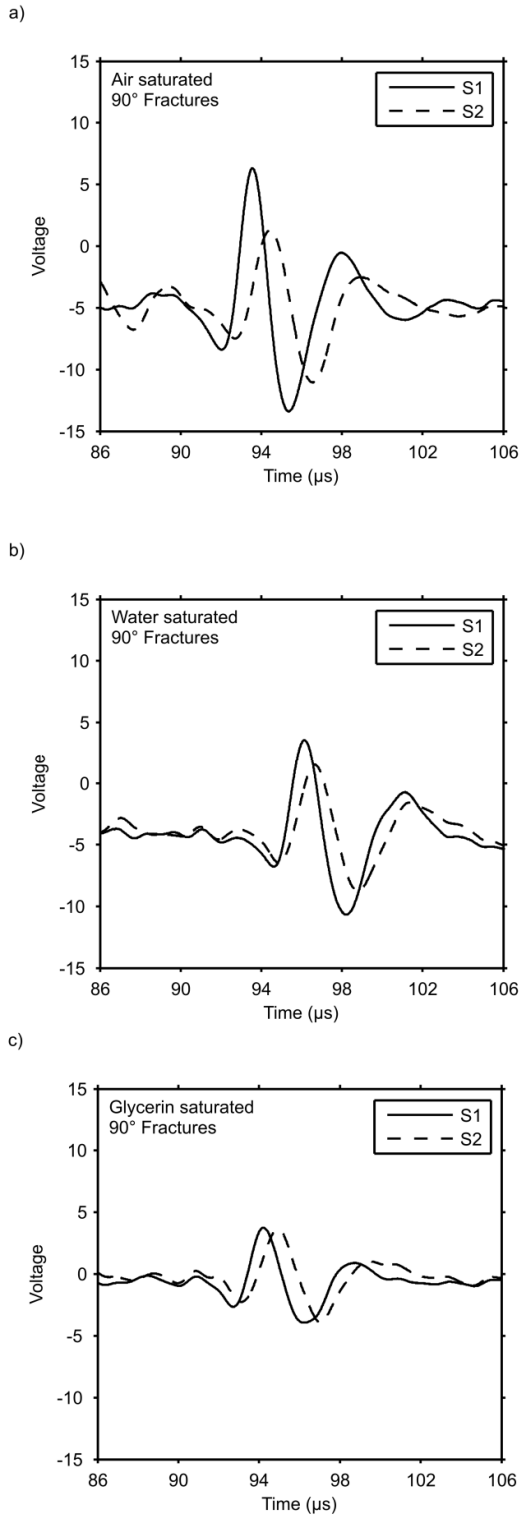

Figure 5.16: S-wave pulse reflections from the base of the 90° sample while saturated with air (a), water (b) and glycerin (c).

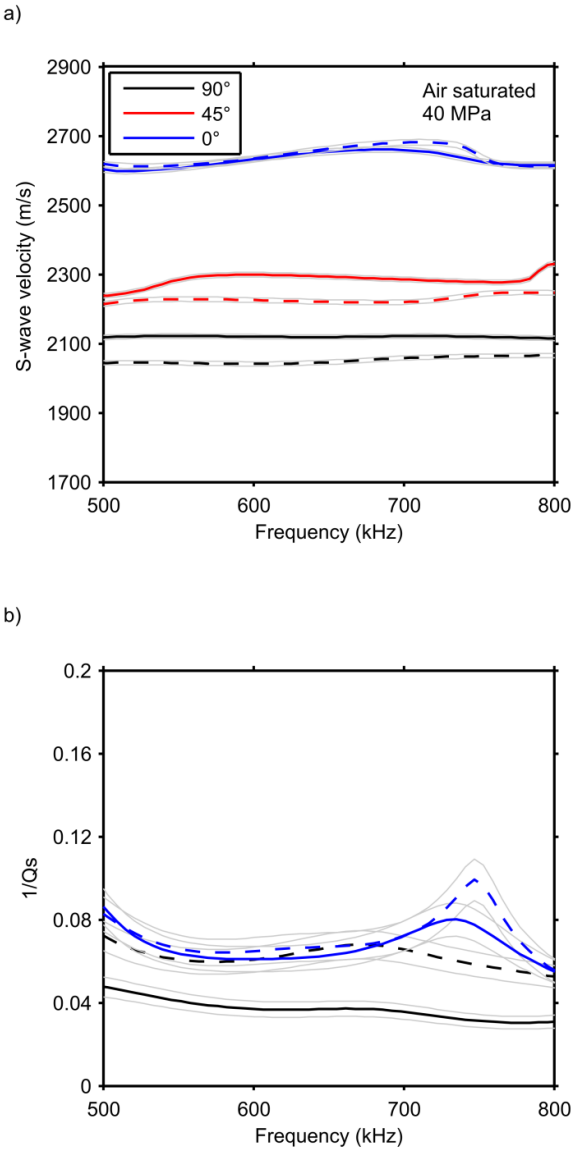

Figure 5.17: Air saturated S-wave velocity (a) and attenuation (b) relative to the fracture orientation in each sample. Solid lines indicate S1-waves and dashed lines S2-waves.

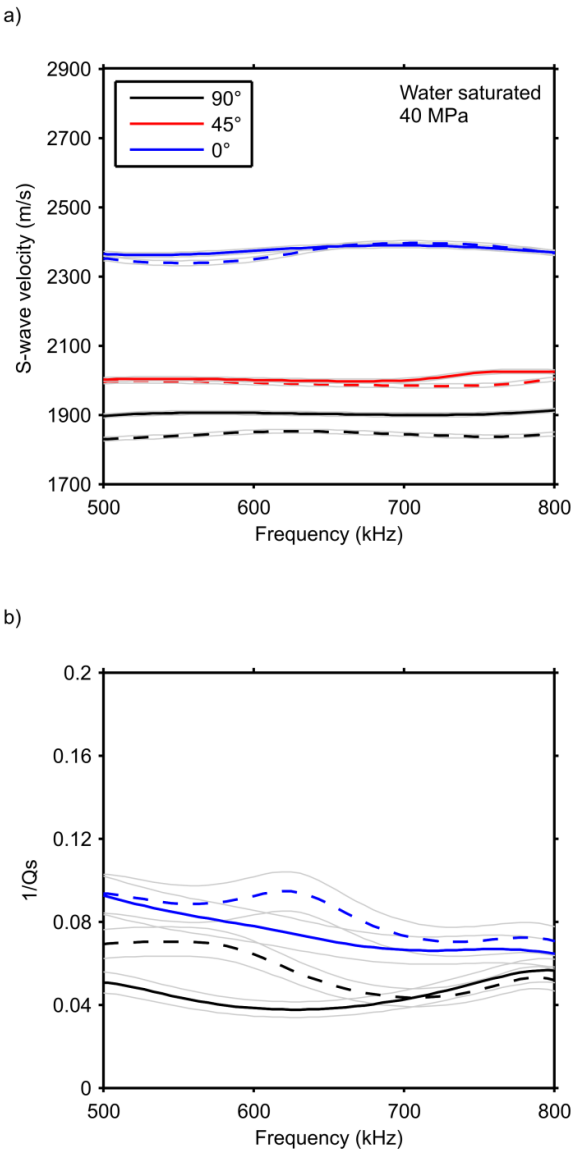

Figure 5.18: Water saturated S-wave velocity (a) and attenuation (b) relative to the fracture orientation in each sample. Solid lines indicate S1-waves and dashed lines S2-waves.

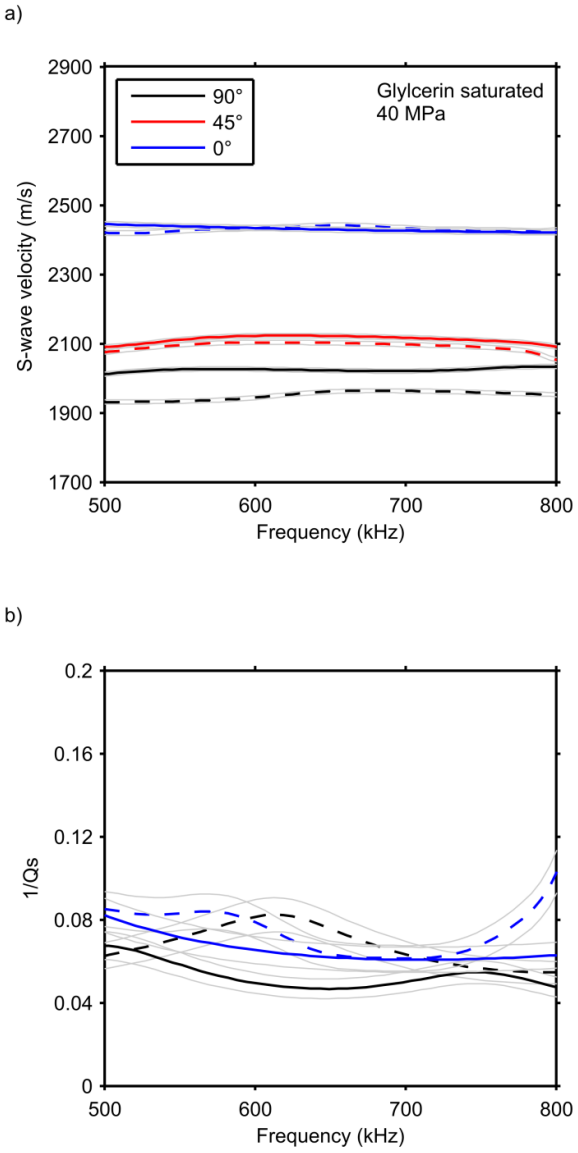

Figure 5.19: Glycerin saturated S-wave velocity (a) and attenuation (b) relative to the fracture orientation in each sample. Solid lines indicate S1-waves and dashed lines S2-waves.

5.7 Observations of fluid-dependent shear-wave splitting.

The limitations of this dataset are clear. The measurements from each core plug do not agree with established fracture anisotropy theory that predicts, for example, that P-wave velocities should be faster at 90° to the fracture normal than at 0°. For this reason, a sensible approach to the data analysis is to treat the data from each plug separately to see if there are any fluid-dependent effects that are consistent with the theory in the three fracture directions.

Theory predicts that shear-wave splitting should be zero for shear-wave propagation at 0° to the fracture normal. Figure 5.20 shows the S1 and S2-wave velocities (a) in the 0° plug for the three saturations and corresponding shear-wave splitting (b). It can be seen that the shear-wave splitting results, within error bars, match the broad theoretical prediction that for each saturation shear-wave splitting should be zero. No layering shear-wave splitting correction has been applied because an unfractured sample with layering cored at 0° to the layering normal was built. Nevertheless, with theory predicting that shear-wave splitting should be zero at this incidence angle in the layered case the fracture core results should remain valid.

A key finding from chapter 4 was this dependence on fluid viscosity at 45° to the fracture normal. Figure 5.21 reveals that shear-wave splitting does appear to be dependent on saturating fluid at 45° to the fracture normal. To what extent this relates to theoretical predictions cannot be known.

The other key finding from chapter 4 was the robust nature of the relationship between shear-wave splitting and fracture density. Analysis of the shear-wave splitting in the synthetic sandstone core with fractures orientated at 90° to the fracture normal (Figure 5.22) shows that this relationship remains true, namely that percentage shear-wave splitting is 100 times the fracture density as determined using X-ray CT scanning. It should be noted that the shear-wave splitting in the 90° fractured core is

corrected for layering anisotropy at 40 MPa from the water saturated blank sample (0.48%; Figure 5.11a).

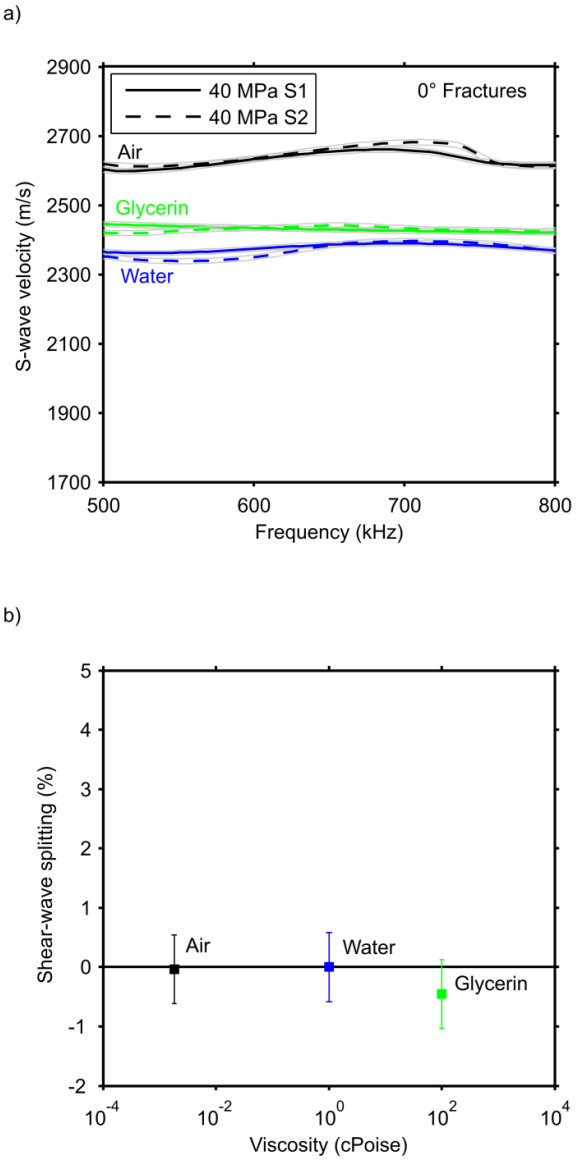

Figure 5.20: (a) Shear-wave velocities (S1 & S2) versus measurement frequency at 40 MPa effective pressure in the 0˚ sample with penny-shaped voids (i.e., wave propagation at 0˚ to fracture normal) when saturated with air, water and glycerin. (b) Shear-wave splitting versus fluid viscosity.

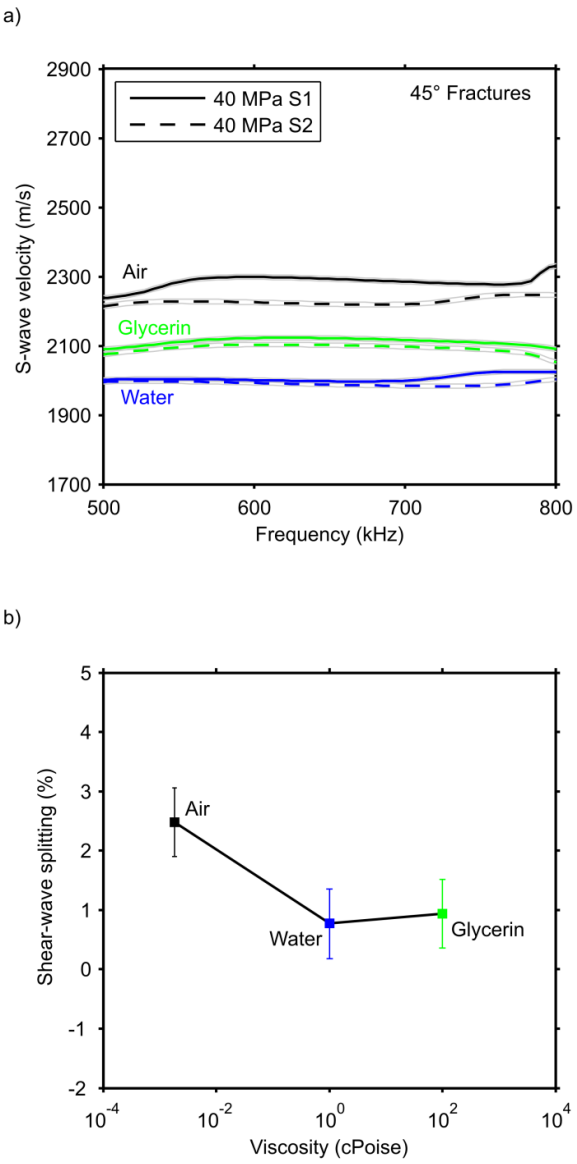

Figure 5.21: (a) Shear-wave velocities (S1 & S2) versus measurement frequency at 40 MPa effective pressure in the 45˚ sample with penny-shaped voids (i.e., wave propagation at 45˚ to fracture normal) when saturated with air, water and glycerin. (b) Shear-wave splitting versus fluid viscosity.

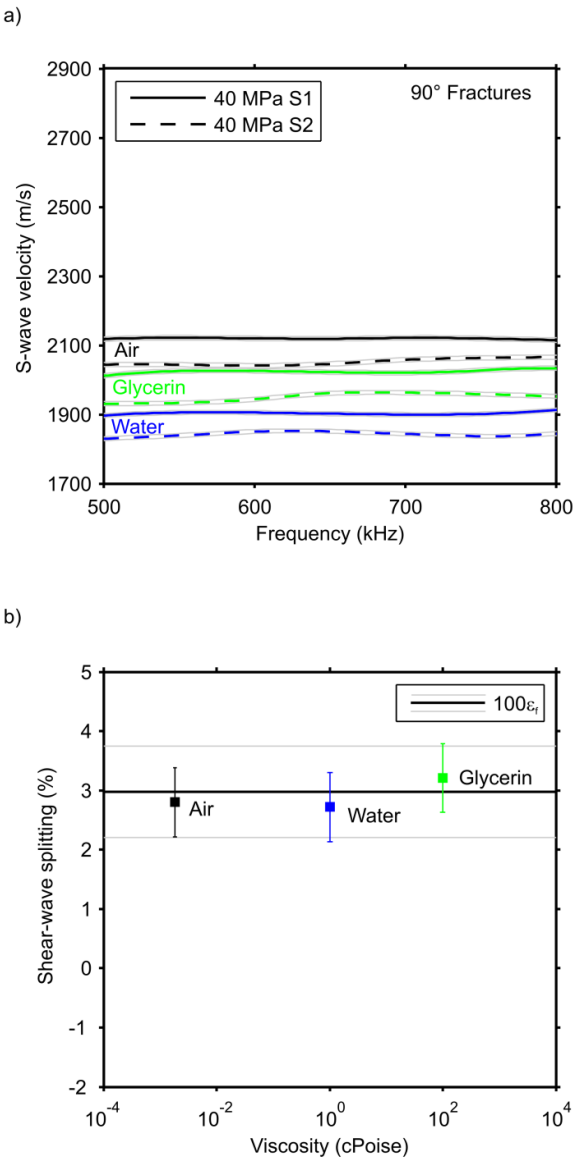

Figure 5.22: (a) Shear-wave velocities (S1 & S2) versus measurement frequency at 40 MPa effective pressure in the 90˚ sample with penny-shaped voids (i.e., wave propagation at 90˚ to fracture normal) when saturated with air, water and glycerin. (b) Shear-wave splitting versus fluid viscosity. The fracture density (ε_f) with error bars measured from X-ray CT image analysis is indicated (i.e., 100 times fracture density).

5.8 Conclusions.

Laboratory validation of seismic fracture theories requires synthetic rocks with controlled fracture properties to suit the idealised fracture shapes and distributions of various theoretical models. To date there have only been a handful of published experiments of this nature, but all suffer from results on somewhat unrealistic synthetic rocks. Hence, a method for making realistic synthetic sandstones that contain a known distribution of penny-shaped voids for further verification of theory was attempted. Methods adapted from the metal casting industry were used to prepare samples of silica cemented quartz sandstone with porosity ≈30% and permeability ≈30 mDarcy. By arranging aluminium discs during the manufacture process and subsequently removing the aluminium with acid, it was possible to make a sample with a regular distribution of penny-shape voids. The size of these voids was chosen with practical considerations in mind, but also to be much larger than the sand grain size and yet small enough to minimise ultrasonic scattering in our experiments. The manufacturing process reported here is capable of producing realistic, silica-cemented, synthetic sandstone which exhibits ultrasonic velocity and attenuation properties essentially the same as for natural sandstone samples of similar porosity, permeability and cement content.

Despite careful duplication of preparation methods for the blank sample and the three fractured samples, the measured ultrasonic velocities did not conform to accepted theoretical predictions between samples. This indicated some randomness in the synthetic sandstone manufacturing process, probably caused by different degrees of grain compaction before cementation under atmospheric pressure. An improved method for future investigation would be to cement the quartz grains while under a uniform effective pressure, although this was not possible in the timeframe of this project. Hence, it was not possible to consider the four samples as having the same rock frame properties, and so the full elastic moduli tensor due to fracture anisotropy could not be derived. Despite this, it was still possible to make meaningful

observations of shear-wave splitting on individual samples and how it varied with pore fluid.

The measured shear-wave splitting due to layering in the blank sandstone sample was less than 0.5%, while the shear wave splitting measured in the fractured sample (i.e., with penny-shaped voids and minus the blank sample layering anisotropy) was much larger, equal to 2.72 ± 0.58% for water saturation. Furthermore, shear-wave splitting did not vastly change with fluid saturants air and glycerin, and in all cases was similar to $100\varepsilon_f$, where ε_f is the fracture density due to penny-shaped voids measured from X-ray CT scans of the core sample. This result confirms theoretical predictions for porous rocks and for high porosity sandstones in particular. Hence, percentage shear-wave splitting (SWS) can be taken as a reliable indication of fracture density (i.e., SWS equal to around 100 times the fracture) in high porosity sandstones, a relationship that is independent of fluid in agreement with the conclusions of chapter 4.

To overcome the inter-sample variability seen in this chapter, it was decided to build larger sandstone blocks so that all the measurements could be obtained on a single sample. This necessarily meant abandoning the highly accurate pulse-echo system which requires 5 cm cylindrical samples and pressures greater than about 5 MPa for consistent coupling. Hence, bench top anisotropy measurements are the topic of the next chapter.

Chapter 6

Ultrasonic Experiments III (NOCS rocks: octagonal samples and bench-top experiments).

This chapter forms an expanded version of the submitted paper:

Tillotson P., Chapman M., Sothcott J., Best A. I. and Li X. Y. Analysis of P- and S-wave anisotropy in silica cemented sandstone with a controlled fracture geometry. *Submitted to Geophysical Prospecting June 2011.*

Summary: This chapter describes a third set of laboratory ultrasonic measurements. The measurements used a bench-top setup to measure P- & S-wave velocity and attenuation through octagonal shaped rocks samples. Two samples were manufactured using the methods outlined in chapter 5. One sample was left unfractured to measure the layering anisotropy associated with the manufacturing. The other sample contained a controlled fracture geometry consisting of well positioned penny shaped voids. Both samples were measured air, water and glycerin saturated by placing transducers on opposing faces of the rock. The results showed that layering anisotropy was small, but was significant enough to cause more anisotropy than expected in the fractured samples. Measurements of the fractured rock showed that P- & S-wave velocity and attenuation anisotropy was present. Maximum P-wave velocity, minimum P-wave attenuation and maximum shear-wave

splitting all occurred at 90° to the fracture normal. Poro-visco-elastic effects were also clear. For example at 45° to the fracture normal fluid-dependent shear-wave splitting was observed shown by a polarisation flip between water and glycerin saturation. By accounting for the background anisotropy in the Chapman (2003) model it was possible to model the anisotropy observed in the fractured rock for the three fluid saturations. The model was able to predict angular observations of shear-wave splitting between water and glycerin and to also predict Thomsen's anisotropy parameters, epsilon, gamma and delta for air, water and glycerin saturations.

6.1 Introduction.

A new method for creating synthetic silica cemented sandstones with a controlled fracture geometry was reported in chapter 5. The results in chapter 5 showed that although the method could produce realistic silica cemented sandstones with a controlled fracture geometry, the inter-sample variability caused velocity variations that did not agree with expected theoretical variations. This inter-sample variability was attributed to cementation variations between the separate samples. In a bid to remove this variability, larger samples, one unfractured to measure background anisotropy and a fractured sample were constructed in a bid to acquire all measurements on the single samples with respect to the fracture direction.

Given that the size of the samples that could be reasonably manufactured was found to be approximately 7 cm^3. This was not sufficiently large enough to allow three core plugs taken at different angles to the fracture normal. A decision was made to use a new bench-top laboratory arrangement taking direct transmission measurements in different directions though a single sample at atmospheric pressure.

The samples were ground into octagonal prisms that had faces wide enough (25 mm) to place 1 inch transducers on opposing faces allowing the full anisotropic tensor to be measured (see Appendix A). By using an ultrasonic broadband pulse (central frequency 500 kHz), comparison of the transmission spectrum recorded through the rock with that of a known reference material (duralumin) meant that phase velocity and attenuation could be calculated.

Velocity (P-, S1 and S2-wave) and attenuation (Q_P^{-1}, Q_{S1}^{-1} and Q_{S2}^{-1}) was measured in the two samples while saturated with air, water and glycerin for azimuths at 0°, 45°, 90° and 135° to the layer and fracture normals (0° = 180°).

The measurements found that the unfractured sample showed small levels of P- and S-wave velocity anisotropy for all saturations and as a result increased the expected anisotropy measured in the fractured sample. By incorporating the measured background anisotropy into the

Chapman (2003) model it was possible to quantify the measured anisotropy seen in the fractured rock by using comparisons of Thomsen's anisotropy parameters, epsilon, gamma and delta. In addition to this, fluid-dependent shear-wave splitting was seen at 45° to the fracture normal consistent with observations seen in chapters 4 and 5.

6.2 Creating octagonal shaped samples.

Two synthetic sandstones were built with the composition given in equation 5.1. The same mixture of material was used and layers were filled alternatively between the two moulds which were 7 x 7 x 7 cm in internal dimensions. One sample was left blank (to measure matrix anisotropy) and the other contained a controlled fracture geometry.

Transducers with a central frequency of 500 kHz were used for the experiments. For this reason larger diameter penny-shaped voids were planned and as a result the number of fractures required for the fracture density decreased. The fractured samples in chapter 5 suffered from overlap of aluminium discs at the manufacturing stage.

Penny shaped discs were punched out of 150 μm thick aluminium with a diameter of 5 mm and positioned carefully using two templates: one for odd layers (Figure 6.1) and the even numbered layers (Figure 6.2). The layers were 5 mm in thickness. This configuration was designed to minimise scattering that could occur due to coincident fractures in each layer.

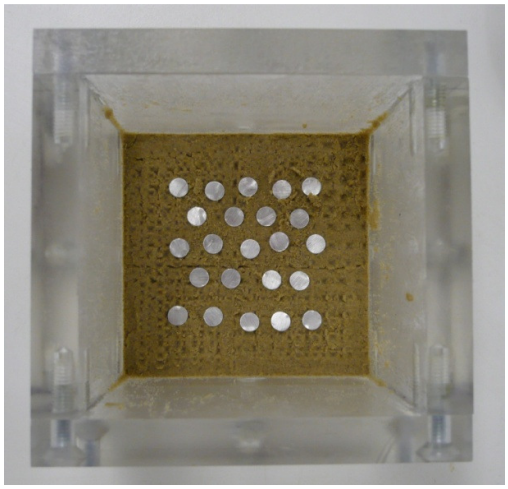

Figure 6.1: Aluminium disc arrangement in the odd numbered layers in the fractured sample.

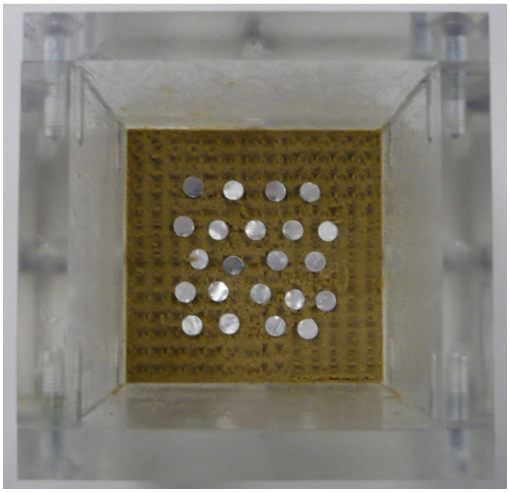

Figure 6.2: Aluminium disc arrangement in the even numbered layers in the fractured sample.

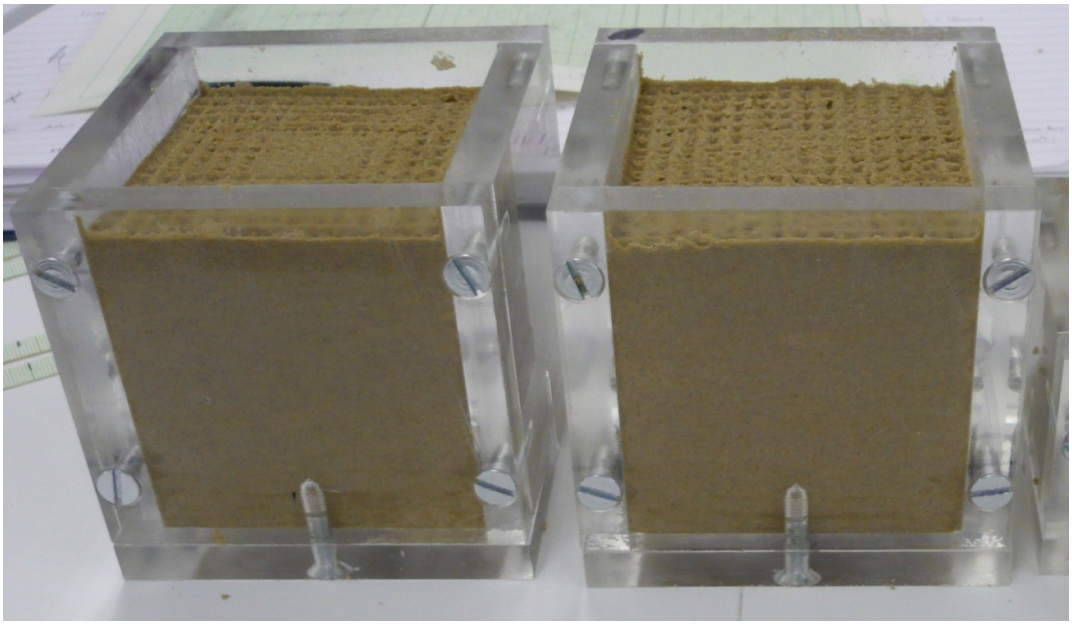

Figure 6.3: Moulds filled with 5 mm layers of mixed material. Left containing aluminium shaped discs, right blank.

Figure 6.4: Blocks after drying and heating in the furnace. Aluminium discs on the top of the left block only act as a reminder to it being the fractured block.

The samples were then built up in layers until the moulds were full (Figure 6.3) and then dried and heated as per chapter 5 (Figure 6.4). The same Jones and Shipman grinding machine used to ensure the pulse-echo core samples are ground flat was used to grind the cube samples into octagonal prisms with 25 mm wide faces (large enough to press a transducer against) at increments of 45° to the fracture normal (Figure 6.5).

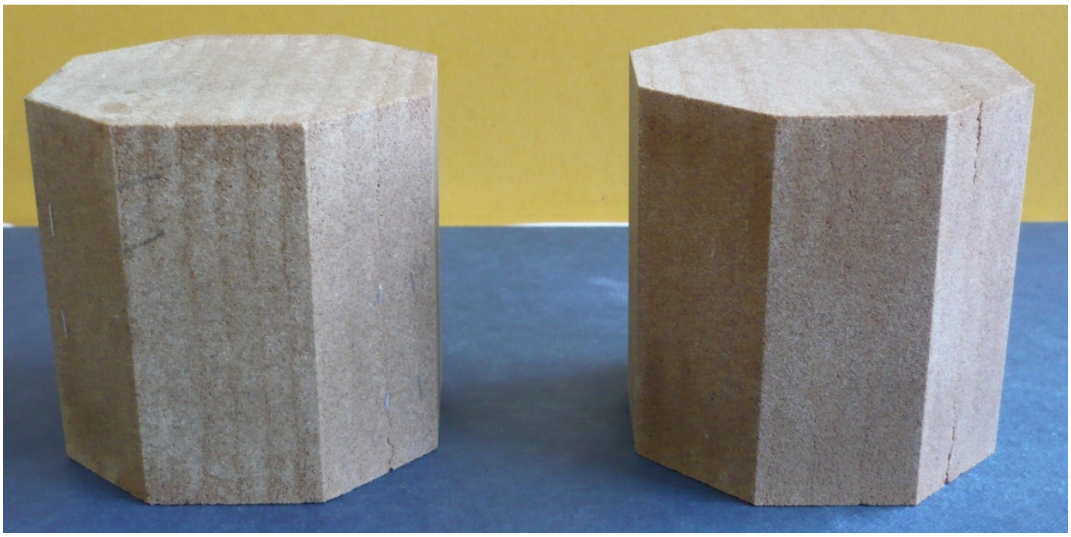

Figure 6.5: Octagonal shaped blocks, left containing aluminium discs and the right blank before acid leaching.

To create the voids the same method as chapter 5 was used. Both samples were immersed in acid to ensure they underwent the exact sample process causing leaching of the aluminium discs. Due to the larger size of the samples it took longer for the bubbling to reduce in the fractured sample. However, a low resolution fast X-ray CT scan at Southampton General Hospital was used to show that all the aluminium had been dissolved within the fractured sample meaning that both samples were ready to be measured. The final samples are shown in Figure 6.6.

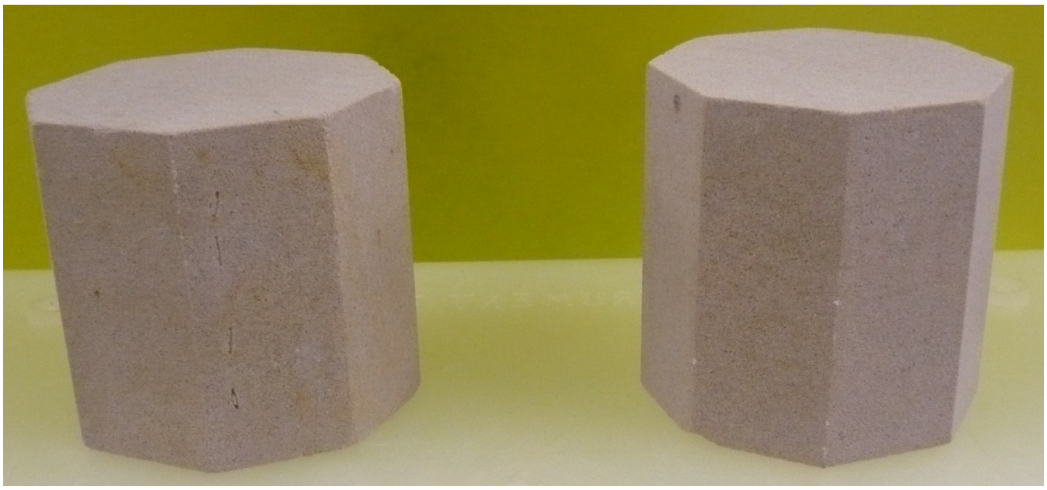

Figure 6.6: Acid leached samples containing penny shaped voids (left) and blank sample (right).

6.3 Petrophysics of octagonal synthetic rock samples.

The octagonal shaped rock samples were analysed using SEM imaging (with diagnostic probe) for grain size, sorting, cementation variation and composition, probe permeametry and X-ray CT scanning for fracture property analysis. The physical properties are listed in Table 6.1.
An example of an SEM image is shown in Figure 6.7. This figure shows that the grain size, distribution and levels of cementation compare well with the samples manufactured in chapter 5 (see Figure 5.6). The Hitachi TM-1000 SwiftED-TM analyser showed >90% silica was present in the rock; this is in line with the XRD analysis carried out in chapter 5.

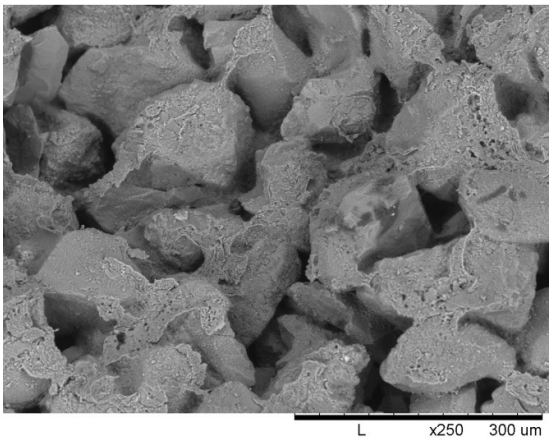

Figure 6.7: SEM image of the octagonal synthetic silica-cemented sandstone (blank sample). It shows the well sorted quartz grain size (mean 120 μm) and the distribution of the silica cement at grain contacts.

X-ray CT scanning was carried out at the μ-VIS centre based at the University of Southampton. The fractured rock was scanned and the data gave a resolution of 42 microns. The 3D data constructions were analysed in 1D slices (Figures 6.8 and 6.9) and using 3D volumes (Figure 6.10). These scans were used to determine the fracture density of the sample (and associated error) in the same manner as chapters 4 and 5. The fracture density was found to be, $\varepsilon_f = 0.0314 \pm 0.0059$.

Probe permeametry was carried out using the methods of Halvorsen and Hurst (1990). A number of flow readings were taken on each face of the octagonal rocks. These readings were correlated with rocks of known permeability also measured with the probe permeameter. Permeability was found to vary from face to face, but the average for both samples was found to be 21 mDarcy.

Density was calculated in the fractured rock by dividing the saturated weight by the volume measured in the X-ray CT scan. The volume of the unfractured sample was calculated using Archimedes principle in a water bath. The porosity of each sample was calculated

from the dry and water saturated weight differences and a density of 1000 kg/m^3 assumed for the saturating water.

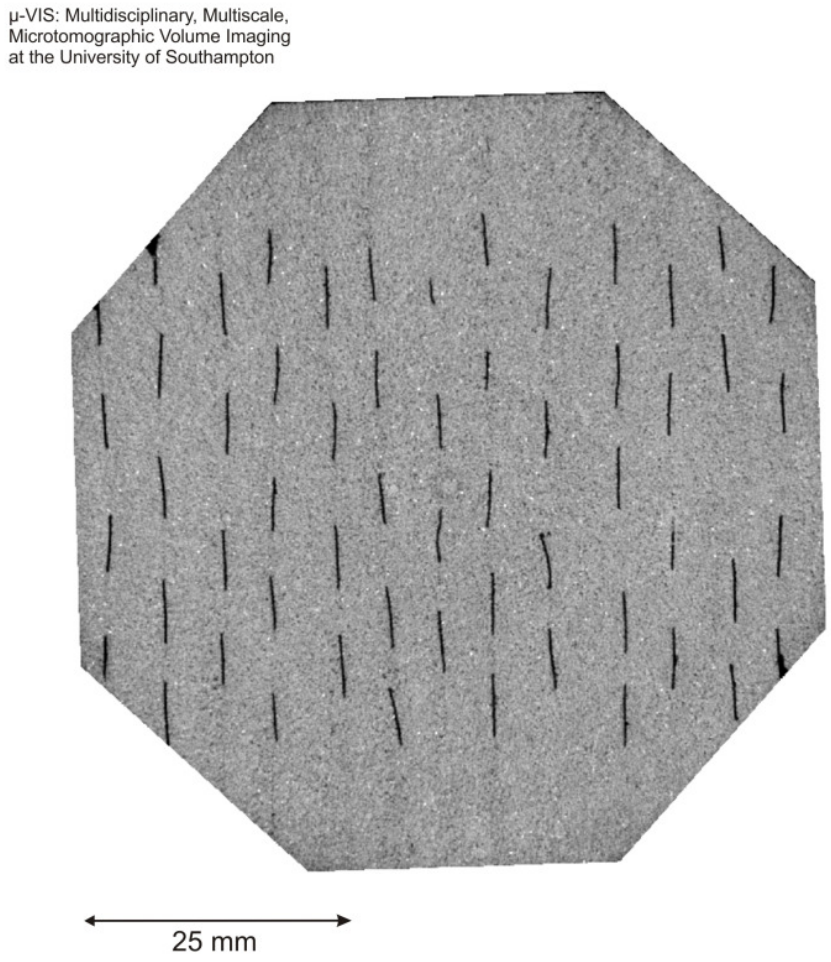

Figure 6.8: X-ray CT scan image showing a cross section through the middle of the fractured sample.

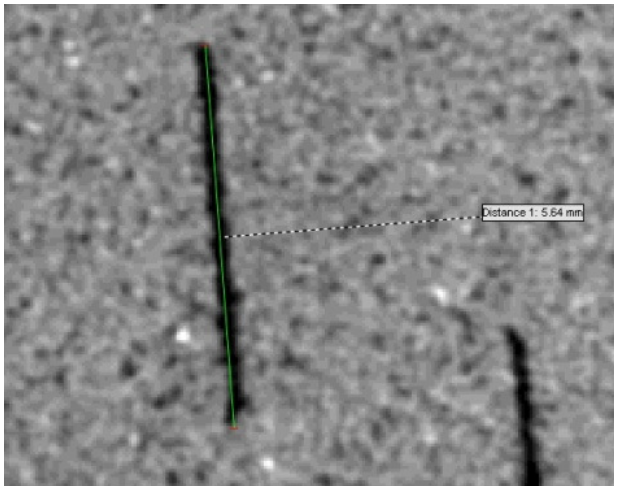

Figure 6.9: Zoomed in section from X-ray CT scan. Distance tool shows this individual penny-shaped fracture is 5.64 mm in length.

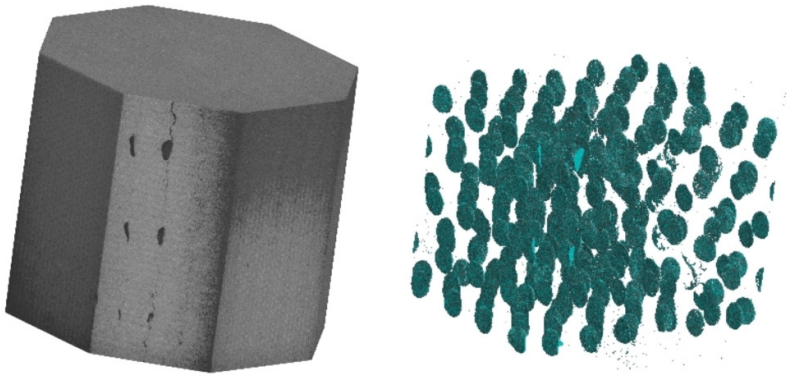

Figure 6.10: 3D volume image from CT scan. It shows the position of the fractures in the octagonal fractured plug. This allowed an accurate calculation of the fracture density to be made.

Unfractured sample	
Porosity, Φ_p	30%
Permeability, κ	21 mDarcy
Grain size	120 μm
Bulk density of air saturated rock, ρ_{air}	1826 kg/m^3
Bulk density of water saturated rock, ρ_{water}	2130 kg/m^3
Bulk density of glycerin saturated rock, $\rho_{glycerin}$	2193 kg/m^3
Fractured sample	
Porosity, Φ_p	33%
Permeability, κ	21 mDarcy
Bulk density of air saturated rock, ρ_{air}	1903 kg/m^3
Bulk density of water saturated rock, ρ_{water}	2232 kg/m^3
Bulk density of glycerin saturated rock, $\rho_{glycerin}$	2298 kg/m^3
Fracture density, ε_f	0.0314 ± 0.0059
Average fracture radius, a	2.91 ± 0.06 mm
Average fracture aspect ratio, r	0.0429 ± 0.0008

Table 6.1: Physical properties of the synthetic porous rock.

6.4 Ultrasonic bench top measuring technique.

Sample size constraints meant that blocks of insufficient size to core three directions relative to the fractures could be made (using the current construction technique). For this reason P-, S1 and S2-wave velocity and attenuation were measured through the octagonal shaped samples using a bench top configuration (Figure 6.11). In this configuration a transmitting transducer and receiving transducer were placed on opposing sides of the sample and pressed against the rock faces using a pneumatic ram to ensure consistent coupling between

experiments (Figure 6.12). The ram placed 0.5 MPa of pressure to the system.

A Panametrics PR500 pulse generator was used to drive a P-wave (Panametrics V101 transducer) or S-wave (Panametrics V151) transducer with central frequency of 500 kHz through the rock sample. The waveforms were recorded on a digital oscilloscope. As in the pulse-echo system coupling was required to ensure a signal could propagate between the transducer and rock contacts. For P-wave couplant, honey was used and for S-waves the same shear-wave couplant as used in the pulse-echo system was used.

To vary the measurement relative to the fracture normal the pressure was simply dropped and the rock rotated by 45° and the pressure reapplied. For each measurement direction a P-wave and both S1 (parallel to the fractures) and S2 (perpendicular to fractures) waveforms were recorded. Waveforms were not recorded until the amplitudes remained stable. They were stacked at least 500 times to improve the signal to noise ratio and then converted to ASCII as described in chapter 4. Velocity and attenuation were then calculated by comparing the recorded waveforms with that of a reference material (duralumin) in the Fourier domain (see chapter 6.5).

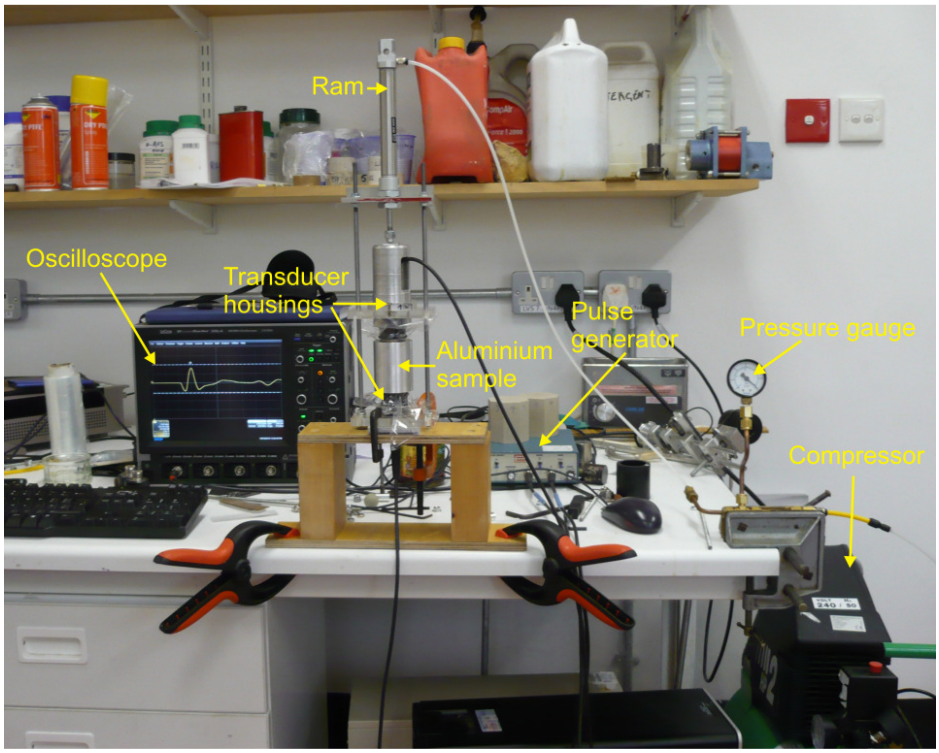

Figure 6.11: Bench top measuring system.

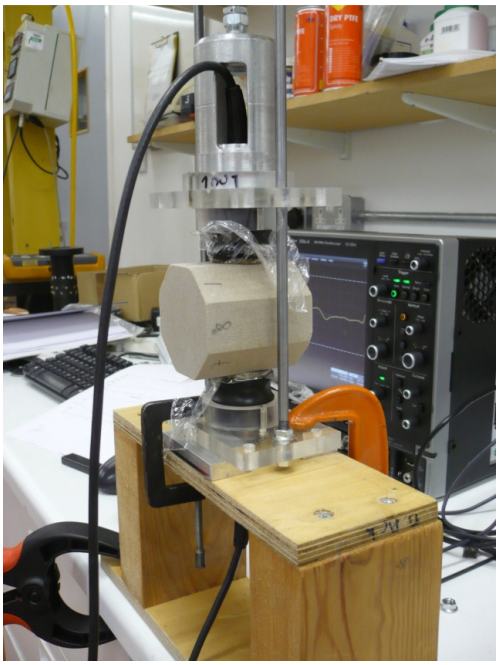

Figure 6.12: Air saturated sample between the two transducers. Coupling pressure is controlled by a pneumatic ram and couplant is used on the transducer faces.

For fluid saturated measurements, the samples were saturated with either water or glycerin using the methods described in chapter 4. To ensure that the combined properties of the rock matrix and saturating fluid were measured the samples were jacketed in a single layer of tin foil (10 μm thick; Figure 6.13). Without a jacket the measurements would have to be carried out in a bath of saturating fluid and the resultant measurements would be a function of the saturated rock and fluid within the bath (Gassman 1951). The increased length of the jacketed sample was accounted for in the velocity calculation. Any amplitude loss caused by the foil was corrected by re-measuring the duralumin sample waveforms with aluminium foil placed on each end of the sample.

The advantages of the system over the pulse-echo system are that it has a lower frequency (500 kHz compared to around 800 kHz), the full anisotropic elastic tensor can be measured from a single sample and that an anisotropic reflection coefficient is not required to calculated attenuation at 45° to the fracture normal. However, the system represents a non-optimum, but acceptable compromise between the accuracy of the pulse-echo system, taken to be double the error (velocity, 0.6% and attenuation, 0.2 dB/cm). The largest drawback of the system is not being able to measure samples under confining pressure.

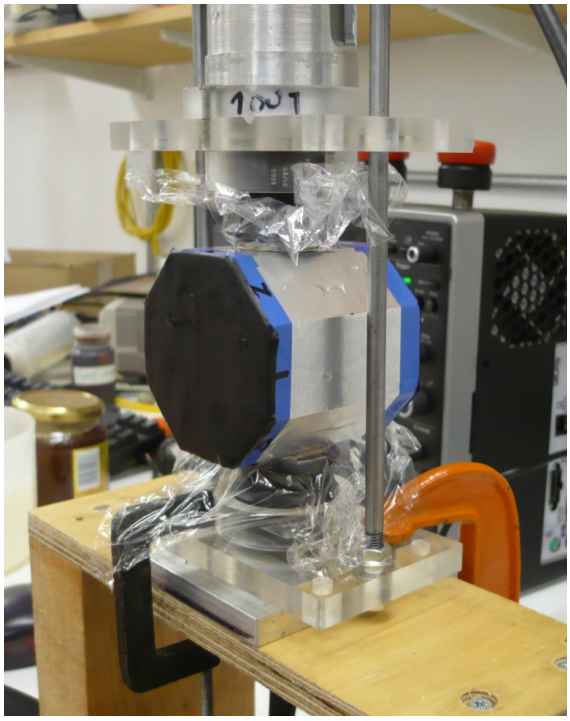

Figure 6.13: Fluid saturated sample with single thickness aluminium foil jacket.

6.5 Calculation of phase velocity.

The waveforms recorded through the rock sample are subject to time delays intrinsic to the measuring system caused by electrical delays within the transducers and oscilloscope. For this reason using a first break, or first zero crossing based on a speed = distance multiplied by time approach will give highly inaccurate values. Typically transmission experiments use an identical sized reference sample to rock sample to calibrate the measurements since only one single direction is measured through a sample. However, in this experiment, despite best efforts the distance between opposing sides on the octagonal samples were slightly different. It is possible to use a different length reference material to calibrate the rock sample using simple mathematical relations as long as the length and velocity of the reference material are known (Figure 6.14).

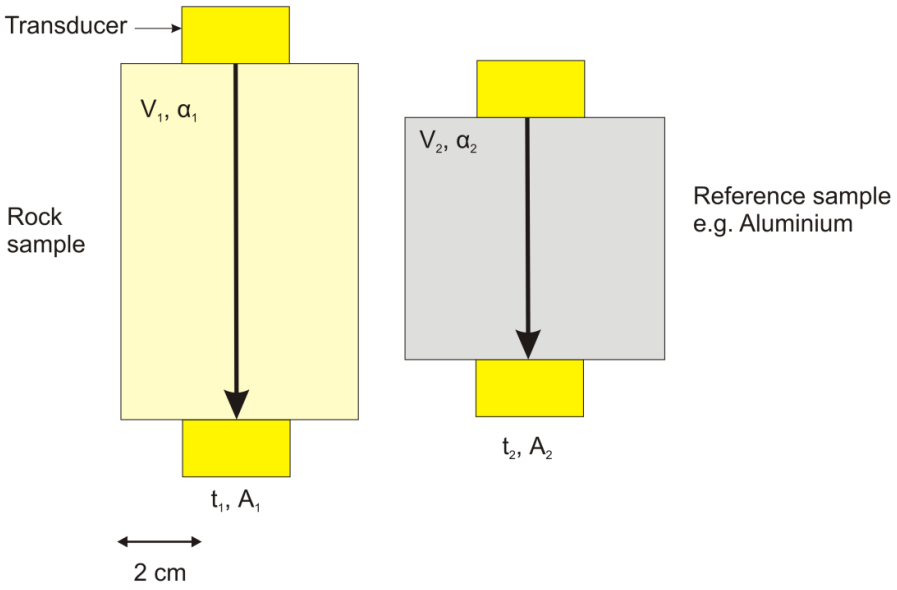

Figure 6.14: Transmission experiment using a different sized rock and reference sample.

The travel times though the rock sample (t_1) and reference duralumin sample (t_2) with different lengths x_1, and x_2, respectively are,

$$t_1 = t_{delay} + \frac{x_1}{V_1} + t_{diff1}\,, \tag{6.1}$$

$$t_2 = t_{delay} + \frac{x_2}{V_2} + t_{diff2}\,, \tag{6.2}$$

where, t_{delay} is the time delay associated with both experiments (assumed to be constant between samples), t_{diff1} and t_{diff2} are diffraction effects caused by beam spreading (see chapter 4.5) which are different for each sample. V_1 and V_2 is the velocity (P- or S-wave) of the rock sample (unknown) and duralumin, respectively. The velocity of duralumin is taken to be 6398 m/s for P-waves, and 3122 m/s for S-waves for all frequencies (Kaye and Laby 1995).

Phase velocity of the sample is calculated by taking the difference in travel time, thus cancelling out the unknown, but common delay times gives,

$$\Delta t = t_1 - t_2 = \left(\frac{x_1}{V_1} - \frac{x_2}{V_2}\right) + \left(t_{diff1} - t_{diff2}\right). \quad (6.1)$$

Let $\Delta t_{diff} = t_{diff1} - t_{diff2}$, and rearrange equation 6.3 to give,

$$V_1 = \frac{x_1}{\Delta t - \Delta t_{diff} + \frac{x_2}{V_2}}, \quad (6.2)$$

However, t_1, t_2, t_{diff1}, t_{diff2} and V_1 are functions of frequency. A Fourier transform can be used to analyse the phase angle spectra in the rock sample and reference sample.

The time spectra now become,

$$t_1(f) = t_A - \frac{\Phi_1(f)}{2\pi f}, \quad (6.3)$$

$$t_2(f) = t_B - \frac{\Phi_2(f)}{2\pi f}, \quad (6.4)$$

where, t_A and t_B are the start times of the windows (see Figures 6.15a and 6.16a), $\Phi_1(f)$ is the Fourier phase angle spectrum for the rock sample (radians), at frequency, f and $\Phi_2(f)$ is the Fourier phase angle spectrum for the reference sample.

Frequency-dependent phase velocity is therefore given by,

$$V_1(f) = \frac{x_1}{\Delta t(f) - \Delta t_{diff}(f) + \frac{x_2}{V_2}}. \quad (6.5)$$

The diffraction corrections are calculated using the Benson & Kiyohara (1974) tables as described in chapter 4.5.

6.6 Calculation of intrinsic attenuation coefficient.

By using a non-dispersive material with a known attenuation coefficient for the reference sample it is possible to compare the Fourier amplitude spectrums of the rock and reference sample, account for the differences in length and diffraction corrections to calculate the attenuation coefficient based on a spectral ratio method.

The Fourier amplitude spectrums of the rock sample (Figure 6.16b), A_1, and reference sample (Figure 6.15b), A_2, are given by,

$$A_1 = A_0 e^{-\alpha_1 x_1} e^{-d_1 x_1}, \tag{6.6}$$

$$A_2 = A_0 e^{-\alpha_2 x_2} e^{-d_2 x_2}, \tag{6.7}$$

where, A_0 is the initial amplitude, α_1 (nepers/m) is the attenuation coefficient of the rock sample, α_2 is the attenuation coefficient of the reference sample. d_1 is the amplitude diffraction correction for the rock sample and d_2 is the amplitude diffraction correction for the reference sample.

It follows that,

$$\frac{A_2}{A_1} = e^{-\alpha_2 x_2 + \alpha_1 x_1 - d_2 x_2 + d_1 x_1}, \tag{6.8}$$

hence,

$$\ln\left(\frac{A_2}{A_1}\right) = -\alpha_2 x_2 + \alpha_1 x_1 - d_2 x_2 + d_1 x_1 \,. \tag{6.9}$$

Rearranging gives,

$$\alpha_1 = \frac{1}{x_1}\left[\ln\left(\frac{A_2}{A_1}\right) + \alpha_2 x_2 + d_1 x_1 - d_2 x_2\right]. \tag{6.10}$$

Inverse quality factor, $Q_1^{-1}(f)$, in dB/m, is therefore given as,

$$Q_1^{-1}(f) = 8.686\left(\frac{V_1(f)\alpha_1(f)}{\pi f}\right). \tag{6.11}$$

An example duralumin P-wave wavelet showing windowing and corresponding Fourier amplitude spectrum are shown in Figures 6.15a and 6.15b. This can be compared to an example P-wave wavelet, windowing and Fourier amplitude spectrum from the water saturated fractured rock in Figures 6.16a and 6.16b, respectively.

The amplitude spectrums show that the duralumin has a larger amplitude than the wavelet from the rock. The peak of the amplitude spectrum for the duralumin is around 400 kHz and the rock sample a bit lower at around 325 kHz. These peaks are around the minimum threshold for edge effects and will exhibit large diffraction corrections. For this reason 500 kHz is used as the central frequency of the experiment, where both amplitude spectrums are still much larger than their minimum values.

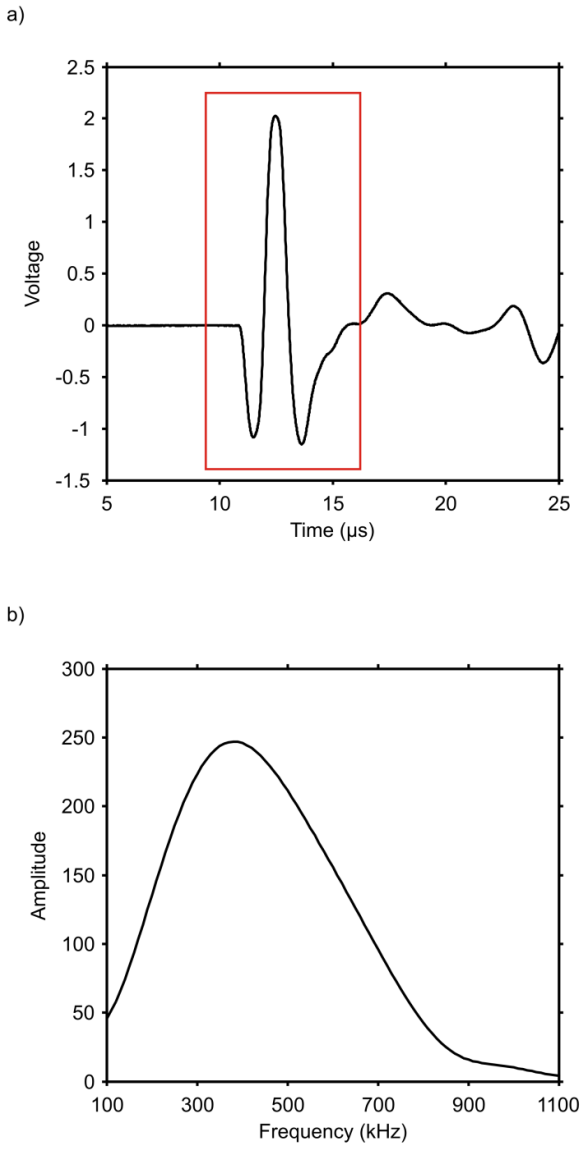

Figure 6.15: Example duralumin wavelet and windowing (a) with its corresponding Fourier amplitude spectrum (b).

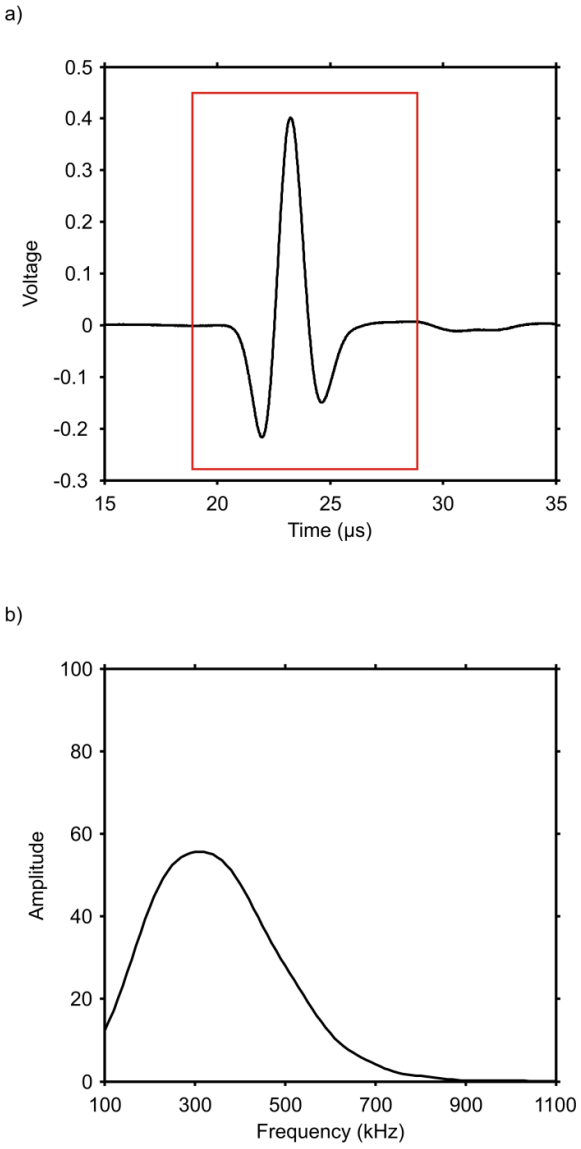

Figure 6.16: Example P-wave wavelet and windowing (a) with its corresponding Fourier amplitude spectrum (b) from the fractured rock sample when water saturated.

6.7 Phase or group velocity.

As in chapter 4, the wavefronts will suffer a lateral shift for the measurements at 45° to the fracture normal. Using equations (1) and (2) from Dellinger and Vernik (1994) the lateral translation at 45° was calculated for P-, S1- and S2-waves in the water saturated fractured rock. The translation for P-waves was found to be 2.91 mm for P-waves, 1.25 mm for S1-waves and -0.11 mm for S2-waves. The diameter of the transducer was 25.4 mm, therefore for all wavefronts, the lateral translation is much smaller than the radius of the receiving transducer and phase velocity is measured at 45° to the fracture normal.

6.8 Laboratory results.

Measurements are presented of P- and S-wave velocity and attenuation for both the unfractured and fractured samples. The samples were measured while saturated with air, water and glycerin saturation. Both samples were octagonal prisms, allowing four measurements at different angles to the layer and fracture normals to be made. The results show that the unfractured sample has measurable seismic anisotropy. By accounting for this extra anisotropy, the measurements of the fractured rock could be explained.

6.8.1 Unfractured rock velocity and attenuation anisotropy.

The experiments of chapter 5 showed that under raised effective confining pressures (10 – 60 MPa) the background anisotropy of the layered unfractured sample was small (< 0.5% shear-wave splitting). However, due to the nature of the bench-top experimental setup used in this chapter, measurements could only be carried out at atmospheric pressure; thus the anisotropy was expected due to the layering of the rock.

P-wave velocity is seen to vary between air (Figure 6.17a), water (Figure 6.18a) and glycerin (Figure 6.19a) saturations. The air saturated velocity is the slowest, and glycerin the fastest. Each saturation state shows that there is subtle variation of velocity with angle to the layer normal with the fastest velocity found at 90° to the layer normal, and the slowest at 45° to the layer normal.

P-wave attenuation magnitude is seen to vary for air (Figure 6.17b), water (Figure 6.18b) and glycerin (Figure 6.19b). In this case the water shows the largest attenuation and glycerin the smallest. However, it can be noted that for each saturation attenuation is seen to be the same for each angle to the layer normal within error.

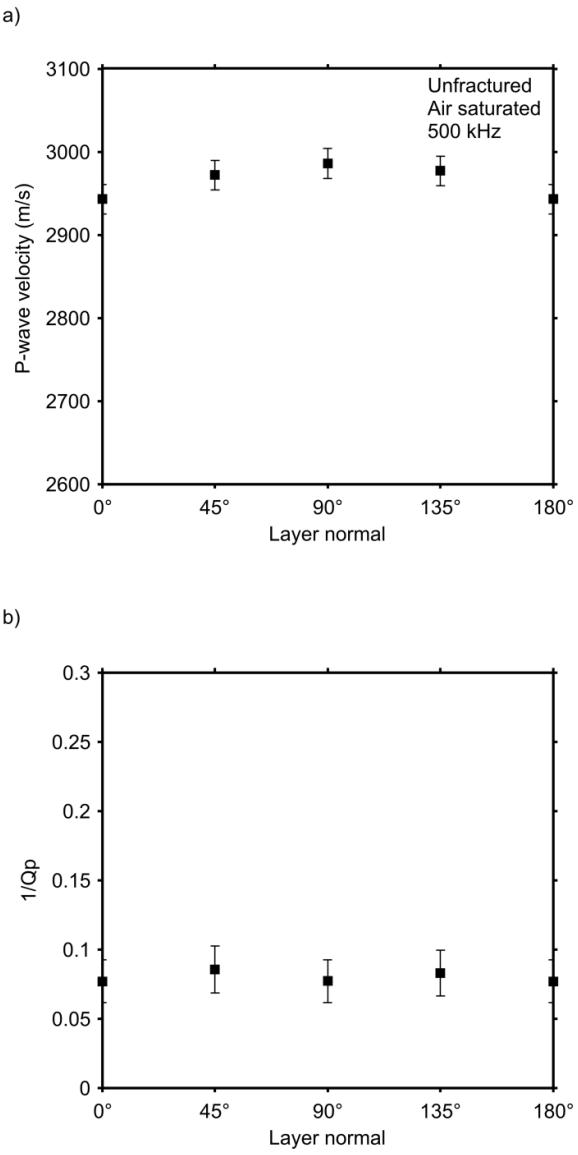

Figure 6.17: Air saturated P-wave velocity (a) and attenuation (b) relative to the layer normal direction.

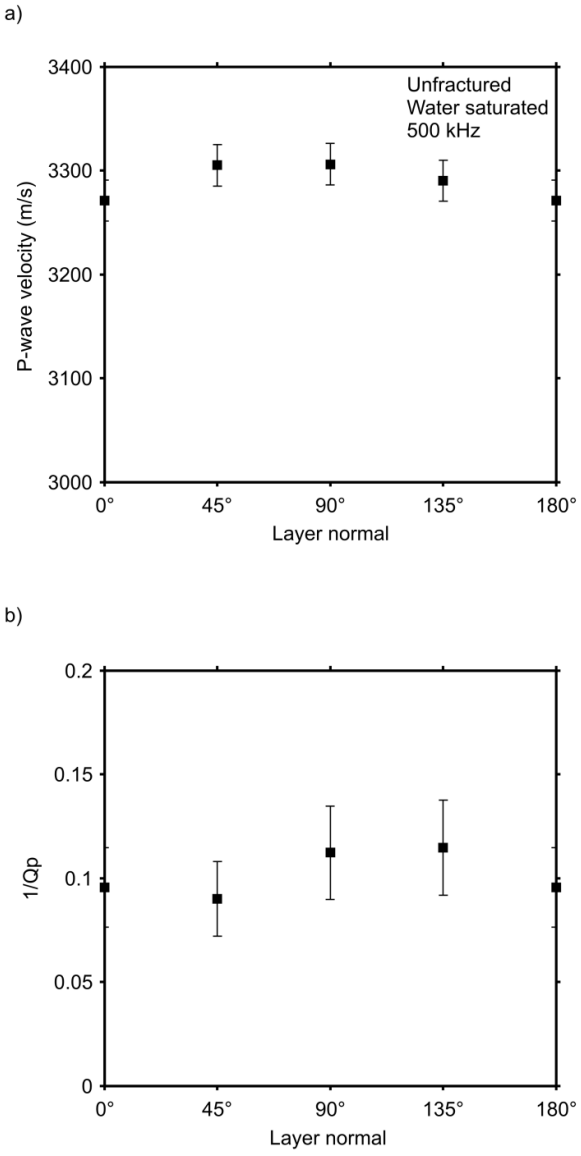

Figure 6.18: Water saturated P-wave velocity (a) and attenuation (b) relative to the layer normal direction.

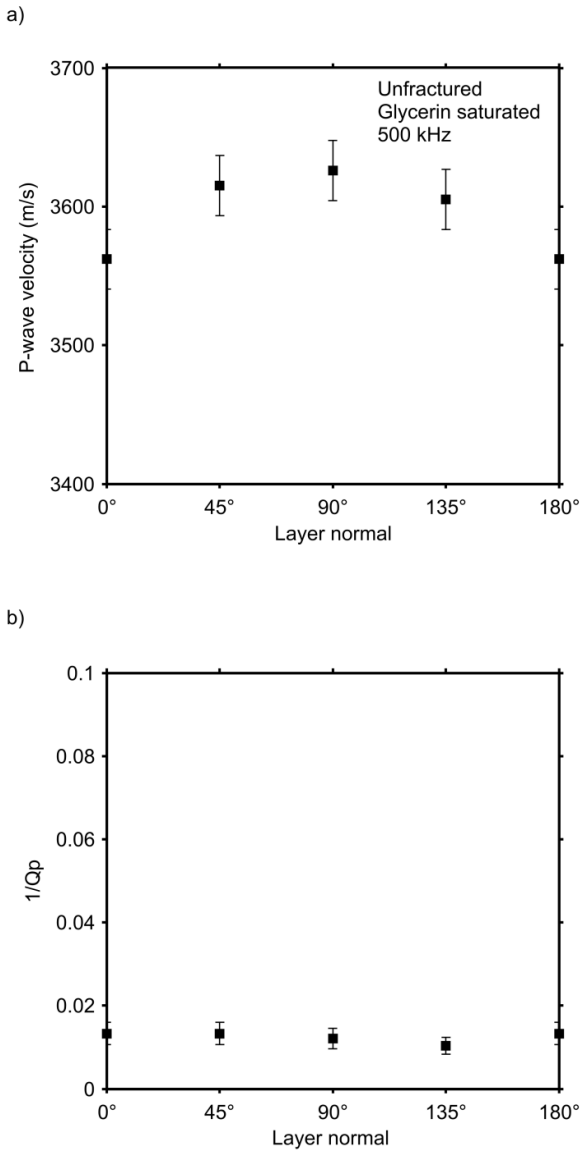

Figure 6.19: Glycerin saturated P-wave velocity (a) and attenuation (b) relative to the layer normal direction.

The S-wave velocity results for the unfractured rock show similar trends to the P-waves. In the air (Figure 6.20a), water (Figure 6.21a) and glycerin (Figure 6.22a) shear-wave splitting was observed. For example the water saturated results show shear-wave splitting is a maximum of 1.45 ± 1.18% at 90° to the layer normal, and a minimum of 0.00 ± 1.20% at 0° to the layer normal.

S-wave attenuation shows the smallest magnitude and small angular variations in the air saturated case (Figure 6.20b). However, in the water (Figure 6.21b) and glycerin (Figure 6.22b) the magnitudes are much larger and no angular variation is seen due to the layering.

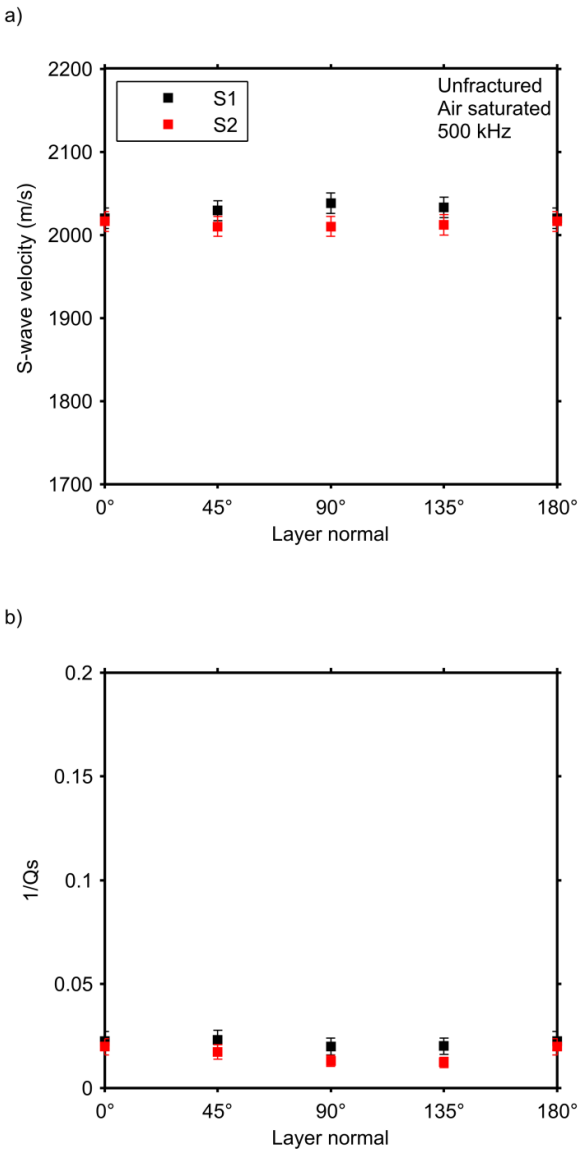

Figure 6.20: Air saturated S-wave velocity (a) and attenuation (b) relative to the layer normal direction.

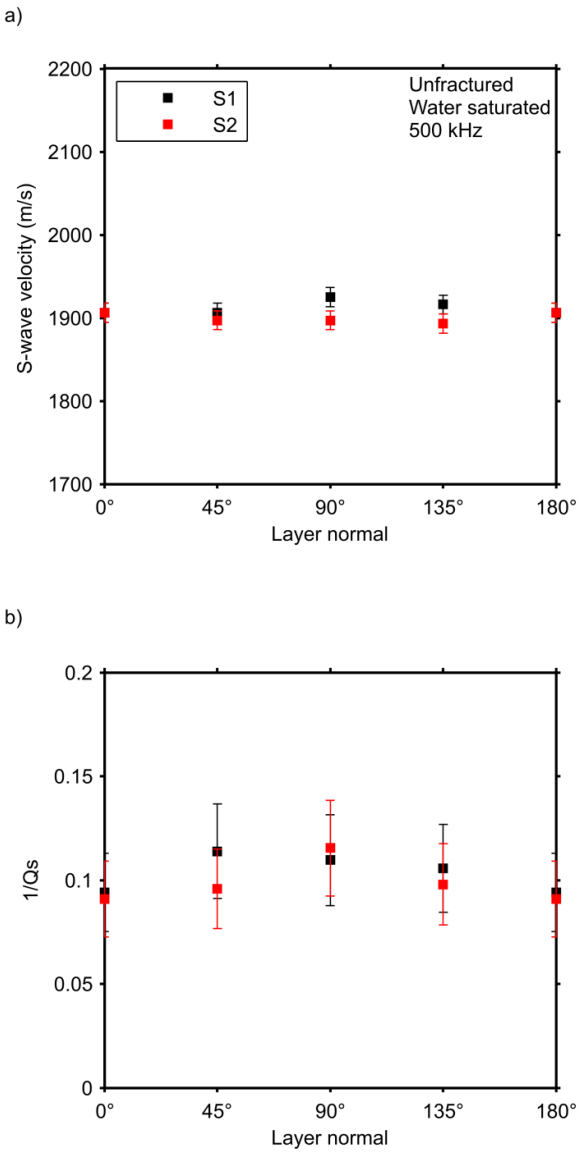

Figure 6.21: Water saturated S-wave velocity (a) and attenuation (b) relative to the layer normal direction.

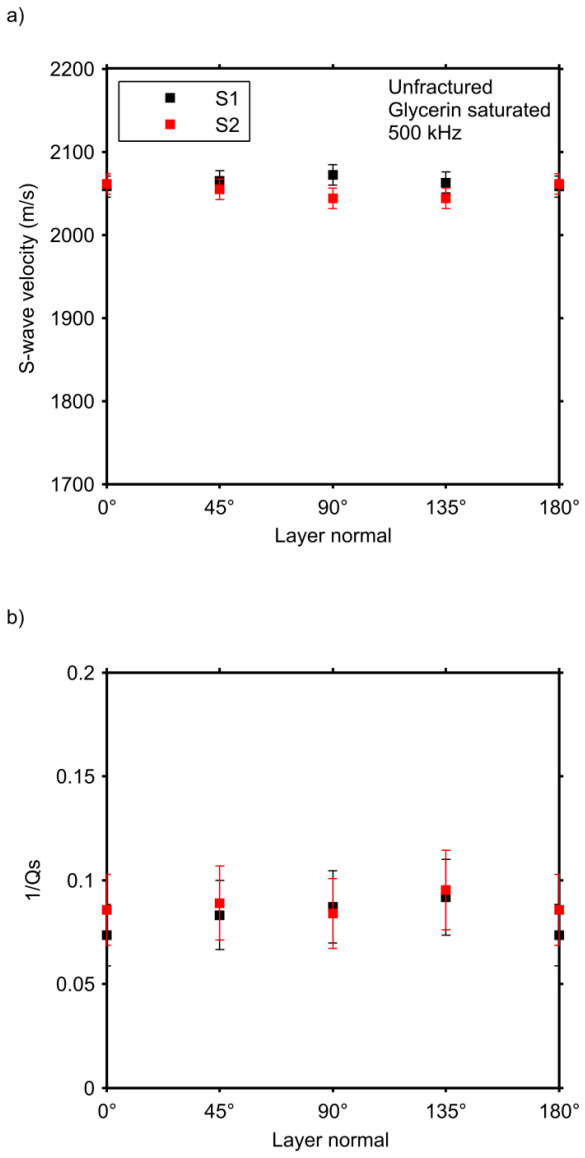

Figure 6.22: Glycerin saturated S-wave velocity (a) and attenuation (b) relative to the layer normal direction.

6.8.2 Fractured rock velocity and attenuation anisotropy.

The magnitude of P-wave velocity is seen to vary between air (Figure 6.23a), water (Figure 6.24a) and glycerin (Figure 625a) saturations; the air saturated velocity is the slowest and the glycerin saturated velocity is the fastest. It is evident that for all saturations significant velocity anisotropy is present with the fastest P-waves being measured at 90° to the fracture normal and slowest at 0° to the fracture normal for all saturations. The magnitudes of the measured velocity anisotropies will be discussed in the modelling section.

The P-wave attenuation measurements also show strong trends. For example, the overall magnitude of attenuation is seen to be the highest for air saturation (Figure 6.23b), intermediate for water (Figure 6.24b) and lowest for glycerin (Figure 6.25b). The variations with fracture direction mirror those of the P-wave velocity. The minimum attenuation is measured at 90° to the fracture normal and maximum at 0° to the fracture normal for all saturations.

Both the velocity and attenuation trends are consistent with interpretations of multi-azimuth field seismic data. The fracture strike is often interpreted as the direction of minimum P-wave travel-time (or fastest P-wave velocity) and attenuation (e.g. Hall and Kendall 2003, Clarke *et al.* 2009, Maultzsch *et al.* 2007, Maultzsch *et al.* 2009).

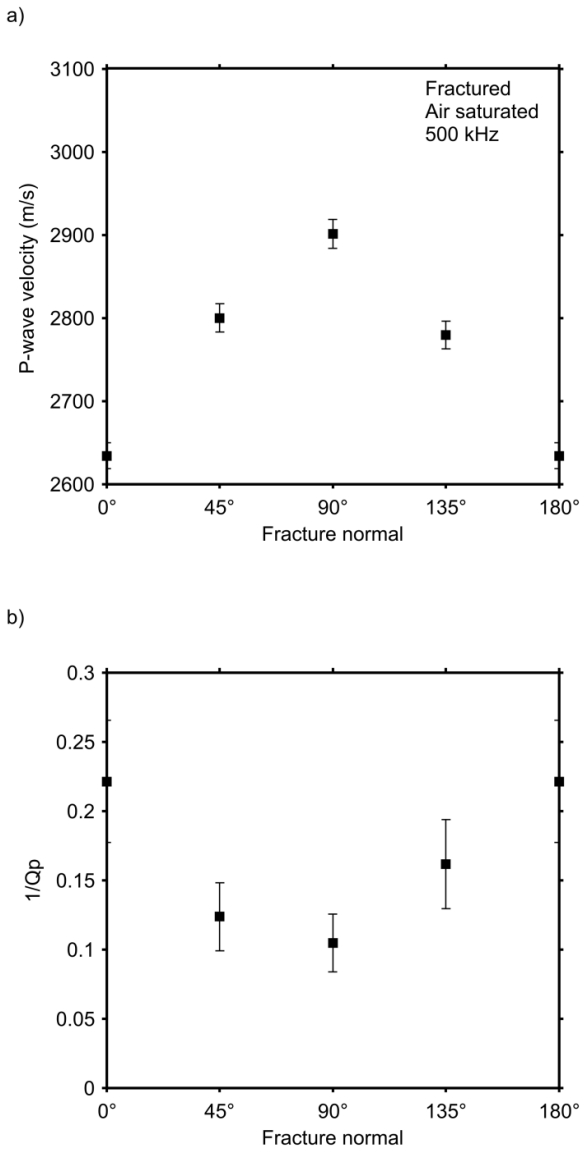

Figure 6.23: Air saturated P-wave velocity (a) and attenuation (b) relative to the fracture normal direction.

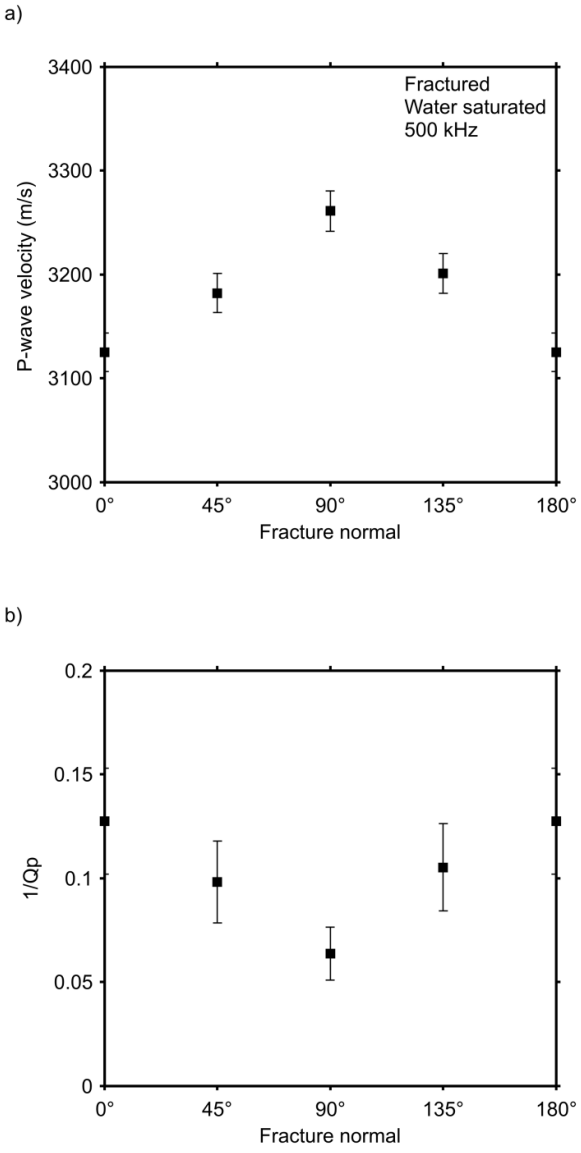

Figure 6.24: Water saturated P-wave velocity (a) and attenuation (b) relative to the fracture normal direction.

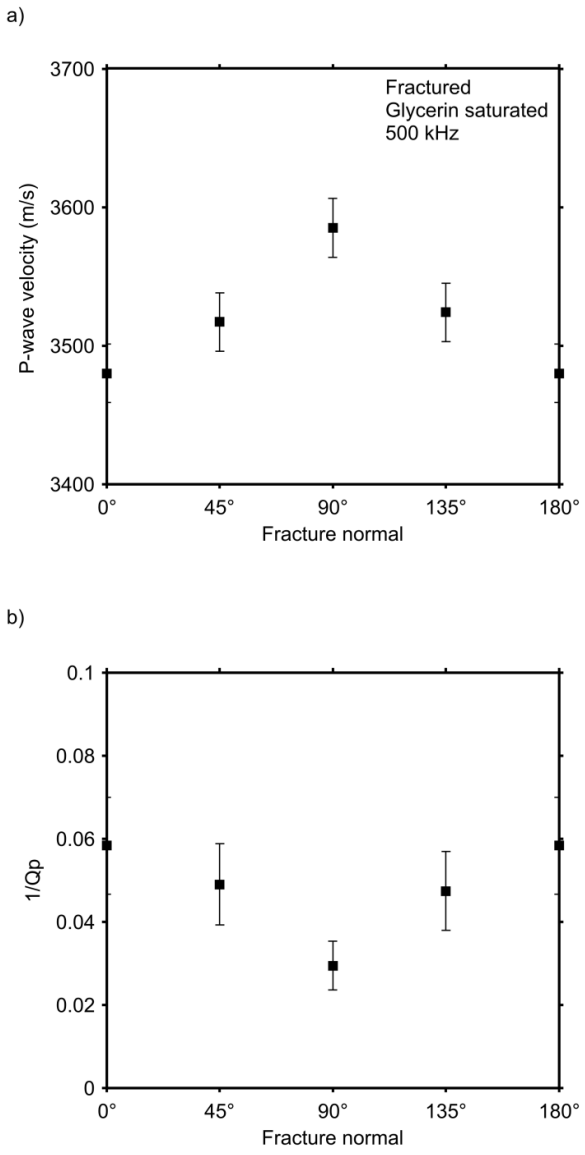

Figure 6.25: Glycerin saturated P-wave velocity (a) and attenuation (b) relative to the fracture normal direction.

S-wave velocity measurements also show the same magnitude of velocity changes as the P-waves for air (Figure 6.26a), water (Figure 6.27a) and glycerin (Figure 6.28a) saturation. These poro-visco-elastic interactions are responsible for controlling shear-wave anisotropy variations seen between the three fluid saturations as a function of fracture direction. For all saturations maximum shear-wave splitting is found at 90° to the fracture normal, for air = 5.65 ± 1.13%, for water = 6.57 ± 1.12% and for glycerin = 5.13 ± 1.14%. This result shows that shear-wave splitting is independent of fluid saturation for S-wave propagation at 90° to the fracture normal. Shear-wave splitting at 0° to the fracture normal does not exceed 0.42 ± 1.19% for all saturations in agreement with theory that predicts 0% at this angle (e.g. Hudson 1981). However, it is at 45° to the fracture normal where interesting variations are seen. At this angle shear-wave splitting is found to be for air = 4.58 ± 1.15%, water = 2.56 ± 1.17% and glycerin -0.67 ± 1.21%. Of particular interest is the positive to negative shear-wave splitting flip measured between the water and glycerin saturated measurements. This is discussed in more detail below.

The S-wave attenuation measurements also show the same angular variations as the P-wave attenuation measurements; the minimum attenuations measured for air (Figure 6.26b), water (Figure 6.27b) and glycerin (Figure 6.28b) are all found at 90° to the fracture normal. Maximum attenuation was also found for all saturations at 0° to the fracture normal. It is also interesting to note that the individual attenuations for the S1- and S2-waves mirror each other (within experimental error) in their azimuthal variations.

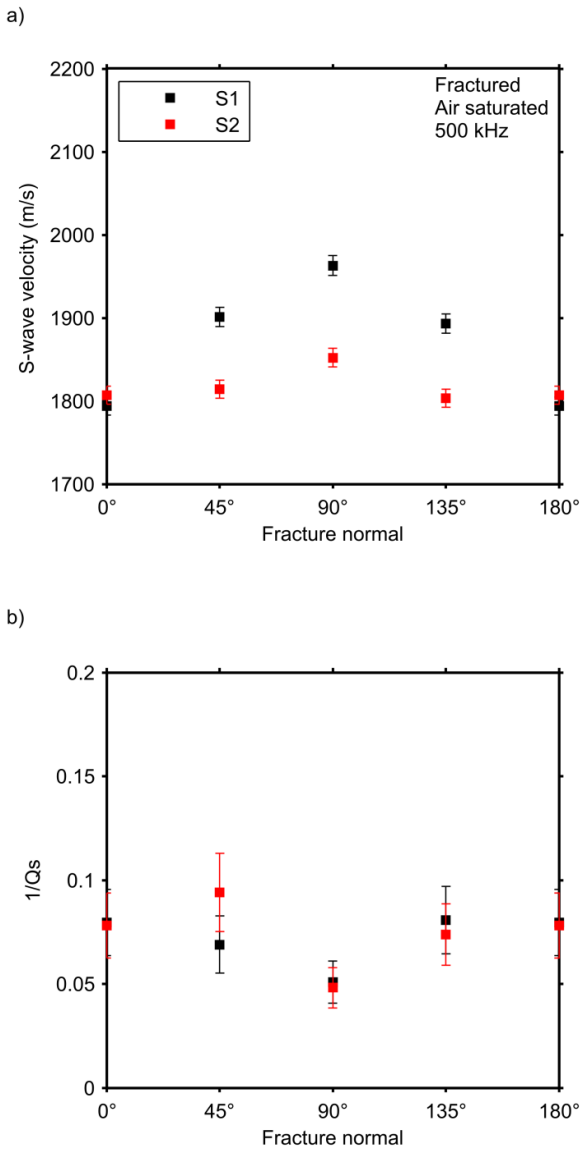

Figure 6.26: Air saturated S-wave velocity (a) and attenuation (b) relative to the fracture normal direction.

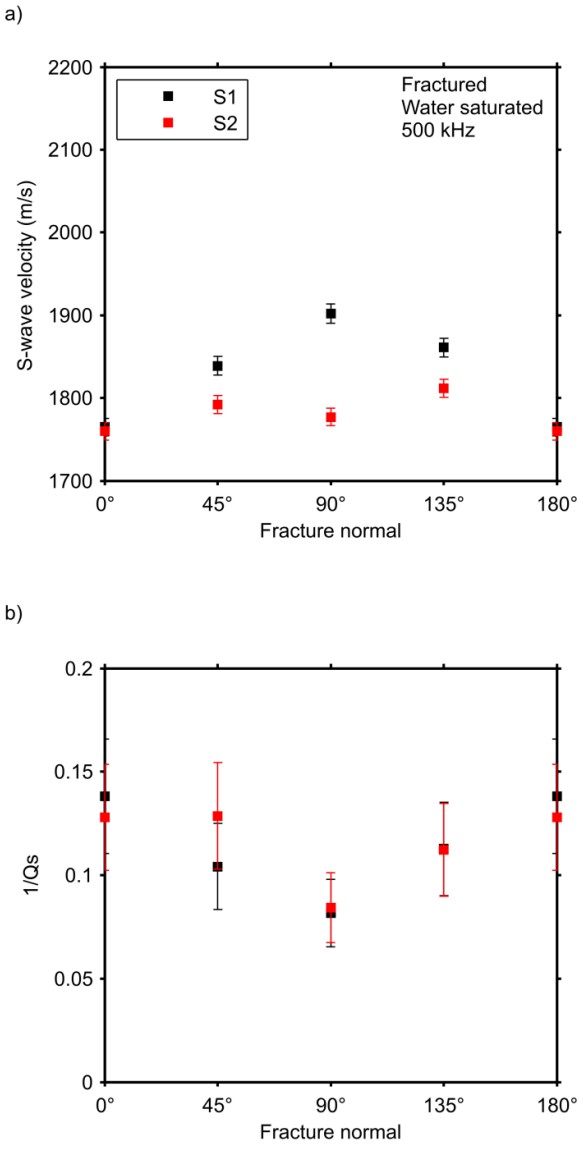

Figure 6.27: Water saturated S-wave velocity (a) and attenuation (b) relative to the fracture normal direction.

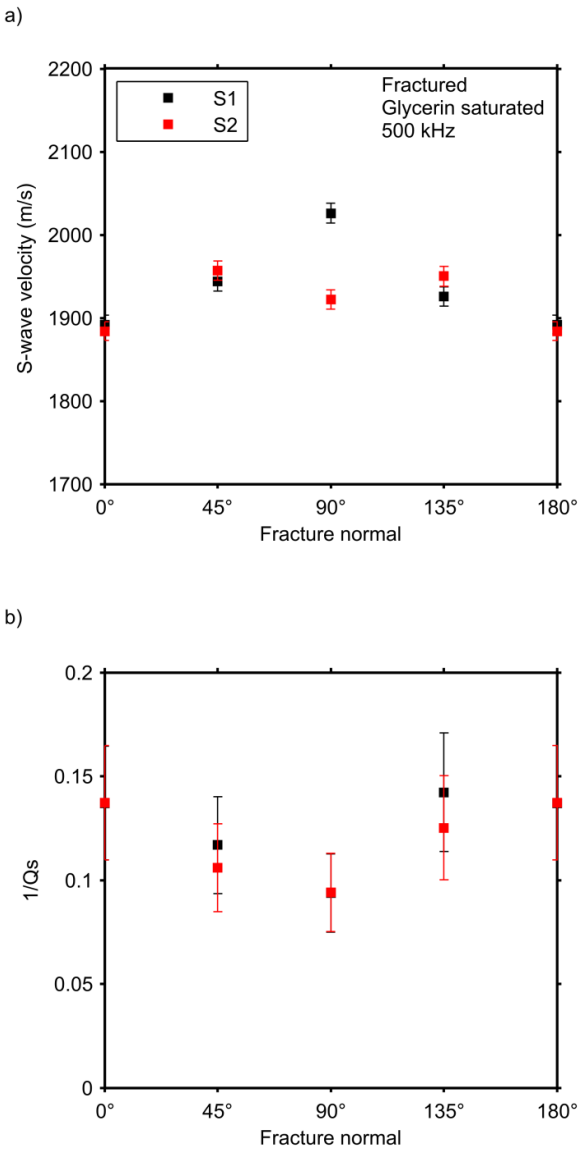

Figure 6.28: Glycerin saturated S-wave velocity (a) and attenuation (b) relative to the fracture normal direction.

6.9 Modelling results.

The data collected from the unfractured sample showed that the background unfractured layered rock showed anisotropy. To explain the results I will apply a modified version of the Chapman (2003) model which includes background anisotropy. The results will only concentrate on velocity and not attenuation. The reason for this is because some of the attenuation measurements in the unfractured sample were larger than in the fractured sample. For this reason the background and fracture induced attenuation effects cannot be distinguished. This may have been caused poor coupling in particular for the water saturated measurements. The angular variations of attenuation were negligible in the unfractured layered sample but showed pronounced changes with fracture direction, therefore a qualitative interpretation about this can be made. Despite this, the velocity results based on travel time changes remain valid and will be the focus of the modelling.

6.9.1 Accounting for background anisotropy in the Chapman (2003) model.

It is evident from Figures 6.18a and 6.21a that the background unfractured layered rock properties show transverse isotropy. For this reason, to model the anisotropy due to the fractures, the anisotropy of the layering must also be taking into account. The full elastic stiffness tensor of the background unfractured rock can be calculated from 5 velocity measurements relative to the symmetry of transverse isotropy, in this case the layering. The required velocities are $V_P(0°)$, $V_P(45°)$, $V_P(90°)$, $V_{S1}(90°)$ and $V_{S1}(0°)$ or $V_{S2}(90°)$. These were all measured at 500 kHz, the same as for the fractured rock measurements. The five independent constants making up the stiffness tensor can be calculated using the equations of Mavko *et al.* (1998) and form the new, measured tensor, $C_{ijkl}^{background}$. Their fit to the unfractured water saturated data are

shown in Figure 6.29. We therefore modify equation 3.14, replacing $C^0_{ijkl}(\Lambda, \mathrm{M}, \omega)$ with $\left[C^{background}_{ijkl} + \Phi_{c,p} C^1_{ijkl}(\lambda^o, \mu^o, \omega, water)\right]$ to allow the model to predict new fluid saturations from the water saturated measurements, giving

$$\begin{aligned} C_{ijkl}(\omega) = & \left[C^{background}_{ijkl} + \Phi_{c,p} C^1_{ijkl}(\lambda^o, \mu^o, \omega, water)\right] \\ & - \Phi_p C^1_{ijkl}(\lambda^o, \mu^o, \omega, fluid) - \varepsilon_f C^2_{ijkl}(\lambda^o, \mu^o, \omega, fluid) \\ & - \varepsilon_c C^3_{ijkl}(\lambda^o, \mu^o, \omega, fluid). \end{aligned} \tag{6.12}$$

The final C_{ijkl} tensor now takes account of the anisotropy associated with the layering and fractures. The corrections associated with porosity and the fractures are still calculated based on an isotropic background medium and use isotropic input $\mathrm{V_P^o}$ and $\mathrm{V_S^o}$ velocities to greatly simplify the equations. Any errors associated with the assumption of an isotropic background for the fracture corrections will be minimal since the small deviations in λ^o and μ^o caused by the background anisotropy are both multiplied by the fracture density (ε_f = 0.0314). Note ε_c is set to zero.

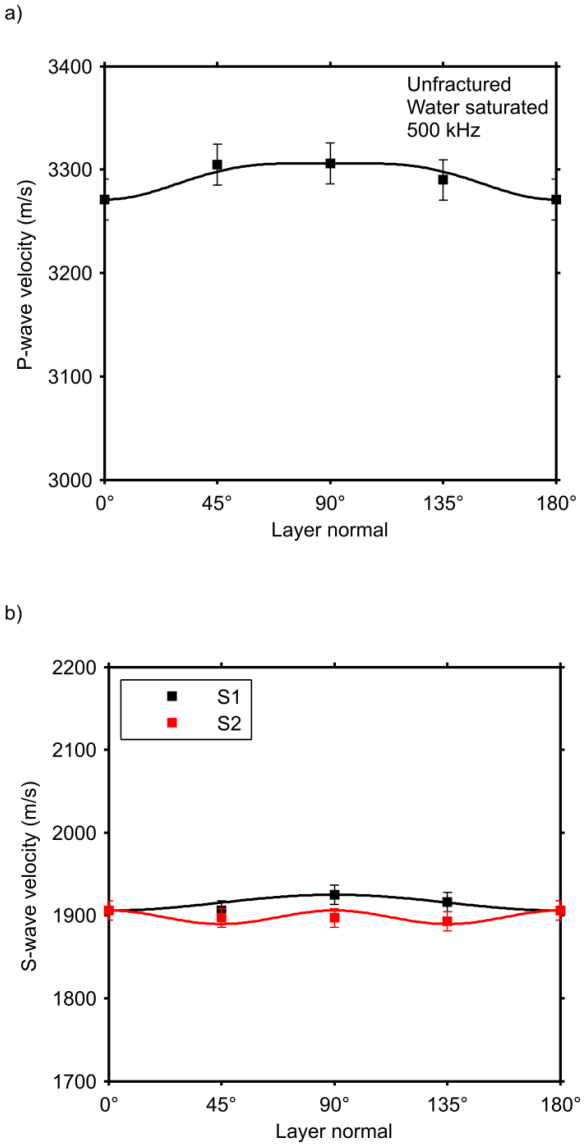

Figure 6.29: Fit of the background anisotropy to the unfractured water saturated P-wave (a) and S-wave (b) velocity data.

6.9.2 Model parameterisation.

Table 6.2 shows the model parameters used to implement the theory of Chapman (2003). The only free variable that requires fitting to the data is the microcrack relaxation time, τ_m. The fracture relaxation time, τ_f, is derived from this value through model relationships incorporating the known fracture radius *a* and grain size ς (equation 3.8).

P-wave velocity, V_P^o	3261 m/s
S-wave velocity, V_S^o	1902 m/s
Observation frequency, f_0	500 kHz
Pore fluid bulk modulus (air), k_{air}	0.000141 GPa
Pore fluid bulk modulus (water), k_{water}	2.19 GPa
Pore fluid bulk modulus (glycerin), $k_{glycerin}$	4.40 GPa
Pore fluid viscosity (air), η_{air}	0.00182 cP
Pore fluid viscosity (water), η_{water}	1 cP
Pore fluid viscosity (glycerin), $\eta_{glycerin}$	100 cP

Table 6.2: Model input parameters for the water saturated synthetic porous rock.

The value of τ_m was sought that minimised the relative difference between the measured and model predictions of the Thomsen anisotropy parameters (see Thomsen 1986), "epsilon" (ε), "gamma" (γ) and "delta" (δ) for the water saturated fractured measurements at 500 kHz. The measured and modelled elastic tensors were used in condensed voigt notation form. This approach produced the best overall fitting model without biasing it towards any single velocity mode.

The parameter ε represents the difference in P-wave velocity between the vertical (90°) and horizontal (0°) directions and is given by

$$\varepsilon = \frac{c_{11} - c_{33}}{2c_{33}}. \qquad (6.13)$$

γ represents the difference in S1-wave velocity between the vertical (90°) and horizontal (0°) directions and is given by

$$\gamma = \frac{c_{66} - c_{44}}{2c_{44}}. \tag{6.14}$$

δ is a combination of elastic moduli and controls the near-vertical anisotropy; it does not include any horizontal velocity terms. It is considered a critical measure of anisotropy for application to field seismology but is rarely measured in experimental data (Thomsen 1986). It is given by

$$\delta = \frac{(c_{13} + c_{44})^2 - (c_{33} - c_{44})^2}{2c_{33}(c_{33} - c_{44})}. \tag{6.15}$$

The relative difference between the measured and model predicted Thomsen parameters as a function of τ_m are shown in Figure 6.30. A minimum is clearly located at τ_m = 2.4 x 10^{-8} s. In fact, the curve suggests that the data best suit a high-frequency model because the differences are smaller at larger values of τ_m (i.e., higher values of relaxation frequency = $1/\tau_m$) than at lower values of τ_m. In the high-frequency limit the fluid within the fractures become increasingly isolated from the surrounding pore space and leads to unrelaxed poro-visco-elastic behaviour.

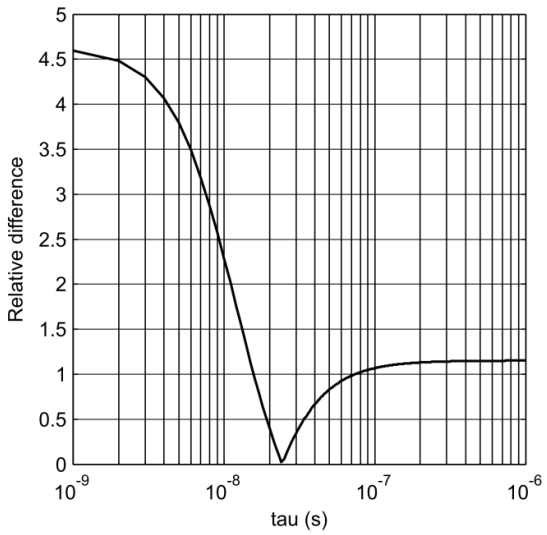

Figure 6.30: Relative difference between the predicted and observed Thomsen parameters as a function of microcrack relaxation time τ_m; note minimum at $\tau_m = 2.4 \times 10^{-8}$ s.

The best fitting model to the water saturated fractured velocity data is shown in Figure 6.31. It can be seen that the observed P-wave velocities (Fig. 12a) are slightly under estimated, however the shape and degree of anisotropy matches the data well. This difference in velocity comes as a result of using $C_{ijkl}^{background}$ from the unfractured rock as it has a slightly different density to the fractured rock (see Table 1). S-wave velocities (Fig. 12b) show a better fit to observations in terms of velocity magnitude and the model successfully predicts the shape of angular variations for the S1 and S2-waves.

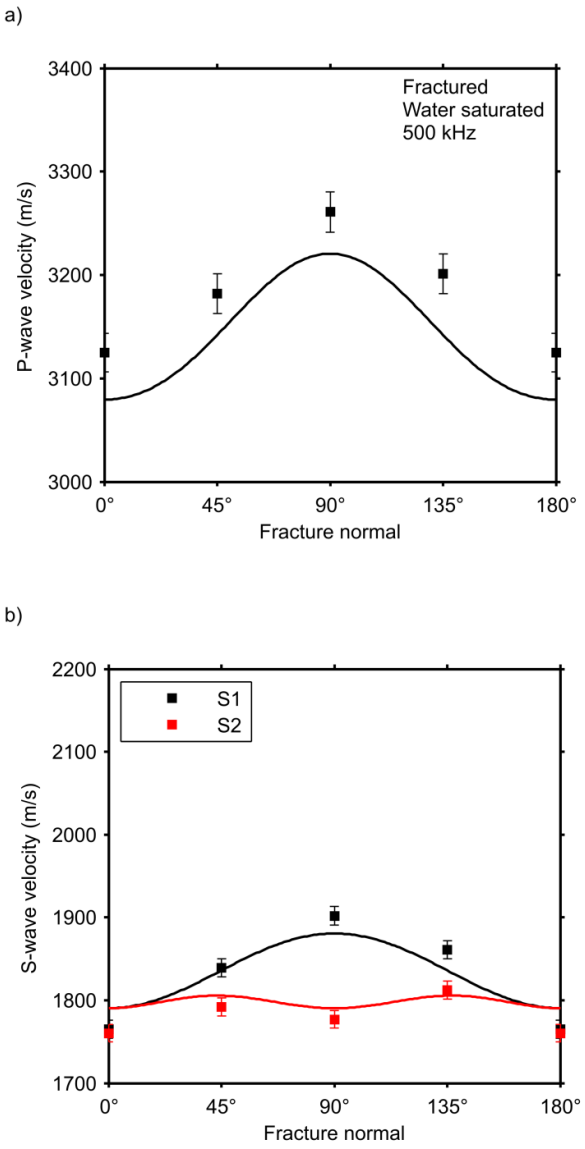

Figure 6.31: Best fitting model to the water saturated fractured rock P-wave (a) and S-wave (b) velocity data.

A frame stiffening effect appears to be responsible for the high glycerin velocities (Marketos and Best 2010). This effect results in higher velocities than can be predicted by theory. However, it is still instructive to evaluate the variations of velocity anisotropy with fracture normal direction as a result of viscosity and bulk modulus effects.

The magnitude of attenuation measured is also an order too high to be modelled using theory. This is attributed to scattering effects caused by the seismic wavelengths being close to the fracture size. Despite the bench-top measuring system using a lower frequency than the previous Tillotson *et al.* (2011) study (500 kHz as opposed to750 kHz), a larger fracture size results in seismic wavelength to fracture size ratios of around 1.1 : 1 for P-waves and 0.6 : 1 for S-waves. Despite these ratios, the laboratory results show clear azimuthal trends and minimum attenuation in the fracture strike plane showing potentially how robust these observations could be.

6.9.3 Fluid-dependent shear-wave splitting.

A key finding of Chapter 4 was an observation and quantification of the sensitivity of shear-wave splitting to fluid viscosity at 45° to the fracture normal. This sensitivity of shear-waves to fluid viscosity could have implications for the discrimination of oil and water in fractured reservoirs (Qian *et al.* 2007). For these measurements the results are analysed in the same manner.

The aspect ratio of the fractures, r = 0.0429, was constrained to a high accuracy using X-ray CT scanning at atmospheric pressure, the same pressure as the ultrasonic measurements. Modelling results showed that at this aspect ratio both fluid viscosity and bulk modulus appear to be responsible for the observed variations of anisotropy. Figure 6.32 shows the model sensitivity to aspect ratio, fluid viscosity and bulk modulus. It can be seen that at larger aspect ratios (r = 0.1), shear-wave splitting is sensitive to both k_f = 2.19 GPa, and k_f = 4.4 GPa

over a range of viscosities, however at smaller aspect ratios (0.001) this sensitivity disappears.

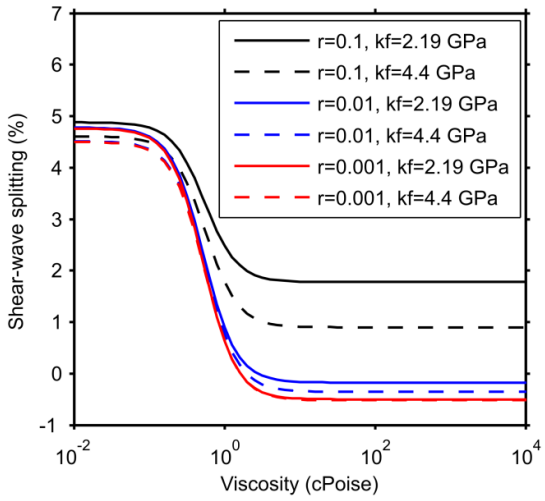

Figure 6.32: Sensitivity of shear-wave splitting at 45° to the fracture normal to fracture aspect ratio (r) at, fluid viscosity and fluid bulk modulus (kf) as predicted by the Chapman (2003) model.

Figure 6.33 shows the measured and model predicted shear-wave splitting as a function of fracture direction for water and glycerin saturation. The measurements show that at 0° to the fracture normal, shear-wave splitting is close to zero for both saturations, in line with model predictions. At 90° to the fracture normal, both saturations measure around 6% shear-wave splitting, broadly matching the model which predicts that percentage shear-wave splitting will be one hundred times the fracture density plus background anisotropy. At 45° to the fracture normal shear-wave splitting is distinctively different between the two fluid saturations. The water saturated shear-wave splitting is measured to be 2.56 ± 1.17% and glycerin, -0.67 ± 1.21%. A polarisation flip was also seen at this angle to the fracture normal for variations of shear-wave splitting due to fluid viscosity in Tillotson *et al.* (2011). It can be seen that the model predicts a polarisation flip based on both

changes in viscosity and bulk modulus at angles around the same as our measured values.

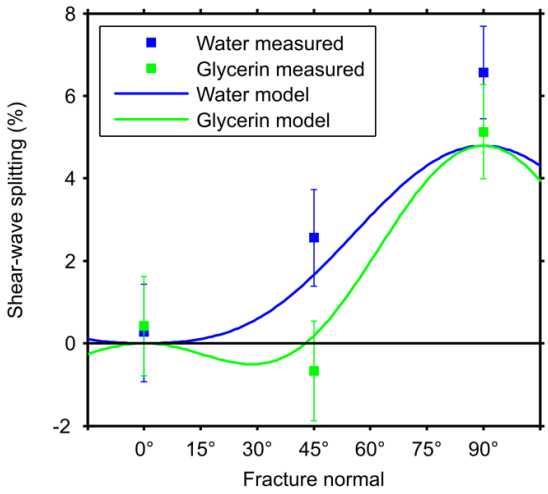

Figure 6.33: Comparison of model predictions of shear-wave splitting with observations relative to the fracture normal and fluid saturation. Black line indicates 0% shear-wave splitting.

6.9.4 Thomsen parameter modelling.

Thomsen's anisotropy parameters (Thomsen 1986) are a neat convenient way to describe the anisotropy in a transversely isotropic medium. We compare the measured and model predictions for ε, γ and δ based on changes in bulk rock density, fluid viscosity and fluid bulk modulus.

ε, the P-wave anisotropy parameter, is predicted by the model to decrease with increasing fluid viscosity and bulk modulus (Figure 6.34). We show that the measured values compare well to the predicted values for water and glycerin saturation. Qualitatively, the air saturated measurement and model predictions agree that epsilon should be much larger than the water and glycerin saturations.

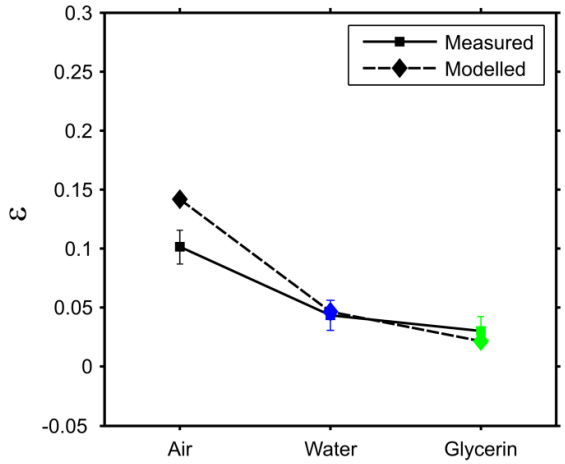

Figure 6.34: Comparison of model predictions and observations of ε for air, water and glycerin saturation.

γ, the S-wave anisotropy parameter is predicted to be independent of saturating fluid properties (Figure 6.35). Our measurements show that the air and glycerin gamma show a very good match with the model predictions, and that water broadly matches the prediction.

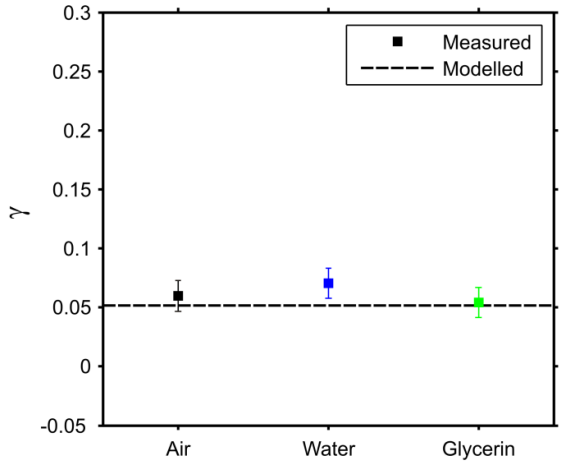

Figure 6.35: Comparison of model predictions and observations of γ for air, water and glycerin saturation.

The final parameter we measure and model is δ, a complex combination of elastic terms that describe the near vertical motion of P- and S1-waves. As with the model and measured epsilon, we are able to match the water and glycerin predictions with the measured data (Figure 6.36). The air saturated model and measurements are both a magnitude higher than the water and glycerin saturations and show fair agreement.

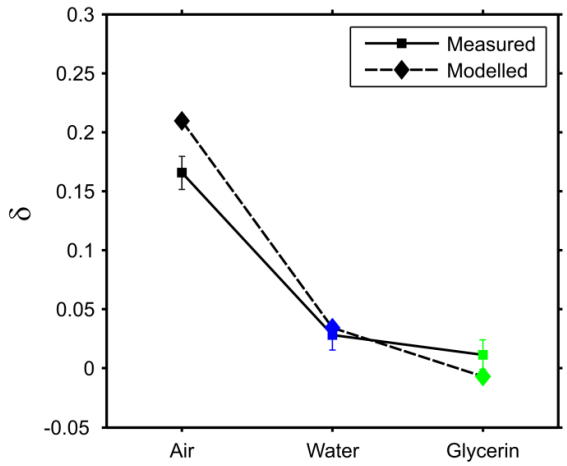

Figure 6.36: Comparison of model predictions and observations of δ for air, water and glycerin saturation.

6.10 Conclusions.

To date only a handful of laboratory validations of fracture theories exist and have all suffered from unrealistic rock properties. To test these theories, rocks with controlled fracture properties including shape, size and distribution, are required. Using the method outlined in Chapter 5, synthetic silica cemented rocks with a controlled distribution of penny-shaped voids were produced. By using larger, 7 cm diameter, octagonal shaped rocks with 25 mm wide faces and a bench-top ultrasonic pulse transmission system it was possible to measure, using a reference sample, P-, S1- and S2- phase velocity and attenuation for air, water and glycerin saturation. By measuring velocity in all the required directions the full anisotropic elastic tensor of the unfractured and fractured rock samples was measured. The unfractured rock showed small levels of anisotropy and as a result was incorporated into the modelling.

The laboratory velocity and attenuation results qualitatively confirm previous understanding. For example field seismic data that shows

azimuthal anisotropy is often interpreted as system of aligned fractures. The fracture strike is interpreted as the direction of minimum attenuation and maximum P- & S1-wave velocity. The maximum shear-wave splitting direction can also give the fracture strike and density. These interpretations are all independent of fluid saturation. Our laboratory velocity and attenuation results confirm all these techniques for three different fluid saturations, however our maximum percent shear-wave splitting was found to equal 100 times the fracture density plus background layering anisotropy. We note the robustness of the results given the similarity of the wavelength to fracture size ratio resulting in high levels of scattering.

By incorporating the measured background anisotropy into the Chapman (2003) model we modelled both shear-wave splitting as a function of fracture normal direction and more general predictions of the model using the Thomsen anisotropy parameters. Despite equivalent medium criteria being violated (the wavelengths were about the same as the fracture size) the theory is able to explain the observed variations in anisotropy related to fluid viscosity and bulk modulus.

A shear-wave splitting polarisation flip is seen at 45° to the fracture normal for glycerin saturation. This flip is theoretically attributed to both fluid viscosity and fluid bulk modulus given the fracture aspect ratio and shows good agreement with the laboratory data. The same theory was used to quantify fluid-dependent shear-wave splitting by Tillotson *et al.* (2011). The agreements in the findings between the two studies imply that the analysis of reflected S-wave data for discrimination between, for example, oil and water in fractured reservoirs should be studied in detail and could offer a robust alternative to traditional fluid substitution methods based on P-wave reflection data.

Theory was also used to predict the anisotropic response of the fluid saturated rock using Thomsen's anisotropy parameters. Using a single model fitting based on the water saturated model, it was possible to accurately predict ε and δ based on variations of fluid viscosity and bulk modulus for air and glycerin saturation. Of particular note was the

large variation for air saturation where these parameters have significant separation from the water and glycerin saturation measurements. Thomsen's S-wave anisotropy parameter, γ, was as expected, found to be independent of model fitting. This is particularly of interest since it is possible to directly predict gamma from analysis of X-ray CT scanning without needing to know the velocity of the rock.

The theory relates the anisotropic response of the rock based on the physical size of the fractures and saturating fluid properties. These findings therefore give some confidence to the use of the theory for quantitative analysis of seismic anisotropy in fractured reservoirs based on the physical fracture properties. This is in contrast to a common perception that only fracture compliance can be deduced and interpreted from seismic data.

Chapter 7

Discussion and conclusions.

7.1 Introduction.

In this thesis I have measured and analysed laboratory ultrasonic measurements of P- & S-wave velocity and attenuation from three different synthetic porous fractured rock samples. The experiments broadly showed that, despite the violation of equivalent medium criteria the Chapman (2003) theory was able to describe several aspects of the ultrasonic results. For clarity, I summarise the main conclusions of the thesis below for each experiment.

7.2 Summary of results.

7.2.1 Experiment I (Chapter 4).

The first experiment used the pulse-echo system. In this experiment measurements were performed on two cores (50 mm diameter, 20 - 30 mm in length) from a single block of porous synthetic fractured material manufactured by the Chinese National Petroleum Corporation (CNPC). Successful measurements were made in the cores orientated at 45° and 90° to the fracture normal and measured water and glycerin saturated. A third core at 0° to the fracture normal was too highly attenuation to give meaningful results.

The measurements in the 45° and 90° to the fracture normal cores were carried out under water (1 cPoise) and glycerin (100 cPoise) saturations. The aim of the two different saturations was to observe any poro-visco-elastic effects on the rock acoustic properties including the magnitude of anisotropy, and to use these observations to validate theory.

S-wave anisotropy was measured for the different fluids and fracture directions. The core with fractures orientated at 90° to the fracture normal showed percentage shear-wave splitting equal to one hundred times the fracture density and this relationship was insensitive to fluid saturation. Sensitivity of shear waves to saturating fluid was seen using the laboratory data in the core with fractures orientated at 45° to the fracture normal when comparing the water and glycerin saturated measurements. The difference in shear-wave splitting between the two fluid saturations was quantified using the Chapman theory. Although the changes at 45° to the fracture normal were seen to be subtle, the result showed that shear-wave splitting at this angle became negative with a more viscous saturating fluid.

7.2.2 Experiment II (Chapter 5).

The second experiment set out to improve two aspects of the CNPC rocks: the realism of the rocks and seismic wavelength to fracture size ratio. A method was reported for how to manufacture novel synthetic silica cemented sandstones with a controlled fracture geometry. The method was able to produce realistic silica cemented reservoir sandstones which contained penny-shaped voids with realistic seismic P- and S-wave velocities. Four cores were made. One was unfractured and the others were orientated at 0°, 45° and 90° to the fracture normal.

The pulse-echo system was used to measure the P- and S-wave velocity and attenuation of the novel synthetic silica cemented sandstone cores with a controlled fracture geometry for air, water and

glycerin saturations. The results showed that velocity measurements between the separately made cores could not be compared with each other as the velocities did not conform to typical variations associated with transversely isotropic materials. This difference was attributed to variations in cementation and grain packing during the manufacturing stage.

Nevertheless, by comparing shear-wave splitting results from individual cores for all saturations a number of strong correlations were revealed. Initially, the unfractured core was analysed for layering anisotropy and found that at a differential pressure of 40 MPa, shear-wave splitting of less than 0.5% was measured. For the core with fractures orientated at 0° to the fracture normal, 0% shear-wave splitting was measured for all saturations. For the core with fractures at 90° to the fracture normal, shear-wave splitting of around 3% was found for all saturations. These last two observations are both in line with theory that predicts shear-wave splitting should equal $100\varepsilon_f$ and should be independent of fluid saturation. Both of these findings agree with theoretical predictions of shear-wave splitting at the respective angles to the fracture normal for a transversely isotropic medium. Interesting but unquantifiable variations of shear-wave splitting were seen in the core with fractures at 45° to the fracture normal with respect to fluid saturation.

7.2.3 Experiment III (Chapter 6).

In a bid to remove the inter-sample variations seen in the second experiment, two larger samples were made; one unfractured and the other containing a controlled fracture geometry. They were ground into octagonal prisms to allow transducers to be placed directly on the faces to give measurements in four directions relative to the layer and fracture normal in a bench-top, pulse transmission arrangement. The pulse-echo system can only measure in one direction for a single sample and therefore requires three core plugs to fully quantify the anisotropy. This

bench-top arrangement was seen as the best compromise between accuracy and the requirement for all measurements to be made on a single sample. Drawbacks to the bench-top system included loss of elevated pressure data and difficulties in maintaining saturation of samples. By using a reference material to compare the wavelets recorded from the rock, both P- & S-wave phase velocity and attenuation were measured to an adequate degree of accuracy, something previous bench-top studies of synthetic fractured rocks failed to do (e.g. Rathore *et al.* 1995).

Measurements in the fractured rock showed azimuthal variations of velocity consistent with transverse isotropy, something that the samples from the second experiment did not. Shear-wave splitting was measured at each angle by rotating the shear-wave transducer so that it was polarised parallel (S1) and perpendicular (S2) to the fracture strike. Shear-wave splitting was seen to vary at all angles to the fracture normal and found to be sensitive to fluid saturation at 45° to the fracture normal. At 0° to the fracture normal, shear-wave splitting was found to be approximately 0% for all saturations and at 90° to the fracture normal, shear-wave splitting was found to approximately equal the layering anisotropy plus the fracture density. At 45° to the fracture normal, particular attention was paid to the differences between the water and glycerin saturations for a direct comparison with the observations seen in the first experiment. The observations in the third experiment also observed fluid-dependent shear-wave splitting at this angle and also showed a polarisation flip of shear-wave splitting with an increase of fluid viscosity. Modelling results showed, for the aspect ratios of the fractures within the samples, that both viscosity and bulk modulus were responsible for the observed changes of shear-wave splitting.

Using the best fitting model for the water saturated sample, ε, δ and γ were modelled for air and glycerin saturation and compared to the measured data. Modelling of these Thomsen parameters found that the subtle difference between water and glycerin for ε and δ could be

modelled. More interestingly, air saturation was predicted and measured to be much higher than both water and glycerin for these parameters. γ was predicted to be independent of fluid saturation and matched the measured data very well showing that the layering anisotropy plus fracture density could explain the overall S-wave anisotropy found in the fractured sample.

7.3 Discussion and conclusions.

It can be seen that the third experiment made a significant step forwards in model validation in comparison to the first experiment. For example, the full anisotropic tensor was measured for both the unfractured and fractured rocks and for three saturation states. It is interesting to note that the values of τ_m for both experiments were found independently and are both of similar magnitude, although τ_m for the third experiment is larger than for the first. Since the grains making up the rock are larger in size, one might expect any grain contact microcracks to be similarly larger than in the first experiment (CNPC rocks) giving rise to lower relaxation times; this is consistent with theory and acts as a small reality check.

Another thing common to the modelling in both the first and third experiment is the inability to model the velocities associated with the glycerin saturation even when using squirt flow modelling, which predicts that velocity should increase with increasing fluid viscosity. For this reason it appears a frame stiffening effect is occurring for the glycerin saturated measurements. Such an effect was observed on glycerin saturated sandstones in the laboratory by Marketos and Best (2010) with reference to the BISQ squirt flow model (Dvorkin and Nur 1993; Dvorkin et al 1994). Nevertheless, variations of anisotropy with respect to fluid viscosity and bulk modulus can still be assessed.

The suitability of the Chapman model to analyse this type of dataset is key. For example, the Hudson (1981) and Thomsen (1995) models are frequency independent and will not predict variations of

shear-wave splitting with fracture direction and fluid type. The Hudson (1981) model was extended to the full frequency range by Hudson *et al*. (1996) where the normal traction on a fracture in the first order corrections was frequency dependent. However the model reduces to the Hudson (1981) model at zero frequency in contradiction with Gassmann's formulae. Another unsatisfactory and questionable physical aspect with the extension was that fluid was allowed to flow between the cracks along mechanically "invisible" pathways. This becomes particularly apparent at the seismic wavelengths of a field survey as the model predicts fluid flow of tens of metres over these "invisible" pathways.

The laboratory measurements have provided validation for particular aspects of the Chapman model. One aspect is the shear-wave splitting variations with fluid at non-vertical seismic incidence observed in all three experiments. Implications and the results of the model predictions and laboratory measurements could be used directly for oil-water discrimination in fractured reservoirs. For example if the polarisation flip in shear-wave splitting could be seen between water and oil bearing layers, it has the potential to be used as an analytical tool for fluid determination using multicomponent field seismic data.

This laboratory study has confirmed the robust relationships used by the seismic exploration industry to interpret fracture properties: maximum P-wave velocity, minimum attenuation and maximum shear-wave splitting in the fracture strike direction. Measurements from the high pressure pulse-echo system also showed that shear-wave splitting was $100\varepsilon_f$ and independent of fluid saturation for wave propagation at 90° to the fracture normal at high confining pressures.

Perhaps one of the most important findings of the work is evidence that it is possible to infer more than information regarding the fracture compliance from seismic data. The theory of Chapman (2003) relates the anisotropic response of the rock based on the physical size of the fractures and saturating fluid properties. This model was successfully applied to the data of the first and third experiment and used to model

the anisotropic response of the rock based directly on the size of the fractures. In all three experiments it was possible to relate the fracture density, calculated through physically measured parameters to shear-wave splitting. These findings are in direct contradiction with beliefs that only fracture compliance can be derived and interpreted from seismic data and provide evidence that accounting for the physical properties of the fractures within models is a key aspect to consider.

The experiments carried out in this thesis open the door for a series of further laboratory validation experiments. It is clear that the manufacturing method for the rocks allows any number of fracture distributions to be created. However, the ultimate result would be to be able to produce rocks without background layering anisotropy that can be cored in three directions and measured in the pulse-echo system. A study of this nature could look at not just fracture and fluid effects but also pressure effects. It was shown by Best *et al.* (2007) that the response of attenuation anisotropy to pressure was much more sensitive than velocity anisotropy. With this in mind, it would be particularly useful to measure frequency-dependent velocity related fluid effects with changes of attenuation in a multicomponent time-lapse field seismic survey to determine both fluid and pressure changes in reservoirs.

Another important future advance would be the design of laboratory experiments capable of obtaining accurate elastic wave anisotropy data for wavelengths much greater than the fracture size, in order to isolate the true poro-visco-elastic phenomena modelled by Chapman (2003) in the absence of wave scattering effects. On the other hand, one could take the present study results as somewhat realistic to the field case where there may always be some geological features that are larger than the seismic wavelength (e.g., fracture sets occur on a wide range of scales) and hence lead to scattering. Probably the most significant finding of this laboratory study is that despite strong scattering effects, many of the poro-visco-elastic effects on elastic wave anisotropy that are predicted by the theory do in fact predominate and

are readily observable. This is a most encouraging prospect for seismic exploration of fractured reservoirs.

Chapter 8

References.

Aki K. and Richards P. G. 1980. *Quantitative seismology: Theory and methods.* W.H. Freeman and Co., San Francisco.

Alford R. M. Year. Shear data in the presence of azimuthal anisotropy. Conference Shear data in the presence of azimuthal anisotropy, 56th Annual SEG Meeting, Expanded Abstracts, 476-479.

Ass'ad J. M. 2005. The effect of orthorhombic anisotropy and its implication for oil recovery and reservoir exploitation. *Geophysical Prospecting* **53**, 121-129.

Ass'ad J. M., Tatham R. H. and McDonald J. A. 1992. A physical model study of microcrack-induced anisotropy. *Geophysics* **57**, 1562-1570.

Backus G. 1962. Long-wave elastic anisotropy produced by horizontal layering. *Journal Geophysical Research* **67**, 4427-4440.

Bahorich M. and Farmer S. 1995. 3-D Seismic discontinuity for faults and stratigraphic features. *First Break* **14**, 1053–1058.

Barlow R. J. 1989. *Statistics: A guide to the Use of Statistical Methods in the Physical Sciences.* John Wiley & Sons.

Batzle M., Han D.-H. and Hofmann R. 2006. Fluid mobility and frequency-dependent seismic velocity - direct measurements. *Geophysics* **71**, N1-N9.

Benson G. C. and Kiyohara O. 1974. Tabulation of some integral functions describing diffration effects in the ultrasonic field of a circular piston source. *Acoustical Society of America* **55**, 184-185.

Berryman J., G. 1979. Long-wave elastic anisotropy in transversley isotropic media. *Geophysics* **44**, 896-917.

Best A. and McCann C. 1995. Seismic attenuation and pore-fluid viscosity in clay-rich reservoir sandstones. *Geophysics* **60**, 1386-1397.

Best A. I. 1992. *The prediction of the reservoir properties of sedimentary rocks from seismic measurements*. Ph.D. thesis, University of Reading.

Best A. I., Sothcott J. and McCann C. 2007. A laboratory study of seismic velocity and attenuation anisotropy in near-surface sedimentary rocks. *Geophysical Prospecting* **55**, 609-625.

Biot M. A. 1956. Theory of propagation of elastic waves in fluid-saturated porous solid, I. Low frequency range, II. Higher frequency range. *Journal of the Acoustical Society of America* **28**, 168-191.

Block L. V., Cheng C. H., Fehler C. and Scott Phillips W. 1994. Seismic imaging using microearthquakes induced by hydraulic fracturing. *Geophysics* **59**, 102-112.

Brown R. and Korringa J. 1975. On the dependence of the elastic properties of a porous rock on the compressibility of the pore fluid. *Geophysics* **40**, 608-616.

Chapman M. 2001. *Modelling the wide-band laboratory response of rock samples to fluid and pressure changes*. Ph.D. thesis, University of Edinburgh.

Chapman M. 2003. Frequency-dependent anisotropy due to meso-scale fractures in the presence of equant porosity. *Geophysical Prospecting* **51**, 369-379.

Chapman M., Maultzsch S., Liu E. and Li X.-Y. 2003. The effect of fluid saturation in an anisotropic multi-scale equant porosity model. *Journal of Applied Geophysics* **54**, 191-202.

Chapman M., Zatsepin S. and Crampin S. 2002. Derivation of a microstructural poroelastic model. *Geophysical Journal International* **151**, 427-451.

Clarke R. A., Benson P. M. and Carter A. J. 2009. Anisotropic P-wave attenuation measured from a multi-azimuth surface seismic reflection survey. *Geophysical Prospecting* **57**, 835-845.

Crampin S. 1981. A review of wave motion in anisotropic and cracked elastic-media. *Wave Motion* **3**, 343-391.

Crampin S. 1984. Effective anisotropic elastic-constants for wave propagation through cracked solids. *Geophysical Journal of the Royal Astronomical Society* **76**, 135-145.

Crampin S. 1985. Evaluation of anisotropy by shear-wave splitting. *Geophysics* **50**, 142-152.

Crampin S. 1986. Anisotropy and transverse isotropy. *Geophysical Prospecting* **34**, 94-99.

Crampin S. and Peacock S. 2005. A review of shear-wave splitting in the compliant crack-critical anisotropic Earth. *Wave Motion* **41**, 59-77.

Dellinger J. and Vernik L. 1994. Do traveltimes in pulse-transmission experiments yield anisotropic group or phase velocities? *Geophysics* **59**, 1774-1779.

Dvorkin J., Mavko G. and Nur A. 1995. Squirt flow in fully saturated rocks. *Geophysics* **60**, 97-107.

Dvorkin J. and Nur A. 1993. Dynamic poroelasticity: A unified model with the squirt and the Biot mechanisms. *Geophysics* **58**, 524-533.

Ellis M. 2008. *Joint seismic and electrical measurements of gas hydrates in continental margin sediments*. University of Southampton.

Endres A. and Knight R. 1997. Incorporating pore geometry and fluid pressure communication into modeling the elastic behavior of porous rocks. *Geophysics* **62**, 106-117.

Eshelby J. D. 1957. The Determination of the Elastic Field of an Ellipsoidal Inclusion, and Related Problems. *Proceedings of the Royal Society of London. Series A, Mathematical and Physical Sciences* **241**, 376-396.

Gao D. 2011. Latest developments in seismic texture analysis for subsurface structure, facies, and reservoir characterization. *Geophysics* **76**, W1-W13.

Gassman F. 1951. Über die Elastizität pröser Medien. *Vier. der Natur. Gesellschaft in Zürich* **96**, 1-23.

Gray D., Head K., Lahr M., Roberts G. and Ouenes A. 2002. Recent advances in determination of fracture strike and crack density from P-wave seismic data. *The Leading Edge* **21**, 280-285.

Gurevich B. 2003. Elastic properties of saturated porous rocks with aligned fractures. *Journal of Applied Geophysics* **54**, 203-218.

Gurevich B., Makarynska D., Bastos de Paula O. and Pervukhina M. 2010. A simple model for squirt-flow disperaion and attenuation in fluid-saturated graunular rocks. *Geophysics* **75**, 109-120.

Hall S. and Kendall J.-M. 2003. Fracture characterization at Valhall: Application of P-wave amplitude variation with offset and azimuth (AVOA) analysis to a 3D ocean-bottom data set. *Geophysics* **68**, 1150-1160.

Halvorsen C. and Hurst A. 1990. *Principles, practise and applications of laboratory minipermeametry.*

Han D.-H., Nur A. and Morgan D. 1986. Effects of porosity and clay content on wave velocities in sandstones. *Geophysics* **51**, 2093-2107.

Helmut H., Weldes K. and Lange R. 1969. Properties of soluble silicates. *Industrial & Engineering Chemistry* **61**, 29-44.

Hess H. 1964. Seismic anisotropy of the uppermost mantle under oceans. *Nature* **203**, 629-631.

Hoenig A. 1979. Elastic moduli of a non-randomly cracked body. *International Journal of Solids and Structures* **15**, 137-154.

Horne S. 2003. Fracture characterization from walkaround VSPs. *Geophysical Prospecting* **51**, 493-499.

Hudson J., Liu E. and Crampin S. 1996. The mechanical properties of materials with interconnected cracks and pores. *Geophysical Journal International* **124**, 105-112.

Hudson J., Pointer T. and Liu E. 2001. Effective-medium theories for fluid-saturated materials with aligned cracks. *Geophysical Prospecting* **49**, 509-522.

Hudson J. A. 1981. Wave speeds and attenuation of elastic waves in material containing cracks. *Geophysical Journal of the Royal Astronomical Society* **64**, 133-150.

Jones T. 1986. Pore fluids and frequency-dependent wave propagation. *Geophysics* **10**, 1939-1953.

Jones T. and Nur A. 1983. Velocity and attenuation in sandstone at elevated temperatures and pressures. *Geophysical Research Letters* **10**, 140-143.

Kaye G. W. C. and Laby T. H. 1995. *Tables of phsyical and chemical constants.* Longman.

King M. S. 1966. Wave velocities in rocks as a function of changes in overburden pressure and pore fluid saturants. *Geophysics* **31**, 50-73.

Klimentos T. and McCann C. 1990. Relationships among compressional wave attenuation, porosity, clay content and permeability in sandstones. *Geophysics* **55**, 998-1014.

Liu E., Chapman M., Zhang Z. and Queen J. H. 2006. Frequency-dependent anisotropy: Effects of multiple fracture sets on shear-wave polaizations. *Wave Motion* **44**, 44-57.

Liu E., Crampin S., Queen J. H. and Rizer W. D. 1993. Velocity and attenuation anisotropy caused by microcracks and microfractures in a multiazimuth reverse VSP. *Canadian Journal of Exploration Geophysics* **29**, 177-188.

Liu E., Hudson J. and Pointer T. 2000. Equivalent medium representation of fractured rock. *Journal Geophysical Research* **105**, 2981-3000.

Liu E., Queen J. H., Li X. Y., Chapman M., Maultzsch S., Lynn H. B. and Chesnokov E. M. 2003. Observation and analysis of frequency-dependent anisotropy from a multicomponent VSP at Bluebell-Altamont Field, Utah. *Journal of Applied Geophysics* **54**, 319-333.

Lynn H. B., Beckham W. E., Simon K. M., Bates C. R., Layman M. and Jones M. 1999. P-wave and S-wave azimuthal anisotropy at a naturally fractured gas reservoir, Bluebell Altamont field, Utah. *Geophysics* **64**, 1312-1328.

Lynn H. B. and Thomsen L. Year. Reflection shear-wave data along the principal axes of azimuthal anisotropy. Conference Reflection shear-wave data along the principal axes of azimuthal anisotropy, 56th Annual SEG Meeting, Expanded Abstracts, 474-476.

Marketos G. and Best A. I. 2010. Application of the BISQ model to clay squirt flow in reservoir sandstones. *Journal of Geophysical Research* **115**, B06209, doi:10.1029/2009JB006495.

Maultzsch S., Chapman M., Liu E. and Li X. Y. 2003. Modelling frequency-dependent seismic anisotropy in fluid-saturated rock with aligned fractures: implications of fracture size estimation

from anisotropic measurements. *Geophysical Prospecting* **51**, 381-392.

Maultzsch S., Chapman M., Liu E. and Li X. Y. 2007. Modelling and analysis of attenuation anisotropy in multi-azimuth VSP data from the Clair field. *Geophysical Prospecting* **55**, 627-642.

Maultzsch S., Nawab R., Yuh S., Idrees M. and Frignet B. 2009. An integrated multi-azimuth VSP survey for fracture characterization in the vicinity of a well. *Geophysical Prospecting* **57**, 263-274.

Mavko G. and Jizba D. 1991. Estimating grain-scale fluid effects on velocity dispersion in rocks. *Geophysics* 1940-1949.

Mavko G., Mukerji T. and Dvorkin J. 1998. *The Rock Physics Handbook.* Cambdridge University Press, Cambridge, UK.

Mavko G. and Murkerji T. 1995. Seismic pore space compressibility and Gassmann's relation. *Geophysics* **60**, 1743-1749.

Mavko G. and Nur A. 1975. Melt squirt in the Asthenosphere. *Journal of Geophysical Research* **80**, 1444-1448.

McCann C. and Sothcott J. 1992. Laboratory measurements of the seismic properties of sedimentary rocks. *Geological applications of wireline logs* **2**, 285-297.

Meadows M. A. and Winterstein D. F. 1994. Seismic detection of a hydraulic fracture from shear-wave VSP dat at Lost Hills Field California. *Geophysics* **59**, 11-26.

Müller T. M., Gurevich B. and Lebedev M. 2010. Seismic wave attenuation and dispersion resulting from wave-induced flow in porous rocks - A review. *Geophysics* **75**, 147-164.

Murphy W. 1984. Acoustic measures of partial gas saturation in tight sandstones. *Journal of Geophysical Research* **89**, 11549-11559.

Murphy W. 1985. Sonic and ultrasonic velocities: theory versus experiment. *Geophysical Research Letters* **12**, 85-88.

Murphy W., Winkler K. and Kleinberg R. L. 1986. Acoustic relaxation in sedimentary rocks: Dependence on grain contacts and fluid saturation. *Geophysics* **51**, 757-766.

Papadakis E. P. 1972. Ultrasonic diffraction loss and phase change for broad-band pulses. *Acoustical Society of America* **52**, 847-849.

Papadakis E. P., Fowler K. A. and Lynnworth L. C. 1973. Ultrasonic attenuation by spectrum analysis of pulses in buffer rods: Method and diffraction corrections. *Acoustical Society of America* **53**, 1336-1343.

Peacock S., McCann C., Sothcott J. and Astin T. R. 1994a. Experimental measurements of seismic attenuation in microfractured sedimentary rock. *Geophysics* **59**, 1342-1351.

Peacock S., McCann C., Sothcott J. and Astin T. R. 1994b. Seismic velocities in fracture rocks:as experimental verification of Hudson's theory. *Geophysical Prospecting* **42**, 27-80.

Plona T. 1980. Observation of a second bulk compressional wave in a porous medium at ultrasonic frequencies. *Applied Physics Letters* **36**, 259-261.

Pride S., R, Berryman J., G and Harris J., M. 2004. Seismic attenuation due to wave-induced flow. *Journal Geophysical Research* **109**, 1-19.

Qian Z., Chapman M., Li X. Y., Dai H. C., Liu E., Zhang Y. and Wang Y. 2007. Use of multicomponent seismic data for oil-water discrimination in fractured reservoirs. *The Leading Edge* **26**, 1176-1184.

Rathore J. S., Fjaer E., Holt R. M. and Renlie L. 1995. P- and S- wave anisotropy of a synthetic sandstone with controlled crack geometry. *Geophysical Prospecting* **43**, 711-728.

Rüger A. 1997. P-wave reflection coefficients for transversely isotropic models with vertical and horizontal axis of symmetry. *Geophysics* **62**, 713-722.

Rüger A. 2002. *Reflection coefficients and azimuthal AVO analysis in anisotropic media.* Society of Exploration Geophysicists, Tulsa, OK.

Sams M. S., Neep J. P., Worthington M. H. and King M., S. 1997. The measurement of velocity dispersion and frequency-dependent intrinsic attenuation in sedimentary rocks. *Geophysics* **62**, 1456-1464.

Sayers C. 2009. Seismic characterization of reservoirs containing multiple fracture sets. *Geophysical Prospecting* **57**, 187-192.

Sayers C. and Kachanov M. 1995. Microcrack-induced elastic wave anisotropy of brittle rocks. *Journal Geophysical Research* **100**, 4149-4159.

Schoenberg M. 1980. Elastic wave beheavior across linear slip interfaces. *Journal of the Acoustical Society of America* **68**, 1516-1521.

Schoenberg M. and Protázio J. 1992. 'Zoeppritz' rationalized and generalized to anisotropy. *Journal of Seismic Exploration* **1**, 125-144.

Schoenberg M. and Sayers C. M. 1995. Seismic anisotropy of fractured rock. *Geophysics* **60**, 204-211.

Sheppard W., L. 1986. *Corrosion and chemical resistant masonry materials handbook.* Noyes Publications.

Sheriff R. and Geldart L. 1999. *Exploration Seismology.* Cambridge University Press.

Sherlock D. and Siggins A. 2004. The development of synthetic CIPS sandstones for geophysical research. 74th Annual SEG Meeting, Denver, Colorado, USA, Expanded Abstracts, 1642-1646.

Smith T. M., Sondergeld C. H. and Rai C. S. 2003. Gassmann fluid substituations: A tutorial. *Geophysics* **68**, 430-440.

Sothcott J., McCann C. and O'Hara S. G. 2000. The influcence of two different pore fluids on the acousitc properties of reservoir sandstones at sonic and ultrasonic frequencies. *70th SEG Meeting*, Calgary, Canada, Expanded abstracts, 1883-1886.

Thomsen L. 1986. Weak elastic anisotropy. *Geophysics* **51**, 1954-1966.

Thomsen L. 1993. *Weak anisotropic reflections, Offset dependent reflectivity - Theory and practise of AVO analysis.* Society of Exploration Geophysics, Tulsa, Oklahoma.

Thomsen L. 1995. Elastic anisotropy due to aligned cracks in porous rock. *Geophysical Prospecting* **43**, 805-829.

Thomsen L. 2001. Seismic Anisotropy. *Geophysics* **66**, 40-41.

Tillotson P., Chapman M., Best A. I., Sothcott J., McCann C., Shangxu W. and Li X. Y. 2011. Observations of fluid-dependent shear-wave splitting in synthetic porous rocks with aligned penny-shaped fractures. *Geophysical Prospecting* **59**, 111-119, doi: 10.1111/j.1365-2478.2010.00903.x.

Tod S. R., Taylor B., Johnston R. and Allen T. 2007. Fracture prediction from wide-azimuth land seismic data in SE Algeria. *The Leading Edge* **26**, 1154-1160.

Tsvankin I. 2001. *Seismic signatures and analysis of reflection data in anisotropic media.* Handbook of geophysical exploration. Seismic Exploration. Volume 29.

Tsvankin I., Gaiser J., Grechkha V., van der Baa M. and Thomsen L. 2010. Seismic anisotropy in exploration and reservoir characterization: An overview. *Geophysics* **75**, 15-29.

van der Kolk C. M., Guest W. S. and Potters J. H. H. M. 2001. The 3D shear experiment over the Natih field in Oman: the effect of fracture-filling fluids on shear propagation. *Geophysical Prospecting* **49**, 179-197.

Wang Z. 2001. Fundamentals of seismic rock physics. *Geophysics* **66**, 398-412.

Wang Z. 2002. Seismic anisotropy in sedimentary rocks, part 1: A single-plug laboratory method. *Geophysics* **67**, 1415-1422.

Willis H. A., Rethford G. L. and Bielanski. Year. Azimithal anisotropy: Occurrence and effect on shear-wave data quality. Conference

Azimithal anisotropy: Occurrence and effect on shear-wave data quality, 56th Annual SEG Meeting, Expanded Abstracts, 479-481.

Willis M. E., Burns D. R., Rama R., Minsley B., Nafi Toksöz M. and Vetri L. 2006. Spatial orientation and distribution of reservoir fractures from scattered seismic energy. *Geophysics* **71**, 43-51.

Winkler K. 1985. Dispersion analysis of velocity and attenuation and Bera Sandstone. *Journal of Geophysical Research* **90**, 6793-6800.

Winkler K. 1986. Estimates of velocity dispersion between seismic and ultrasonic frequencies. *Geophysics* **51**, 183-189.

Winkler K. and Plona T. J. 1982. Techniques for measuring ultrasonic velocity and attenuation spectra in rocks under pressure. *Journal of Geophysical Research* **87**, 10776-10780.

Xiyuan C., Tian-ji X., Xian-gui L., Tinnin J. and Hallin J. 2009. Research and application of gas detection techniques using full-wave attributes in southwest China. *First Break* **27**, 91-96.

Zhu Y. and Tsvankin I. 2006. Plane-wave propagation in attenuative transversely isotropic media. *Geophysics* **71**, T17-T30.

Zoeppritz K. 1919. On the reflection and propagation of seismic waves. *Göttinger Nachrichten* **I**, 66-84.

Appendix A

Anisotropic reflection coefficient.

The partition, reflection and transmission of plane waves at boundaries can be described for an isotropic/isotropic case using the Zoeppritz (1919) equations and reduces to equation 4.6 in Chapter 4 at normal incidence (such as in the pulse-echo system for isotropic samples). This formula is sufficient for transversely isotropic materials in the symmetry planes (e.g. 0° and 90°) since the waves suffer no lateral translation. However, at angles away from this (e.g. the 45° sample) the transversely isotropic rock base reflection interface with the isotropic buffer rod will cause an anisotropic reflection (Figure A.1).

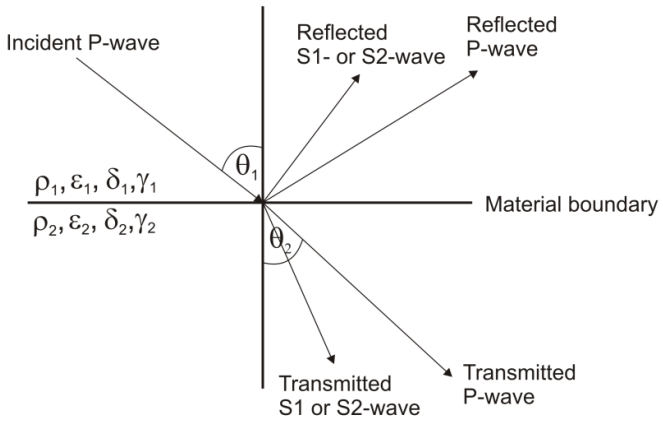

Figure A.1: Reflected and transmitted seismic waves caused by a P-wave incident at a boundary between two materials with different anisotropic properties (adapted from Mavko *et al.* (1998)).

Schoenberg and Protázio (1992) gave solutions of the Zoeppritz equations in anisotropic media which can be used to calculated the anisotropic reflection coefficient with symmetry up to monoclinic.

In order to calculate the anisotropic reflection coefficient the full elastic stiffness tensor is required. For transversely isotropic materials the tensor has the form

$$\begin{bmatrix} c_{11} & c_{12} & c_{13} & 0 & 0 & 0 \\ c_{12} & c_{11} & c_{13} & 0 & 0 & 0 \\ c_{13} & c_{13} & c_{13} & 0 & 0 & 0 \\ 0 & 0 & 0 & c_{44} & 0 & 0 \\ 0 & 0 & 0 & 0 & c_{44} & 0 \\ 0 & 0 & 0 & 0 & 0 & c_{66} \end{bmatrix}.$$

This can only be calculated for transversely isotropic materials by measuring velocity in three directions; 0°, 45° (or some other intermediate angle) and 90° to the symmetry axis. The five components of the stiffness tensor can be measured from 5 velocity measurements (Wang 2002); $\mathrm{V_P}(90°)$, $\mathrm{V_P}(0°)$, $\mathrm{V_P}(45°)$, $\mathrm{S1}(90°)$ and $\mathrm{S1}(0°)$ where,

$$c_{11} = \rho \mathrm{V_P}(90°)\,,$$
$$c_{12} = c_{11} - 2\rho \mathrm{S1}^2(90°)\,,$$
$$c_{33} = \rho \mathrm{V_P}^2(0°)\,,$$
$$c_{44} = \rho \mathrm{S1}^2(0°)\,,$$
$$c_{13} = -c_{44} + \sqrt{4\rho \mathrm{V_P}(45°)^4 - 2\rho \mathrm{V_P}(45°)^2(c_{11} + c_{33} + 2c_{44}) + (c_{11} + c_{44})(c_{33} + c_{44})}\,,$$
$$c_{66} = \frac{1}{2}(c_{11} - c_{12})\,.$$

Exact reflection coefficients can be simplified from the Schoenberg and Protázio (1992) form in the limit of weak transverse isotropy i.e. that ε and δ << 1. The parameters ε and δ are two of Thomsen's anisotropy parameters given by (Thomsen 1986). Thomsen's shear-wave anisotropy parameter, γ, is also required for the S1-wave reflection coefficient. These anisotropy parameters are given by:

$$\varepsilon = \frac{c_{11} - c_{33}}{2c_{33}},$$

$$\delta = \frac{(c_{13} + c_{44})^2 - (c_{33} - c_{44})^2}{2c_{33}(c_{33} - c_{44})},$$

$$\gamma = \frac{c_{66} - c_{44}}{2c_{44}}.$$

The reflection coefficients are described by Thomsen (1993) and modified by Rüger (1997) and are of the form (Tsvankin 2001):

$$R(\theta) = R_{iso}(\theta) + R_{aniso}(\theta)\,, \tag{A.1}$$

where $R_{iso}(\theta)$ is the reflection coefficient in the reference isotropic medium ($\varepsilon = 0$, $\delta = 0$) given by e.g. Aki and Richards (1980). $R_{aniso}(\theta)$ is the contribution of the anisotropy. The parameter θ represents the incidence angle, or for our experiments the angle to the fracture normal.

For P-waves, $R_{aniso,P}(\theta)$ is given by (Rüger 1997):

$$R_{aniso,P}(\theta) = \frac{1}{2}(\delta_2 - \delta_1)\sin^2\theta + \frac{1}{2}(\varepsilon_2 - \varepsilon_1)\sin^2\theta\tan^2\theta\,. \tag{A.2}$$

Subscripts 1 and 2 refer to the material above and below the interface (see Figure A.1).

For S1-waves, $R_{aniso,S1}(\theta)$ is given by Rüger (2002):

$$R_{aniso,S1}(\theta) = \frac{1}{2}\left(\gamma_2 - \gamma_1\right)\tan^2\theta\,. \tag{A.3}$$

Rüger (2002) also shows that for S2-waves, $R_{aniso,S2}(\theta)$ is given by:

$$R_{aniso,S2}(\theta) = \frac{1}{2}\frac{\overline{V}_{P0}^2}{\overline{V}_{S0}^2}[(\varepsilon_2 - \delta_2) - (\varepsilon_1 - \delta_1)]\sin^2\theta\,, \qquad \text{(A.4)}$$

where $\overline{V}_{P0}^2$ and $\overline{V}_{S0}^2$ are the average velocities above and below the reflector.

It can be seen in the pulse-echo system that measuring samples with fractures at an angle between 0° and 90° to the fracture normal will lead to an anisotropic base reflection (see Figure 4.1). Seismic waves will be travelling through a transversely isotropic rock and the reflection will come from the interface with the isotropic buffer rod. For this reason, equations A1.3 could be used to correct the reflection coefficient used in equation 4.5 (Chapter 4). Hence, the intrinsic attenuation coefficient can be calculated correctly. However, without P-wave velocity being measured at 0° to the fracture normal, the full tensor cannot be calculated since parameters ε and δ cannot be determined.

Appendix B

Publications.

Tillotson P., Chapman M., Best A. I., Sothcott J., McCann C., Shangxu W. and Li X. Y. 2011. Observations of fluid-dependent shear-wave splitting in synthetic porous rocks with aligned penny-shaped fractures. *Geophysical Prospecting* **59**, 111-119, doi: 10.1111/j.1365-2478.2010.00903.x.

Geophysical Prospecting

EAGE EUROPEAN ASSOCIATION OF GEOSCIENTISTS & ENGINEERS

Geophysical Prospecting, 2011, **59**, 111–119 doi: 10.1111/j.1365-2478.2010.00903.x

Observations of fluid-dependent shear-wave splitting in synthetic porous rocks with aligned penny-shaped fractures‡

Philip Tillotson[1]*, Mark Chapman[2§], Angus Ian Best[1], Jeremy Sothcott[1], Clive McCann[1], Wang Shangxu[3] and Xiang-Yang Li[2,4]

[1]*National Oceanography Centre, University of Southampton, Waterfront Campus, European Way, Southampton SO14 3ZH, UK,* [2]*Edinburgh Anisotropy Project, British Geological Survey, Murchison House, West Mains Road, Edinburgh EH9 3LA, UK,* [3]*Key Laboratory of Geophysical Prospecting, CNPC, University of Petroleum, 102249 Beijing, China, and* [4]*School of Geosciences, The University of Edinburgh, Grant Institute, The King's Buildings, West Mains Road, Edinburgh, EH9 3JW, UK*

Received September 2009, revision accepted April 2010

ABSTRACT

P- and S-wave velocity and attenuation coefficients (accurate to ±0.3% and ±0.2 dB/cm, respectively) were measured in synthetic porous rocks with aligned, penny-shaped fractures using the laboratory ultrasonic pulse-echo method. Shear-wave splitting was observed by rotating the S-wave transducer and noting the maximum and minimum velocities relative to the fracture direction. A block of synthetic porous rock of fracture density 0.0201 ± 0.0068 and fracture size 3.6 ± 0.38 mm (measured from image analysis of X-ray CT scans) was sub-sampled into three 20–30 mm long, 50 mm diameter core plugs oriented at 0°, 45° and 90° to the fracture normal (transversely isotropic symmetry axis). Full waveform data were collected over the frequency range 500–1000 kHz for both water and glycerin saturated cores to observe the effect of pore fluid viscosity at 1 cP and 100 cP, respectively. The shear-wave splitting observed in the 90° core was 2.15 ± 0.02% for water saturated and 2.39 ± 0.02% for glycerin saturated, in agreement with the theory that suggests that the percentage splitting should be 100 times the fracture density and independent of the saturating fluid. In the 45° core, by contrast, splitting was 0.00 ± 0.02% for water saturation and −0.77 ± 0.02% for glycerin saturation. This dependence on fracture orientation and pore fluid viscosity is consistent with the poro-visco-elastic theory for aligned, meso-scale fractures in porous rocks. The results suggest the possible use of shear- or converted-wave data to discriminate between fluids on the basis of viscosity variations.

Key words: Fluid saturation, Shear-wave splitting, Synthetic fractures

INTRODUCTION

A major cause of seismic anisotropy within hydrocarbon reservoirs is thought to be due to micro-scale (grain-scale) and macro-scale (metre-scale) fractures (Liu *et al.* 1993). Since fractures can significantly affect the flow of reservoir fluids during hydrocarbon extraction they are important features to quantify for optimal production (Sayers 2009). One approach is to use mode converted seismic reflections (PS-waves) to

‡This paper is based on extended abstract Z020 presented at the 71st EAGE Conference & Exhibition Incorporating SPE EUROPEC 2009, 8–11 June 2009 in Amsterdam, the Netherlands.

§Now at: School of Geosciences, The University of Edinburgh, Grant Institute, The King's Buildings, West Mains Road, Edinburgh, EH9 3JW, UK

*E-mail: philip.tillotson@noc.soton.ac.uk

remotely determine fracture density and orientation through observations of shear-wave splitting. Crucially, appropriate equivalent medium theories are needed to interpret the data in terms of fracture properties. These theories relate the fracture density (ε) to the amount of anisotropy measured by the expression $\varepsilon = Na^3$ (Crampin 1981), i.e., the number of fractures per unit volume (N) multiplied by the cube of the fracture radius (a). This is believed to be a valid relationship for fracture densities up to $\varepsilon = 0.1$ (Crampin 1984). However, fracture density can be an ambiguous measurement of the fracture distribution. For example, if a rock has only a few large fractures and many smaller fractures then the same fracture density may be observed for different proportions of large to small fractures. If the observed seismic anisotropy could be attributed to micro- or macro-scale fractures then fluid flow modelling of hydrocarbon reservoirs could be improved (Maultzsch *et al.* 2003).

A more recent application of equivalent medium theories is the prediction of fluid saturation from seismic data (Qian *et al.* 2007). In the case of fractured reservoirs, frequency-dependent seismic anisotropy predicts anisotropic velocity and attenuation relationships between fracture properties (e.g., fracture size and orientation) as well as fluid properties such as viscosity. A common problem in oil exploration is the discrimination between oil and water in a reservoir using seismic reflection data. However, theoretical predictions of frequency-dependent seismic anisotropy indicate that S-waves are more sensitive to the fluid viscosity in a fractured reservoir than the commonly used P-waves (Qian *et al.* 2007). The sensitivity of shear-wave splitting to saturating fluid has already been observed on a field scale by van der Kolk, Guest and Potters (2001) and for this reason, mode converted S-wave analysis has the potential to improve fluid type predictions within fractured reservoirs.

One way to evaluate the reliability of equivalent medium theories for porous rocks is through controlled elastic wave experiments on synthetic rock samples with fractures or penny-shaped voids. This requires that velocities and attenuations can be measured with sufficient accuracy in at least three directions for transversely isotropic materials (e.g., 0°, 45°, 90° relative to the fracture normal) and that the fracture size, shape and density are known as well as properties of the saturating fluid. In a previous study, Rathore *et al.* (1995) produced synthetic porous sandstones containing aligned penny-shaped voids with a diameter of 5.5 mm. They measured ultrasonic P- and S-wave velocity at 100 kHz on dry and water saturated samples as a function of wave propagation direction. The data were compared to the model predictions of Hudson (1981) and Thomsen (1995). Some limitations of the work included: evidence for scattering (Hudson, Pointer and Liu 2001); only two saturation states were measured (dry and water); little emphasis on attenuation; and an unrealistic rock cement (sand grains cemented with epoxy resin). Despite these limitations, their model predictions showed that the low-frequency theory could explain some of the experimental observations.

In this study velocity and attenuation were measured on synthetic porous rock samples with aligned penny-shaped voids using the ultrasonic pulse-echo system. In particular, the shear-wave splitting observations showed good agreement with the theory and are presented here. Data were collected for rocks saturated with water (viscosity 1 cP [1 cP = 10^{-3} Pa.s]) and glycerin (100 cP) and were compared to the frequency-dependent seismic anisotropy theory of Chapman (2003).

The wavelengths used were comparable to the fracture radius. Strictly speaking, the equivalent medium theory should not be applicable to this situation but we nevertheless find a number of important correlations with the theory. Notably, for wave propagation at 90° to the fracture normal, the observed values of shear-wave splitting and the theoretical predictions were about 2%, which was 100 times the fracture density (measured from the image analysis of X-ray CT data). Moreover, the theory predicts the observed angular variations of shear-wave splitting due to pore fluid viscosity changes. These laboratory results provide supporting evidence for the application of such theoretical models to the analysis of mode converted shear-wave reflections for oil-water discrimination in fractured reservoir rocks.

LABORATORY MEASUREMENTS

Rock samples

A block of synthetic porous rock with aligned penny-shaped voids (fractures) was provided by the Chinese National Petroleum Corporation's (CNPC) Key Laboratory for experimental investigation using the pulse-echo system. Three subsamples were cored at 0°, 45° and 90° to the fracture normal using a diamond drill bit; each sample had a diameter of 50 mm and a length of between 20–30 mm (see Fig. 1). Porosity, permeability, grain size and mineralogy (found to be a sodium aluminium oxide compound from XRD analysis) were measured using standard methods; X-ray CT scans were obtained for fracture size and density quantification (Fig. 2). The measured rock and fracture characteristics needed for input to the theoretical model are given in Table 1.

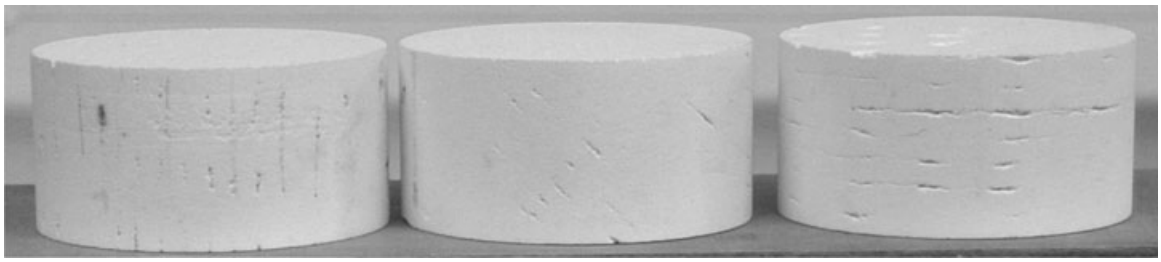

Figure 1 Synthetic rock samples (diameter 50 mm) cored at 90° (left), 45° (centre) and 0° (right) to the fracture normal from the same block. An unwanted hairline fracture is just visible in the 0° sample joining the (planned) penny-shaped fractures.

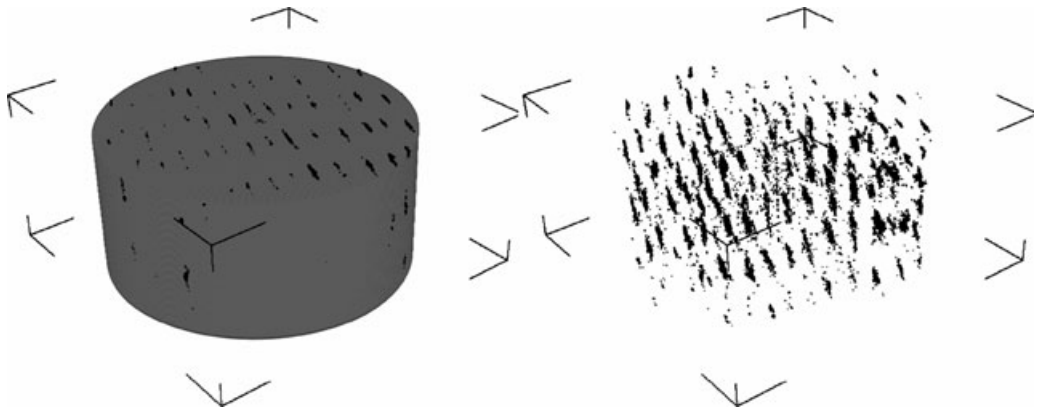

Figure 2 X-ray CT images of the synthetic 90° rock sample (diameter 50 mm) showing size, density and distribution of the penny shaped fractures.

Table 1 Model input parameters for the synthetic porous rock

Rock and fluid parameters used in this study	
P-wave velocity (V_p)	4475 ± 13 m/s
S-wave velocity (V_s)	2710 ± 8 m/s
Observation frequency (f_0)	750 kHz
Bulk density of water saturated rock (ρ)	2829 kgm^{-3}
Rock porosity (Φ_p)	29%
Pore fluid bulk modulus (water) (κ_{fwater})	2.19 GPa
Penny-shaped fractures (at 50 MPa)	
Fracture density (ε_f)	0.0201 ± 0.0068
Fracture radius (a_f)	1.8 ± 0.19 mm
Fracture aspect ratio	0.01

Experimental procedure

Elastic wave velocity and attenuation were measured on the rock samples using the ultrasonic pulse-echo method. The broadband pulses gave useable frequencies between 500–1000 kHz. Shear-wave splitting was measured by rotating the piezoelectric shear-wave transducer (while the sample was under elevated pressure) and observing the minimum and maximum velocities and their associated attenuations relative to the fracture direction (see Best, Sothcott and McCann (2007) for anisotropic measurement procedures). The rock samples were saturated with de-aired de-ionized distilled water (1 cP) and with glycerin (100 cP) using the methods described in McCann and Sothcott (1992) and measured in the pulse-echo rig at differential pressures between 10–50 MPa (differential pressure = confining pressure minus pore fluid pressure); the pore fluid pressure was kept constant at 5 MPa. The system was allowed to equilibrate for 30 minutes at each pressure before each measurement and the temperature in the laboratory was controlled at 20°C. Both P- and S-wave velocity and attenuations were corrected for diffraction effects and calibrated against aluminium and brass standards (McCann and Sothcott 1992; Best 1992) to give absolute accuracies of ±0.3% for velocity and ±0.2 dB/cm for the attenuation coefficient giving inverse quality factors (Q^{-1}) accurate to, for example, ±10% at $Q^{-1} = 0.02$ ($Q = 50$). The ultrasonic pulses reflected from the top and base interfaces of the rock were Fourier analysed for phase velocity and attenuation in the frequency range 500–1000 kHz. This is an optimized frequency range to negate beam spreading and associated edge effects that appear below 500 kHz. Meaningful results were obtained for the 45° and 90° samples only; the signals were too highly attenuated in the 0° fractured sample.

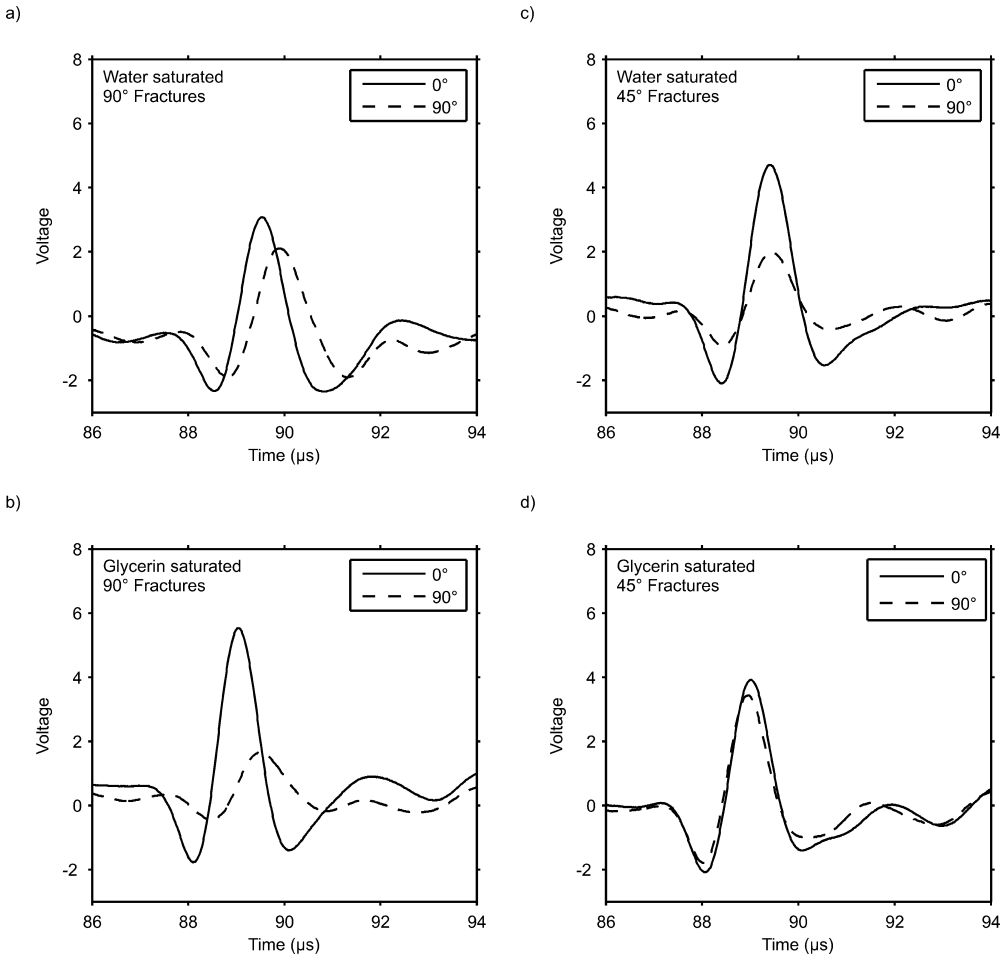

Figure 3 S-wave pulse reflections from the base of the 90° sample saturated with a) water and b) glycerin and from the 45° sample saturated with c) water and d) glycerin. S-wave polarizations relative to the fracture direction indicated in legend.

The velocities measured on these synthetic samples give P- and S-wavelengths of approximately 6 mm and 3.5 mm respectively. Since the fractures have a diameter of about 3.6 mm, very close to the shear wavelength, the inevitable scattering effects make the experimental data less than ideal for equivalent medium modelling (a similar problem to the data of Rathore *et al.* (1995)). However, even under these non-ideal experimental conditions, there were still some important aspects of the theory that agreed with the measurements.

A question that arises is whether at 45° to the fracture normal phase or group velocity is measured using the pulse-echo system. Dellinger and Vernik (1994) modelled propagation of P- and S-waves through an anisotropic medium considering the wavefronts to have a finite width when using an ultrasonic transducer with a radius between 6–10 mm. If the wavefront is travelling parallel or perpendicular to the fracture normal, a true phase velocity is measured. At 45° to the fracture normal, the wavefront can suffer a lateral translation dependent on the degree of anisotropy and propagation distance through the sample. If this translation is larger than the radius of the receiving transducer then a group velocity, not phase velocity, is measured. Using equations (1) and (2) from Dellinger and Vernik (1994) the lateral translation at 45° was calculated to be 0.31 mm for P-waves at 50 MPa (less than 10% of the radius of the receiving transducer in our experimental setup). Hence, for all wavefronts the lateral translation is an order of magnitude less than the radius of the receiving transducer and phase velocity is measured at 45°.

LABORATORY RESULTS

The S-wave pulse reflections from the base of the samples are presented in Fig. 3. For the 90° sample, significant time differences are seen between orthogonally polarized S-waves

corresponding to in-line and transverse directions relative to the aligned fractures (e.g., compare time shift between peak amplitudes of waveforms). These time delays are approximately the same for both the water (Fig. 3a) and glycerin (Fig. 3b) saturated cases. However, in the 45° sample the time delay becomes much smaller for both water and glycerin. When water saturated (Fig. 3c), the waveform for S-wave polarization at 0° to the fracture direction arrives at the same time as the arrival for 90°. However when the 45° sample is glycerin saturated (Fig. 3d) the waveform for S-wave polarization at 90° to fracture direction arrives just before that at 0°. The corresponding S-wave phase velocities are also presented in Figs 4 and 5 for a differential pressure of 50 MPa when any undesired fractures are closed leaving only the desired penny-shaped voids (some hairline fractures were seen joining the penny-shaped voids, possibly introduced as an artefact during the CNPC Key Laboratories rock manufacturing process).

Shear-wave splitting (SWS) is expressed as the parameter SWS (%) = 100 × (S1 − S2)/S1, where S1 and S2 are the parallel and perpendicular shear-wave velocities relative to the fracture direction, respectively. Significant shear-wave splitting of about 2% was observed in the 90° sample for both the water saturated (Fig. 4a) and glycerin saturated (Fig. 4b) cases. However, in the 45° sample the magnitude of shear-wave splitting is seen to change with fluid type (viscosity). Shear-wave splitting reduces to 0.00 ± 0.02% in the water saturated 45° sample in Fig. 5(a) and is −0.77 ± 0.02% in the glycerin saturated 45° sample in Fig. 5(b).

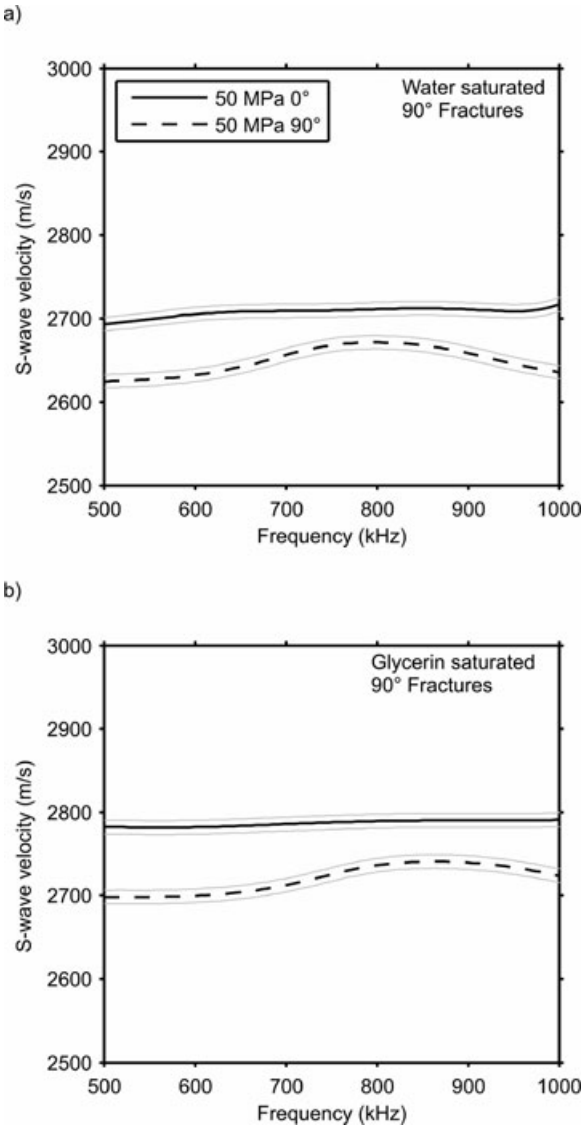

Figure 4 S-wave velocities versus measurement frequency in the 90° sample when saturated with a) water and b) glycerin. S-wave polarizations relative to the fracture direction indicated in legend.

DESCRIPTION OF THE CHAPMAN (2003) THEORY

The theory of Chapman (2003) seeks to model frequency-dependent seismic anisotropy in fractured reservoir rocks through knowledge of rock porosity, permeability, fracture density and orientation and pore fluid properties viscosity, bulk modulus and density. The model is based on a squirt flow mechanism in an anisotropic porous rock with two crack populations: randomly aligned, grain contact, ellipsoidal microcracks defined by the grain size; and aligned, mesoscale, ellipsoidal fractures that are longer than the grain size. The results of the model agree with Brown and Korringa (1975) in the low-frequency range and Hudson (1981) in the high-frequency range. In the absence of aligned mesoscale fractures the model returns to the isotropic, microcrack squirt-flow model of Chapman, Zatsepin and Crampin (2002), which was tested against laboratory data by Chapman (2001).

The stiffness tensor given by Chapman (2003), C_{ijkl}, relating the contributions from the isotropic elastic tensor (C^0, with Lamé parameters, λ and μ), C^1 (pores), C^2 (microcracks) and C^3 (fractures) multiplied by the porosity (Φ_p), microcrack density (ε_c) and fracture density (ε_f) is of the form:

$$C_{ijkl} = C^0_{ijkl} - \Phi_p C^1_{ijkl} - \varepsilon_c C^2_{ijkl} - \varepsilon_f C^3_{ijkl}. \quad (1)$$

These corrections are functions of the Lamé parameters, the fluid and fracture properties, frequency and time-scale factors

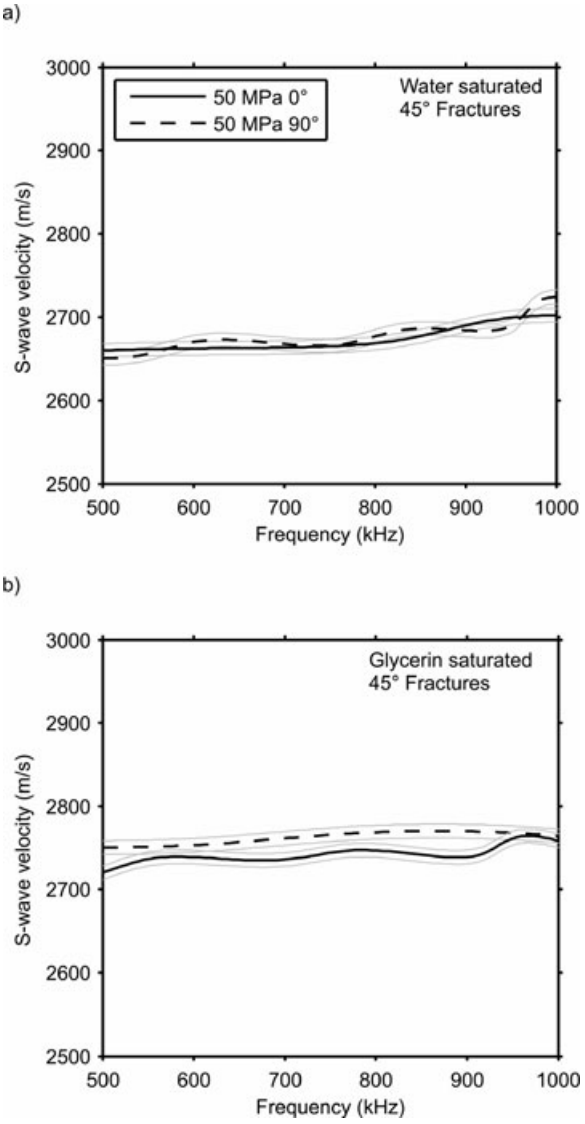

Figure 5 S-wave velocities versus measurement frequency in the 45° sample when saturated with a) water and b) glycerin. S-wave polarizations relative to the fracture direction indicated in legend.

τ_m and τ_f that relate to the squirt flow time associated with the microcracks and fractures, respectively.

To make Chapman's (2003) model more applicable to real data it was adapted by Chapman *et al*. (2003) using Lamé parameters λ^o and μ^o derived from the density (ρ) and measured velocities, V_p^o and V_s^o, of the rock. Also required is $C^0(\Lambda, M)$, to be defined such that the velocities are obtained at a specific frequency (f_0). This allows the model of Chapman (2003) to have the Lamé parameters taken from laboratory measurements for direct calibration of the model. Subsequently, we have

$$\Lambda = \lambda^o + \Phi_{c,p}(\lambda^o, \mu^o, f_0), \quad M = \mu^o + \Phi_{c,p}(\lambda^o, \mu^o, f_0), \quad (2)$$

where $\Phi_{c,p}$ refers to corrections to the elastic tensor, which are proportional to ε_c and Φ_p, with $\lambda^o = \rho(V_p^o)^2 - 2\mu^o$; $\mu^o = \rho(V_s^o)^2$.

Equation (1) can now be written as

$$\begin{aligned} C_{ijkl}(\omega) = {} & C^0_{ijkl}(\Lambda, M, \omega) - \Phi_p C^1_{ijkl}(\lambda^o, \mu^o, \omega) \\ & - \varepsilon_c C^2_{ijkl}(\lambda^o, \mu^o, \omega) \\ & - \varepsilon_f C^3_{ijkl}(\lambda^o, \mu^o, \omega). \end{aligned} \quad (3)$$

In this form the corrections for pores, microcracks and fractures that describe the frequency dependence and anisotropy of a material can be obtained from laboratory measurements on the rock (Maultzsch *et al*. 2003).

Fluid flow in the model occurs on two scales, the grain scale (associated with the microcracks and pores) and the fracture scale. The relaxation time associated with the grain scale is related to the squirt-flow frequency (τ_m) while the flow associated with the fractures results in a lower characteristic frequency or time-scale constant (τ_f) related to the size of the fractures. The time scales τ_m and τ_f are related through

$$\tau_f = \frac{a_f}{\varsigma}\tau_m, \quad (4)$$

where a_f is the fracture radius and ς is the grain size. τ_m is given by

$$\tau_m = \frac{c_v \eta(1 + K_c)}{\sigma_c \kappa \varsigma c_1}, \quad (5)$$

where η is the fluid viscosity, κ is the permeability, c_v is the volume of the individual cracks, $K_c = \sigma_c/\kappa_f$ is the inverse of the crack space compressibility, κ_f is the fluid bulk modulus, c_1 is the number of connections to other elements of pore space and $\sigma_c = \pi\mu r/[2(1 - \upsilon)]$ is the critical stress with r representing the aspect ratio of the cracks and υ is Poisson's ratio.

The model relates the frequency-dependent seismic response to fluid mobility and fracture scale lengths by allowing anisotropic velocity dispersion and attenuation (Qian *et al*. 2007).

MODEL PARAMETERIZATION AND MISFIT MINIMIZING

Table 1 shows the model parameters used to implement the theory of Chapman (2003). The only free variable that requires fitting to the data is the microcrack relaxation time τ_m; the fracture relaxation time τ_f is derived from this value

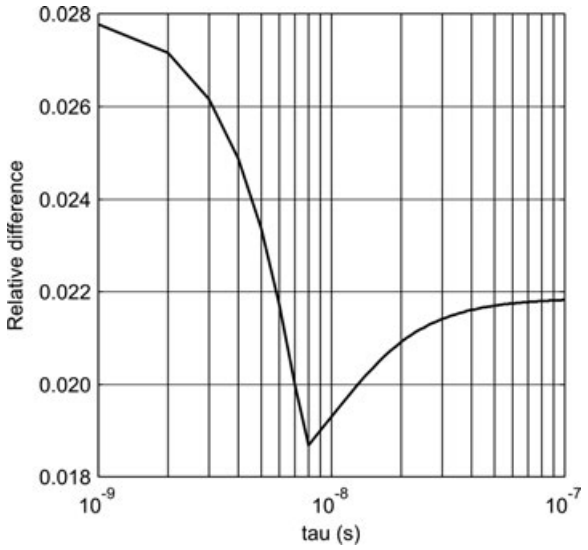

Figure 6 Relative difference between predicted and observed ultrasonic velocities at 750 kHz in the water saturated 90° and 45° samples as a function of microcrack relaxation time τ_m; note minimum located at $\tau_m = 8 \times 10^{-9}$ s.

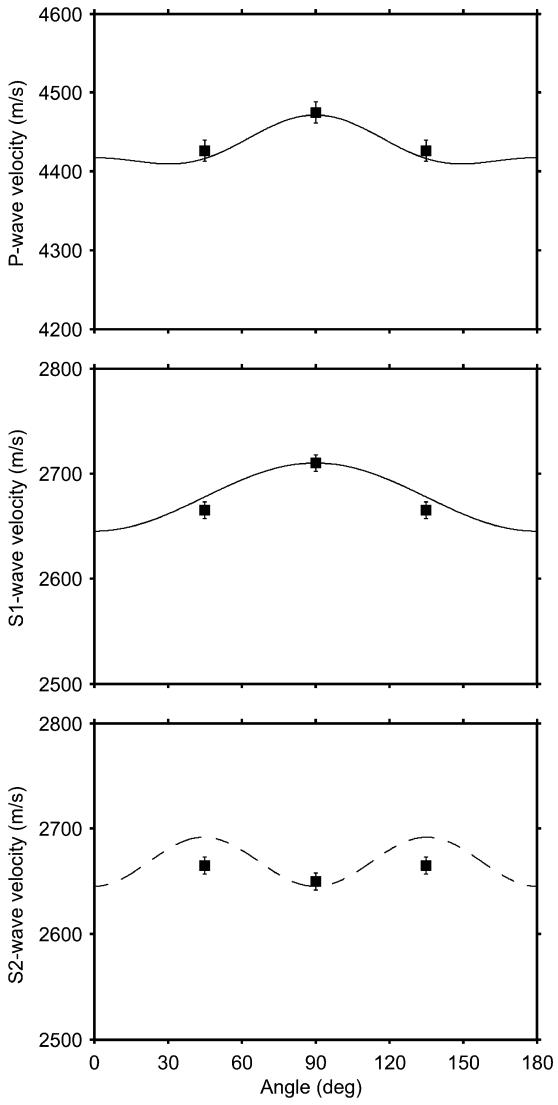

Figure 7 Results of best fitting model (lines) to the laboratory data for water saturated 45° and 90° samples at 750 kHz (squares). Note the data at 45° are repeated at 135° on the assumption of perfect symmetry in order to complete the characteristic angular dependence curves.

through model relationships incorporating the known fracture radius a_f and grain size ς (equation (4)). Chapman *et al.* (2003) showed that setting the microcrack density ε_m to zero is a good approximation for most situations of interest, hence only the fracture density ε_f is needed in Table 1. A value of τ_m was sought that minimized the misfit between the observations and model for the water saturated 45° and 90° samples. The misfit was calculated from the combined relative difference between the measured and modelled velocities at 750 kHz in the 45° and 90° samples for P- (compressional), S1- (shear-wave parallel to the fractures) and S2- (shear-wave perpendicular to the fractures) waves. This approach produced the best overall fitting model without biasing it towards any single velocity mode.

The model was found to be insensitive to the fracture aspect ratio (thickness/diameter), R, in the range $R < 0.01$. We expect that under pressure our aspect ratio will be small and therefore assume that we are in the low aspect ratio limit.

The combined misfit curve in Fig. 6 was generated from reasonable values of τ_m based on the grain size; a minimum is clearly located at $\tau_m = 8 \times 10^{-9}$ s. In fact, the curve suggests that the data best suit a high-frequency model because the differences are smaller at larger values of τ_m (i.e., higher values of relaxation frequency $= 1/\tau_m$) than at lower values of τ_m. In the high-frequency limit the fluid within the fractures become increasingly isolated from the surrounding pore space and leads to unrelaxed poro-visco-elastic behaviour.

The best fitting model velocities are compared to the actual measurements at 750 kHz in Fig. 7. The model velocities match well for P-waves but slightly overestimate the measured S1-wave values at 45° (and the duplicated results plotted at 135°) and overestimate the S2-wave values at 45° and 135°. Nevertheless, the model and experimental results are in reasonable agreement. We believe the fit is acceptable,

particularly given the deviation of the model parameters from the assumptions of the equivalent medium theory.

MODELLING OF FLUID-DEPENENT SHEAR-WAVE SPLITTING

An interesting feature of the theoretical model is the prediction of viscosity-dependent shear-wave splitting as a function of wave propagation incidence angle relative to the fracture normal. For this reason, the experiments were designed to discover whether any such dependencies could be observed in the synthetic rocks.

We repeated the measurements under glycerin saturation. There appears to be a frame stiffening effect that results in higher P- and S-wave velocities than predicted by the theory but it is nevertheless instructive to compare shear-wave splitting results to the water saturated case.

Experimental observations of shear-wave splitting from Figs 4 and 5 are again shown in Fig. 8, only this time plotted against pore fluid viscosity at a single frequency of 750 kHz. Again it is seen that, while shear-wave splitting is similar for water and glycerin in the 90° sample, shear-wave splitting is zero for water and negative for glycerin in the 45° sample. Note that the experimental errors are smaller than the symbols used for the data points.

The theory predicts that for wave propagation at 90° to the fracture normal, shear-wave splitting should be unaffected by viscosity and the relationship between fracture density and shear-wave splitting holds true regardless of viscosity. At 45° to the fracture normal, shear-wave splitting theoretically becomes negative due to increasing viscosity since the quasi-shear (S2) velocity can be higher than that of the pure-shear (S1) at this propagation angle. It is also interesting to note that although the free parameter τ_m was fitted to the water saturated data only, it also shows good agreement with the observed shear-wave splitting as a function of fracture orientation and viscosity (i.e., in the glycerin saturated samples). This provides an independent check of the correct calibration of the model to the data.

The findings here are in accordance with the theoretical predictions and field data analysis made by Qian *et al.* (2007). They successfully analysed 3D/3C data from the Shengli oilfield, detecting attenuation and velocity anomalies of PS converted-waves. These were found to be consistent with synthetic modelling results of changes in viscosity and they observed both the oil saturated zones and the water bearing zones after water injection at the location of the oil well using the field seismic data.

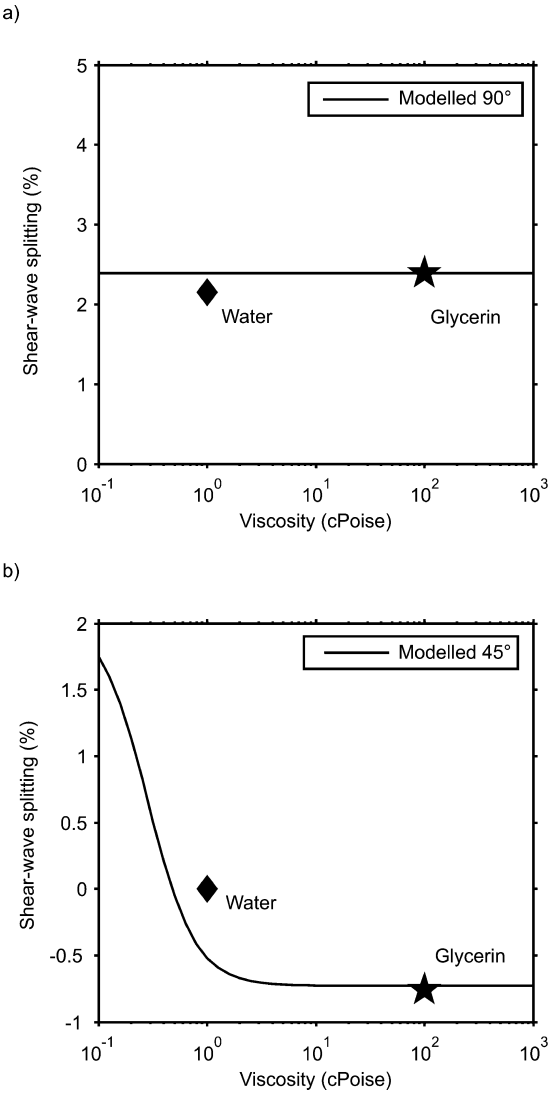

Figure 8 Comparison of model predictions of shear-wave splitting with observations at 750 kHz as a function of pore fluid viscosity a) 90° sample and b) 45° sample.

CONCLUSIONS

Laboratory observations of shear-wave splitting in synthetic rocks with penny-shaped fractures show significant changes with respect to fracture orientation and fluid viscosity relative to experimental errors. X-ray CT scanning of the rock samples allowed fracture size and density to be quantified for input to the theoretical model of Chapman (2003). Despite the experimental wavelength being close to the fracture size, the average measured magnitude of shear-wave splitting within our frequency range for waves propagating at 90° to the fracture normal is 2.15 ± 0.02% when water saturated

and 2.39 ± 0.02% when glycerine saturated. This percent shear-wave splitting in the vertical core is 100 times the fracture density measured by CT scanning, as predicted by theory (Hudson 1981). The theoretical predictions of the Chapman (2003) model, relating the magnitude and polarity of shear-wave splitting to fracture orientation and pore fluid viscosity, show reasonable agreement with the laboratory observations.

The results of this study provide evidence of fluid-dependent shear-wave splitting in fractured rocks as predicted by the theory. This gives added confidence in the use of the theory for the analysis of mode converted seismic wave reflection data for discrimination between, for example, oil and water in fractured reservoirs due to fluid viscosity differences.

ACKNOWLEDGEMENTS

The authors wish to thank the UK's Natural Environmental Research Council, Exxon-Mobil and Sinopec for providing financial support for this work. We also thank the Chinese National Petroleum Corporation for providing samples. This work forms part of the PhD studies of Philip Tillotson under a NERC-BGS PhD Studentship.

REFERENCES

Best A. 1992. *The prediction of the reservoir properties of sedimentary rocks from seismic measurements*. PhD thesis, University of Reading.

Best A., Sothcott J. and McCann C. 2007. A laboratory study of seismic velocity and attenuation anisotropy in near-surface sedimentary rocks. *Geophysical Prospecting* **55**, 609–625.

Brown R. and Korringa J. 1975. On the dependence of the elastic properties of a porous rock on the compressibility of the pore fluid. *Geophysics* **40**, 608–616.

Chapman M. 2001. *Modelling the wide-band laboratory response of rock samples to fluid and pressure changes*. PhD thesis, University of Edinburgh.

Chapman M. 2003. Frequency-dependent anisotropy due to mesoscale fractures in the presence of equant porosity. *Geophysical Prospecting* **51**, 369–379.

Chapman M., Maultzsch S., Liu E. and Li X.-Y. 2003. The effect of fluid saturation in an anisotropic multi-scale equant porosity model. *Journal of Applied Geophysics* **54**, 191–202.

Chapman M., Zatsepin S. and Crampin S. 2002. Derivation of a microstructural poroelastic model. *Geophysical Journal International* **151**, 427–451.

Crampin S. 1981. A review of wave motion in anisotropic and cracked elastic-media. *Wave Motion* **3**, 343–391.

Crampin S. 1984. Effective anisotropic elastic-constants for wave propagation through cracked solids. *Geophysical Journal of the Royal Astronomical Society* **76**, 135–145.

Dellinger J. and Vernik L. 1994. Do traveltimes in pulse-transmission experiments yield anisotropic group or phase velocities? *Geophysics* **59**, 1774–1779.

Hudson J.A. 1981. Wave speeds and attenuation of elastic waves in material containing cracks. *Geophysical Journal of the Royal Astronomical Society* **64**, 133–150.

Hudson J., Pointer T. and Liu E. 2001. Effective-medium theories for fluid-saturated materials with aligned cracks. *Geophysical Prospecting* **49**, 509–522.

Van Der Kolk C.M., Guest W.S. and Potters J.H.H.M. 2001. The 3D shear experiment over the Natih field in Oman: The effect of fracture-filling fluids on shear propagation. *Geophysical Prospecting* **49**, 179–197.

Liu E., Crampin S., Queen J.H. and Rizer W.D. 1993. Velocity and attenuation anisotropy caused by microcracks and microfractures in a multiazimuth reverse VSP. *Canadian Journal of Exploration Geophysics* **29**, 177–188.

Maultzsch S., Chapman M., Liu E. and Li X.Y. 2003. Modelling frequency-dependent seismic anisotropy in fluid-saturated rock with aligned fractures: implications of fracture size estimation from anisotropic measurements. *Geophysical Prospecting* **51**, 381–392.

McCann C. and Sothcott J. 1992. Laboratory measurements of the seismic properties of sedimentary rocks. *Geological Applications of Wireline Logs* **2**, 285–297.

Qian Z., Chapman M., Li X.Y., Dai H.C., Liu E., Zhang Y. and Wang Y. 2007. Use of multicomponent seismic data for oil-water discrimination in fractured reservoirs. *The Leading Edge* **26**, 1176–1184.

Rathore J.S., Fjaer E., Holt R.M. and Renlie L. 1995. P- and S-wave anisotropy of a synthetic sandstone with controlled crack geometry. *Geophysical Prospecting* **43**, 711–728.

Sayers C. 2009. Seismic characterization of reservoirs containing multiple fracture sets. *Geophysical Prospecting* **57**, 187–192.

Thomsen L. 1995. Elastic anisotropy due to aligned cracks in porous rock. *Geophysical Prospecting* **43**, 805–829.